REPUBLIC OF IRAQ MINISTRY OF HIGHER EDUCATION AND SCIENTIFIC RESEARCH

AL-FURAT AL-AWSAT TECHNICAL UNIVERSITY

ENGINEERING TECHNICAL COLLEGE-NAJAF

ORBITAL ANGULAR MOMENTUM PHENOMENA BASED MICROWAVE ANTENNA ARRAY DESIGN

MUSTAFA ABDULMAHDI MOHAMMED HASAN

.

(B. Sc. In Communications Techniques Eng.)

2021

ORBITAL ANGULAR MOMENTUM PHENOMENA BASED MICROWAVE ANTENNA ARRAY DESIGN

.

THESIS

SUBMITTED TO THE (COMMENICATION TECHNIQUES ENGINEERING DEPARTMENT)

IN PARTIAL FULFILLMENT OF THE REQUIREMENTS FOR THE DEGREE OF (MASTER DEGREE)

BY

MUSTAFA ABDULMAHDI MOHAMMED HASAN

Supervised by

Lecturer Dr. Husam Noman MohammedAli

2021

بسم الله الرحمن الرحيم

سورة الانبياء/ اية33

سورة يس/أية 40

Dedication

To the greatest person that Allah has ever created, **Prophet Mohammad** peace be on him and his family.

To the best person that Allah has ever created after His Prophet, **Imam Ali** peace be upon him.

To those who have all the credit on me, to those who were the cause of my existence, to my beloved **parent**.

To my **wife**, my **brothers** and my **friends**...

To all who supported and encouraged me to achieve my success

Declaration

I hereby declare that the work in this thesis my own except for quotations and summaries which have been duly acknowledged.

August 15, 2021 Mustafa Abdul Mahdi Mohammed Hasan

Supervisor Certification

I certify that this thesis titled " Orbital Angular Momentum Phenomena Based Microwave Antenna Array Design" which is being submitted by Mustafa Abdul Mahdi Mohammed Hasan was prepared under my supervision at the Communication Techniques Engineering Department, Engineering Technical College-Najaf, AL-Furat Al-Awsat Technical University, as a partial fulfillment of the requirements for the degree of Master of Technical in Communication Engineering.

Signature:

Name: **Lecturer Dr. Husam Noman MohammedAli**

(Supervisor)

Date: / / 2021

In view of the available recommendation, I forward this thesis for debate by the examining committee.

Signature:

Name: **Prof. Dr. Ahmad T. Abdulsadda**

(Head of comm. Tech. Eng. Dept.)

Date: / / 2021

Committee Report

We certify that we have read the thesis titled "Orbital Angular Momentum Phenomena Based Microwave Antenna Array Design" submitted by Mustafa Abdul Mahdi Mohammed Hasan and as an Examining Committee, examined the student's thesis in its contents. In our opinion, it is adequate for an award of a degree of Technical Master in Communication Engineering.

Signature:
Name: : **Dr. Husam Noman MohammedAli**
Degree: **Lecturer**
(Supervisor)
Date: / / 2021

Signature:
Name: **Ghufran Mahdi Hatem**
Degree: **Lecturer**
(Member)
Date: / / 2021

Signature:
Name: **Dr. Wafaa Mohammed Ridha Shakir**
Degree: **Assistant Prof.**
(Member)
Date: / / 2021

Signature:
Name: **Dr. Jawad K. Ali**
Degree: **Prof.**
(Chairman)
Date: / / 2021

Approval of the Engineering Technical College- Najaf

Signature:
Name: **Assistant Prof. Dr. Hassanain G. Hameed**
Dean of Engineering Technical College- Najaf
Date: / / 2021

Linguistic Certification

This is to certify that this thesis entitled **"Orbital Angular Momentum Phenomena Based Microwave Antenna Array Design"** was reviewed linguistically. Its language was amended to meet the style of the English language.

Signature:

Name:

Date:

Abstract

The increment in the number of subscribers and devices connected together via the wireless systems or the Internet requires to use of all available resources as much as possible. This thesis targets to shed light on using spatial multiplexing as an extra degree of freedom to increase the communication channel capacity. Typically, time and frequency multiplexing are the most common techniques employed in communication systems.

The orbital angular momentum OAM is a technique exploited in this thesis. The OAM can carry several orthogonal EM signals simultaneously if the system is fed by a circuit being able to feed the OAM system with multiple inputs. The whole research task is divided into three parts to ease the achievement. The first part is devoted to designing the single antenna elements. The adopted antenna structure is the printed crossed-dipole antenna. The design starts with the conventional one and ends with one that has high performance and is a low-profile structure compared with the conventional design. The gain is increased, the cross-polarization components are reduced, the radiation pattern is stable, and the gap between the main radiator and the ground is reduced. The cavity with four walls and the artificial magnetic conductor are utilized to do so. The former way focuses the power on narrower beams, so the gain is enhanced, while the latter way aids to reduce the gap separating between the main radiator and the ground. Also, other things are carried out such as using a bunch of diodes to make the design is a circular polarization reconfigurable antenna.

Second, the RF feeding network is developed using the RF Butler matrix. Each input port can distribute the signal into all the output ports with progressive phase shift, and each port has its own progressive phase shift and is orthogonal to each other. This property enables our proposed design to radiate several orthogonal signals concurrently.

Eventually, several replicas of the printed crossed-dipole antenna are placed in the uniform circular arrangement UCA to come up with the OAM arrays. Four, eight, and nine antenna elements are used in the OAM array as a step

to increase the number of the OAM. The OAM antenna elements are fed directly or with the RF feeding networks. The vortex phase distributions of the far-field EM waves are obtained and shown in the work to support our proposed works.

Acknowledgment

I would like to express my sincere gratitude and acknowledgment for lecturer. Dr. Nasr AlKafaji for his valuable guidance, advice, and timely care extended to me during my research period. I am able to successfully complete this research work and deliver this thesis because of his immense patience and constructive feedback.

I would like to acknowledge the help of Lecturer Dr. Husam Noman MohammedAli for his continuous support throughout this work. His imminent way of thinking has supported me to explore my research abilities and encouraged in implementing the ideas with absolute satisfaction.

Also, I would like to thanks the ministry of electricity Iraq to give me this opportunity to achieve my goals and to give more effort in my career in the company of AlWasat electricity distribution- Najaf branch.

The thanks for to whom give me any assistant or advice that was helpful to this thesis, thanks for your kindness:

Dr. Mustafa Sadiq Aljumaily\ MOC Company –Missan, Iraq.

Dr. Son Xuat Ta\ School of Electronics and Telecommunications-Seoul, South Korea.

Mr. Mohamed Haj Hassan\ University of Duisburg-Essen- Essen, Germany

Mr. Malcolm White\ Creo Medical Ltd- United Kingdom

Contents

List of Tables

List of Figures

List of Abbreviations/ Nomenclature

Abbreviation	Description
3GPP	Third generation partnership project
5G	Five generation
5G NR	Five generation new radio stranded
AMC	Artificial magnetic conductor
BDS	broadcasting services
BM	Butler Matrix
CDA	Cross dipole antenna
CE	common (or current) era
dB	Decibel
DRA	Dielectric resonant antenna
EHF	Extremely High Frequency
EM	Electromagnetic
EM	Electromagnetic
FBW	Fractional Bandwidth
FBW	Fractional Bandwidth
GNSS	global navigation satellite systems
GPS	global position system
HFSS	High Frequency Structure Simulator
HP	Horizontal polarization
IL	Insertion losses
ITU	International telecommunication union
LG	Laguerre polarization

LHCP	Left hand circular polarization
LP	Laguerre polynomial
MIMO	Multi input multi output
OAM	Orbital angular momentum
OERW	open-ended rectangular waveguide
PB	Pancharatnam-Berry
RF	Radio frequency
RF	Radio Frequency
RHCP	Right hand circular polarization
RL	Return losses
SAM	Spain angular momentum
S-parameters	Scattering Parameter
SPP	Spiral phase plat
SPST	single pole single throw switches
SWOT	strengths weaknesses opportunities threats
TE	Transvers electric field
TL	Transmission Line
TM	Transvers magnate field
TZ	Transmission Zero
UCA	Uniform array
UCAAS	Uniform Circular Antenna Arrays
UWB	Ultra Wideband
VQR	vacant quarter ring
WiMax	wireless personal area network and worldwide interoperability
WLAN	wireless local area network

List of symbols

Symbol	Definition		
Z_o	Characteristic Impedance	φ	roll angle
W	Width Transmission Line	ϕ_n	phase of the nth element's
t	Thickness Transmission Line	$e^{jl\phi}$	azimuthal phased term
h	Thickness Substrate	E_{total}	total field

Z_c	Characteristic Impedance	L	orbital angular momentum
c	Speed Of The Light In	S	spin angular momentum
ν_P	Phase Velocity	J	angular momentum
k_o	Propagation Constant	r_n, φ_n	Placement of each individual element
f_c	Cut Frequency	r_m	Stand of radius vector
R_S	Surface Resistance	fr(r)	field variant along the
l	Order Number	ħ	Plank constant topological
L_s	Series Inductance	F	applied force
C_s	Series Capacitance	$\boldsymbol{p}$	object's momentum
L_p	Parallel Inductance	E	Electric field
C_p	Parallel Capacitance	H	Magnetic field
J	Admittance	S	rotational momentum
β	Phase Constant.	P	photon's momentum
a	Loss	LG_{pl}	Laguerre-Gaussian
σ	Conductivity	D	diameter of the circular
η	Impedance of Free Space	h(ϕ)	different phase delays
K_o	Propagation Constant	Δh	greatest thickness variation
γ_o	Impedance Scaling Factor	α_c	Conductive Losses
L	Physical Length	μ_o	Permeability of Vacuum
λ_o	Space Wavelength	ε_o	Permittivity of Vacuum
λ_g	Guided Wavelength	ε_e	Effective Permittivity
α_d	Dielectric Loss	$\tan\delta$	Tangent Losses
ε_r	Permittivity of Dielectric		

List of Publications

Published.

1. M. Hasan, N. Alkhafaji, H. AlAnsary, and A. R. Mohsin, “A small footprint printed cross-dipole antenna with wide impedance bandwidth and circular polarization,” Indones. J. Electr. Eng. Comput. Sci., vol. 24, no. 1, pp. 347–356, 2021, doi: 10.11591/ijeecs.v24.i1.pp347-356.
2. M. Hasan, N. Alkafaji, and H. Al-Anssary, “A wideband Circular polarization cross printed dipole antenna with four quadrants parasitic,” J. Phys. Conf. Ser., vol. 1973, no. 1, 2021, doi: 10.1088/1742-6596/1973/1/012096.

Submitted

1. M. Hasan, N. Alkhafaji and H. AlAnsary “28-GHz OAM Antenna Array with Four Crossed-Dipole Antennas using the 4×4 Butler Matrix ,” Indones. J. Electr. Eng. Comput.

Chapter 1: Introduction and Literature Review

1.1 Introduction

The god says in the holy Quran ‘And He it is who created the night and the day, and the sun and the moon. They float, each in an orbit' (Qur’an 21.33) [1]. Also he says, ‘the sun is not to overtake the moon, nor is the night to outpace the day. Each floats in an orbit.’ (Qur’an 36.40) [1]. The movement of the earth with the sun, the movement of the sun and the earth around themselves, the movement of the solar system are in spiral patterns. Even the angular momentum was mentioned by God in His holy Book 1400 years ago.

In astronomy, Nicolaus Copernicus is the first man to formulate the theory of heliocentric and the Earth’s being a body revolving in its orbit in his book “*On the Revolutions of the Celestial Spheres*”. He is a developer of the theory of the Earth's rotation, and is considered the founder of modern astronomy [2]. Kepler's laws of planetary motion, were published by Johannes Kepler between 1609 and 1619, describing orbits of the planets around the Sun as demonstrated in **Figure 1-1**. The laws have modified the heliocentric theory of Nicolaus Copernicus.

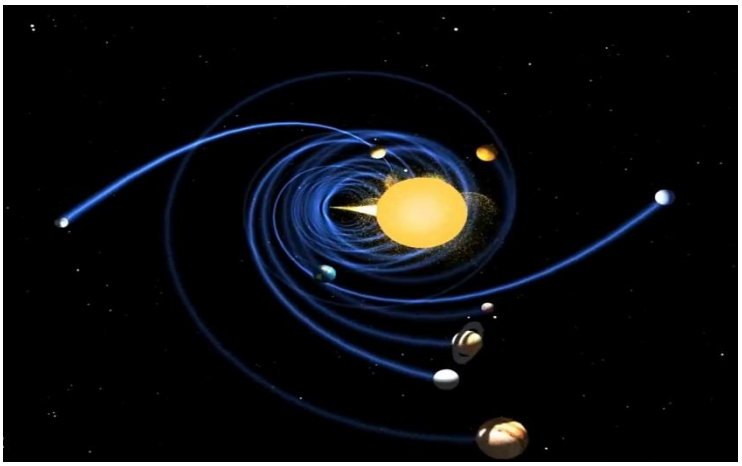

Figure 1-1 The vortex movement of the solar plants.

Explanations mentioned above are examples that would show that our subject is compatible with the theory that says “everything is vortex”. The vortex movement within the axis of rotation (orbital) of the solar system is

similar to the OAM wave form, which is a combination of angular rotation momentum and linear rotation momentum as depicted in **Figure 1-2**.

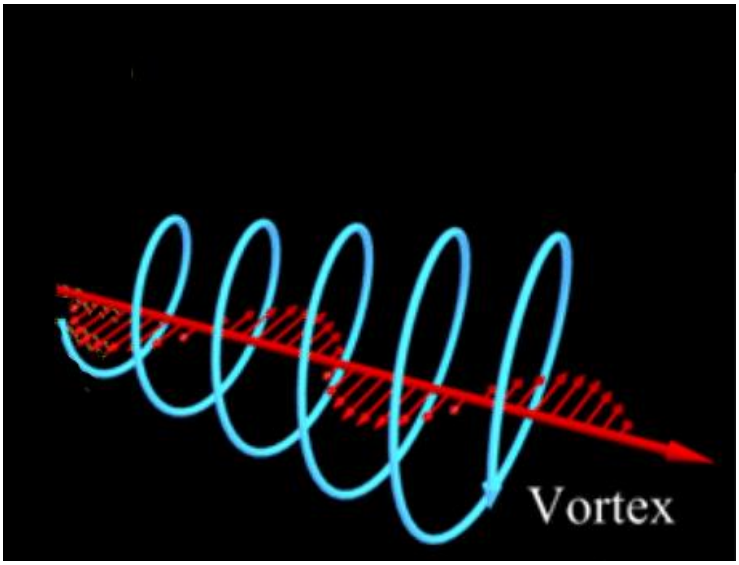

Figure 1-2 OAM electromagnetic vortex wave.

One of the most effective ways to improve channel performance is to use orbital angular momentum (OAM) technology.

According to Maxwell's theory, the momentum can be separated into two parts: linear momentum and angular momentum [3]. The latter one can be categorized as: spin and angular momentums. Typically, the orbital polarization introduced by the EM wave is represented by the spin angular momentum (SAM), while the spatial pattern of the EM wave is represented by the orbital angular momentum (OAM). The OAM, on the other hand, was not heavily investigated till 1992. Allen et al. [3] discovered that there are certain kinds of radiations having an orbital angular momentum of l ħ per photon, where l is an integer known as the "topological charge" or the order of the OAM mode. The phase of a normal plane wave remains constant on the wave front, but the phase α of OAM waves changes linearly along the angular coordinate φ (roll angle): $\alpha = l\varphi$. As a result, the field changes as $e^{-jl\varphi}$ changes $\cdot f_r(r) \cdot e^{-jkz}$, where k is the wave vector, z is the propagation axis, and the field $f_r(r)$ varies along the circular coordinate. This property increases the capacity of communication systems by supporting an infinite number of orthogonal modes, see **Figure 1-3**.

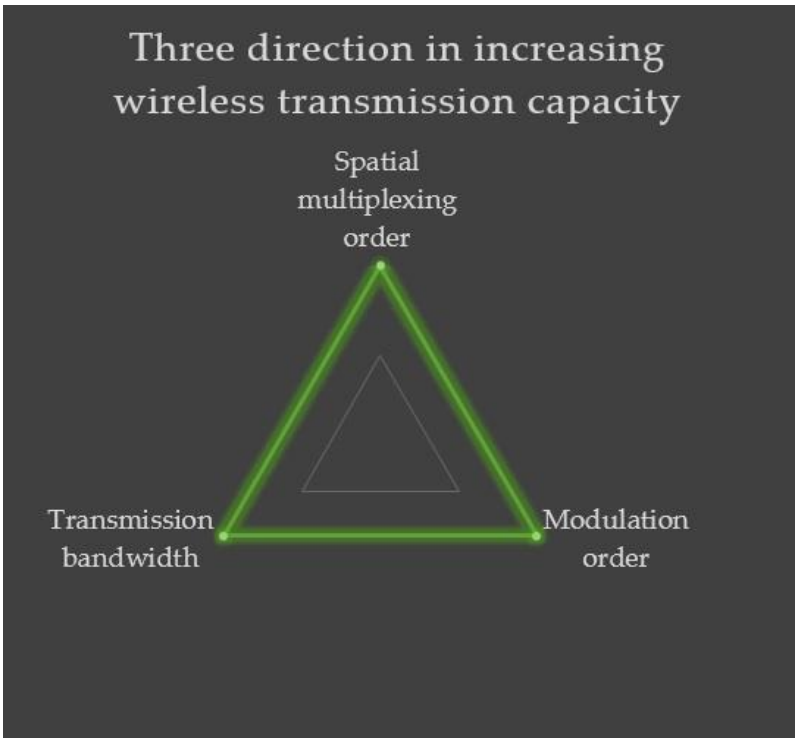

Figure 1-3 The ways of increasing transmission channel capacity.

1.2 Literature Review

In this section, the author aims to chronologically present the most relevant works reported in the literature regarding single antenna or antenna array designs generating the OAM waves. As a number of the modes increases, the antenna array designs should have a large number of elements and will be focused on their results as will be demonstrated **Chapter 4, Table 4-6.** We can see that there are different techniques to generate the OAM waves such as metasurface, holographic gratings, spiral phase plates, dielectric antennas, and others).

Table 1-1 Methods for generating OAM wave.

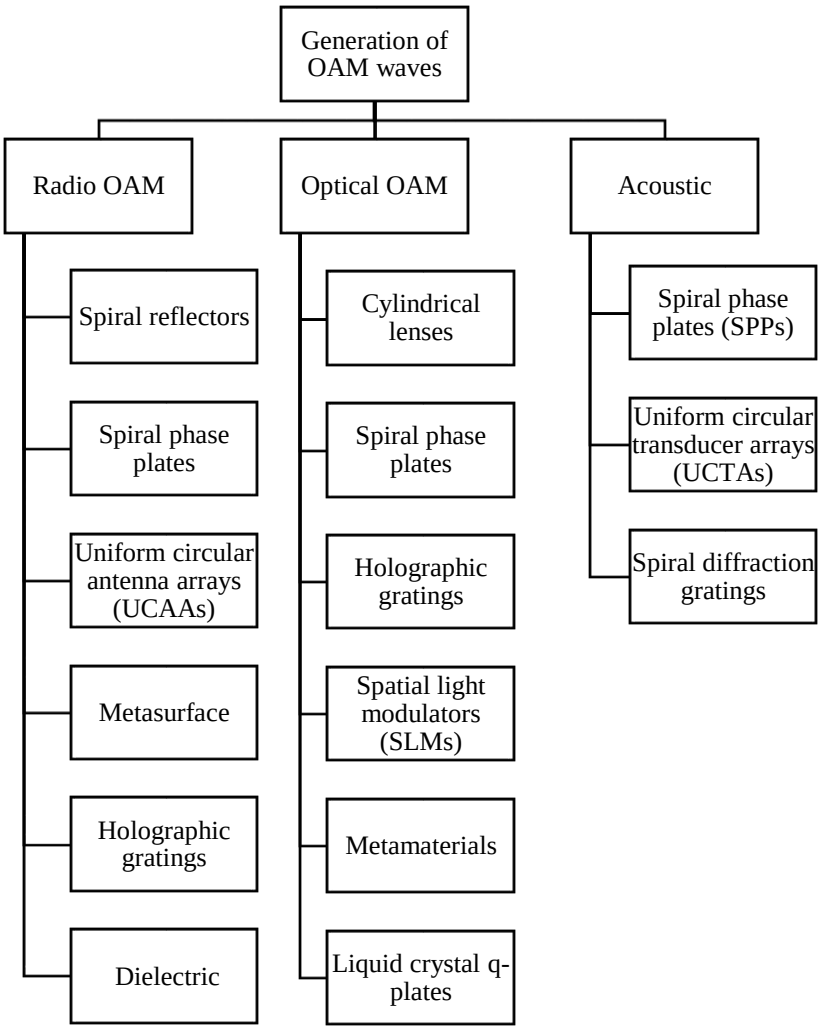

The antenna generating OAM wave can be divided into two main parts:

1.2.1 The Wave Front Manipulation

An EM wave carrying OAM has a helical transverse phase of the form $e^{-jl\varphi}$, generated by manipulating the wave front, with either negative or positive signs that represents a certain mode number of 2π phase changes in the azimuthal direction.

In RF, the spiral phase plate (SPP) is the most basic device for generating OAM beams. In this scenario, the thickness of the SPP is altered azimuthally to provide different phase shifts required to the OAM generation [4].

In [5], the guided waves were combined inside the horn antenna to generate the radio OAM waves. Combining the guided TE11 mode with a single SPP and the TE21 mode with two half-turn SPPs yielded the OAM-EM with mode $l = 1$.

In 2015, authors have implemented a design capable of generating a millimeter-wave OAM beam. Only single beam can be generated, but with low reflectivity SPP [6].

A different way of generating the OAM-EM wave is the 2D thin metasurface. It is a type of artificial structure having periodic or quasi-periodic properties that can achieve some unique properties not found in the nature. Shaped-beams can be created by precisely manipulating the phase and intensity of an electromagnetic wave. The structure of the unit cell, which must achieve at least 2 phase variations and maintain the required amplitude, is the most critical parameter in the RF OAM metasurface antennas.

Kuang Zhang *et al* in 2018 [6], introduced the use of ultra-thin metalenses. By modifying the spatial orientation of the Pancharatnam-Berry phase unit cell, phase shifts of the transmission cross-polarized wave are controlled to obtain the OAM-EM wave.

In 2020, Wang *et al* [7] the interference between wav generated by different layers is optimized by cascading three anisotropic impedance surfaces with custom-designed unit-cells. These cascaded metalenses allow for multiplexed CP vortex-beam transmission, but this multiplexing is valid not only for one signal. Therefore, references [6] and [7] are dedicated to figure out the real spatial multiplexing.

In addition to the SPP and metalenses antennas, the dielectric resonator antenna (DRA) which has several remarkable features such as the small size, the low loss, and the high radiation efficiency attracts a lot of attention recently to generate the OAM-EM wave with several modes. It has been confirmed that the OAM beams can be stimulated by the microstrip patch antenna, where there are two ways for investigating the DRA depending on an order of the electromagnetic modes.

Q-plates construction is a device that behaves differently throughout its surface and especially introduces distinct phase shifts depending exclusively on the azimuthal angle in order to convert the constant phase of the wave front into one with azimuthally dependence φ.

The authors MacCalli *et al* in 2013 [8], had used a well-known and low-cost manufacturing technology which is the PCB, creating the Q-plates operating at the millimeter wavelengths. By cutting grooves with precise geometry from the conventional dielectric materials where this material becomes inhomogeneous, the OAM-EM wave is readily generated.

1.2.2 The Spatial Multiplexing Applicability.

Single dielectric resonator antennas can be exploited to generate the OAM - EM waves with multiple modes (i.e., the spatial multiplexing), where it was proposed by J. Ren and K. W. Leung [9]. Two orbital angular momentum (OAM) states with l = +1 and -1 were demonstrated by applying two orthogonal feeding ports using the 90-degree hybrid coupler. Although, a number of the generated modes in this design is limited, the simple feeding circuit motivates us to use a combination of this feeding circuit to come up with a circuit being able to support a higher number of the OAM-EM modes.

The other methodology which is more relevant to our work is the uniform circular array (UCA). This type of arrays is now the most common method of generating the RF OAM beams. N elements are equidistantly arranged on a circle with a radius of around the beam axis in the standard UCA. Each element is fed with a uniform amplitude signal to generate the OAM mode of l, and the phase of the nth element should obey the following formula [10]:

$$\phi_n = \frac{2\pi nl}{N} \qquad \textbf{1-1}$$

This method is different from all others mentioned above to generate the OAM-EM waves, because the generated modes relies on a number of the antenna elements utilized in the proposed OAM array. Generally, the

channel capacity increases as a number of the modes increases. Thus, adopting array with higher modes is the goal in this research study, but the computation resources are limited, leading to a lack of maneuverability in the designs.

Bai *et al* in 2014 [11], had reported the circular array consisting of eight identical rectangular patches, excited by an asymmetrical a back-fed via-50Ω microstrip patch with feeding network. The increase in the phase after full rotation is 360° for the OAM modes +1 or -1, in which the circular array arrangement is the most suitable one. One drawback accompanying the UAC array is the single feeding port, and the spatial multiplexing will not be easier to obtain. Consequently, designing a feeding network supplying several input orthogonal signals concurrently is imperative.

But it still one input feed even the good idea for the sequential feeding network we can judge on this design is similar to the fore mention antennas design that used the front wave to be vortex wave.

In 2016, Bai *et al* [12], had reported a design generating two circularly polarized (CP) dual-modes $l = \pm 1$ with the OAM beams, thereby presenting multiplexing property. The OAM antenna array is made up of four dual-CP elements that are rotated 90 degrees clockwise. The four elements are fed with the same progressive phase shift for both left-hand circular polarization (LHCP) and right-hand circular polarization (RHCP), but with the opposite directions. this phase sequentially is our target in to the next literatures researches.

In 2017, Li *et al* [13], had also used four-element antenna OAM array with a U-shaped and an M-shaped microstrip feeding lines to excite the quasi-cross-shaped aperture. The antenna array was able to produce dual-mode OAM waves $l = \pm 1$. The OAM array seemed to have good performance, but on the other hand, the feeding type is not compatible with the single elements adopted in this thesis.

It is clearly to declare that most researchers have used the patch antennas in their OAM design. However, the patch antennas have low gains, so adding parasitic elements such as directors enhances the gain obviously.

In 2017, Liu *et al* [14] had reported a programmable OAM structure. The PIN diodes on the feeding network were inserted to control the preferred mode. This feature is useful to encrypt the digital data by varying changing the OAM +1 and -1 modes into the LHCP and RHCP, respectively. This design motivates us to adopt the smart feeding to make the antenna array dynamic array but not restricted to only two mode as in this paper [15].

In 2020, Kang *et al* [15], a four-element circular patch array with ± 1 OAM modes capabilities was proposed employing a reconfigurable feeding network. Furthermore, a bunch of PIN diodes were the control elements in the proposed design. Only two modes were realized by the aid of a microcontroller.

Byun *et al* [16], three orbital angular momentum (OAM) modes ($l = 0$, $l = \pm 1$) had been reported. These three modes could be excited simultaneously. In other words, we can say that the spatial multiplexing was obtained owing to the use of a combination of the quadrature couplers, crossovers, and phase shifters. It is simply the Butler matrix.

In the subsequent references, the OAM arrays with higher modes were found in the literature using the Rotman lens feeding network technique to feed UCAA.

In 2016, Bai *et al* [17], a Rotman lens-fed antenna array was used to generate five-mode OAM radio beams. A suitable method for the generation of the multi-mode OAM radio beam was carried out by integrating several layers Rotman lens based the OAM feeding network. To obtain the helical wave fronts from an N-element OAM circular array, each array element should be fed with the same amplitude but with a different phase difference for each consecutive element. The circular array is made up of nine uniform rectangular patches that are joined with the Rotman lens.

In 2020, Zhang *et al* [18], proposed an OAM antenna array which was similar to the previous research of a microstrip Rotman lens but with 9-element uniform circular array antenna to increase the OAM modes.

Additionally, high-gain patch elements, to boost the OAM beam gain, were utilized.

In this thesis, a design of the OAM array, consisted of two layers, will be presented. The antenna array is mounted on the top layer, while the Butler based the smart feeding network is placed on the bottom layer. The array elements will arrange in a circular fashion as a step to accommodate the phase shift distribution. The coaxial probe-fed is the element connecting between elements and the feeding ports. Also, the single antenna elements adopted in this research work are used for the first time.

1.3 SWOT Analysis

The SWQT analysis is a strategic planning technique used to identify strengths, weaknesses, opportunities, and threats related to technique competition or project planning. From our strategic planning process and to focusing on the keys issues, we will try to define the key issues by the survey for whole the OAM antenna types. This will be helpful to formulate the strengths and weaknesses which are internal while opportunities and threats are the external factors. To choose the best way to generate the OAM antenna with most useful Orbital Angular Momentom properties which they should be compatible to our problem statements and motivation, **Table 1-2** defines all the RF OAM antennas according to their strengths and weaknesses [19].

Strength, weakness, opportunity, and threat (SWOT) analysis of our

Table 1-2 Types of generating OAM's antennas

Features	**SPPs**	**Holographic gratings**	**Spiral reflectors**
Cost	Low	Low	Low
Speed	Normal	Fast	Normal
Conversion efficiency	High	Low	Normal
OAM mode	Single mode; Non-pure mode	Multiple mode	Single mode; Non-pure mode
Flexibility	Low	Low	Low
Working frequency	One point	All	One point
Processing difficulty	High	High	High
System complexity	Low	Low	Low
Market readiness	No	No	No

Features	**UCAAs**	**Metamaterials**	**Dielectric q-plates**
Cost	High	Low	Low
Speed	Normal	Fast	Normal
Conversion efficiency	Normal	Relatively high	/ (Not discussed)
OAM mode	Multiple modes; Composite mode	Single mode	Single mode; Pure mode
Flexibility	High	Low	Low
Working frequency	All	One point	One point
Processing difficulty	Low	High	High
System complexity	High	Low	Low
Market readiness	Yes	No	No

proposed OAM UCA are demonstrated in **Figure 1-4**. The UCA is the best candidate one because it can easily achieve our thesis objectives.

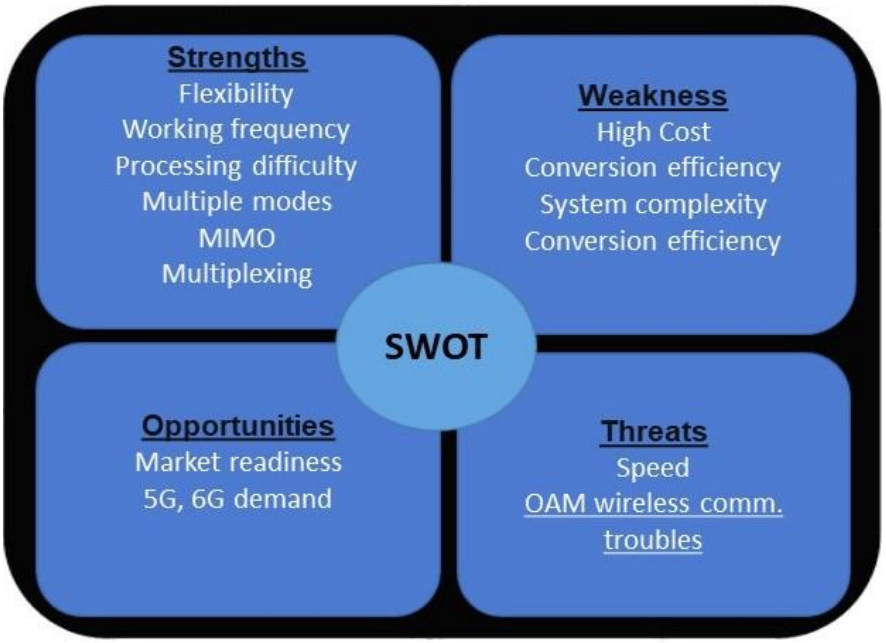

Figure 1-4 The internal and external SOWT analysis of UCA antenna.

1.4 Motivation

One of the most important points that has motivated the researcher is the need for more capacity (demanded). **Figure 1-3** shows the modulation and transmission factors being limited, so adding the spatial multiplexing that will rise the capacity is the best solution. The OAM is a new technology and it will fulfill the our research goals by increasing the channel spectrum (i.e., increasing the data rate. This opens the door for a new debate how to exploit the OAM technology.

1.5 Problem Statements:

- In the 5G systems, devices work at higher frequencies, so the propagating waves in space attenuate quickly after a short distance from the antenna source. Consequently, using an antenna array rather than single antennas becomes imperative. Besides, the conventional arrays cannot carry signals with more than one polarization at the same time. These two restrictions will be addressed in this research study.

- Most previously reported works have responses that cannot be altered after fabrication with large footprints.

1.6 Thesis Objectives:

- Design single new antenna with capability of generating different states of wave polarizations to fulfill the design requirements given above in the problem statements. Also, these antennas will be investigated in the millimeter wave bands (e.g., 5G).
- Figure out topological ways of antennas arrangements to produce the effective OAM arrays. In other words, they can generate different states of OAM polarizations using less complicated structures.
- Make the design controlled autonomously using the smart feeding network.

1.7 Organization of Thesis

- **Chapter 2** introduces the most basic theory required to have a solid background about the work in the succeeding chapters.
- **Chapter 3** is devoted to study and analyze the conventional printed crossed-dipole antenna with several new modifications to be compatible with the requirements in the later chapter.
- **Chapter 4** investigates several new designs of the OAM antenna arrays using the smart feeding network.
- **Chapter 5** concludes the thesis and presents some potential future works.

Chapter 2: Theoretical Background

2.1 Introduction

The fundamental properties of momentum electromagnetic fields, the spin angular momentum SAM, and the orbital angular momentum OAM will be discussed first in this chapter. Also, the chapter will explain the Laguerre - Gaussian LG beam equation of OAM. Next, all the necessary theoretical background to design single antenna, array, and the RF smart feeding network will be introduced to give readers the cohesive information about the proposed works in Chapters 3 and 4.

2.2 Theoretical and Momentum Conception of OAM EM wave

2.2.1 Poynting Vector, Linear Momentum:

The Poynting vector is a vector whose magnitude is equal to the wave power density and whose direction shows the propagation direction of an EM wave in the absence of rotational momentum. It's measured in W/m^2 and has the following definition:

$$S = E \times H \qquad \textbf{2-1}$$

The electric and magnetic fields are represented by E and H, respectively. A photon's momentum, p, is thus given as:

$$p = \hbar k \qquad \textbf{2-2}$$

The wave number k is represented by the ħ decreased Plank constant.

2.2.2 SAM and OAM (Angular Momentum)

Poynting proposed in 1909 that a circularly polarized EM wave can carry rotational momentum [20]. His deduction was based on a comparison between a mechanical model – a uniformly spinning shaft with a circular section – and a circularly polarized light beam. He arrived at the following conclusion: The angular momentum provided to unit area per second is:

$$\frac{p\lambda}{2\pi} \qquad \textbf{2-3}$$

A pressure of radiation wavelength λ applied on a surface is denoted by p. This is equivalent to saying that the angular momentum is equal to l, with $l = \pm 1$ corresponding to the left and right circular polarization,

respectively. Because it is connected with the spin of the photon **Figure 2-1 (a)**. This component of the angular momentum is known as the spin angular momentum (SAM). This can be seen by rotating the photon around its own axis. As a result, there might be two different values of l, each of which corresponds to a different rotation direction [21]. Because the photon does not require an external reference, the SAM is also known as intrinsic angular momentum.

A second sort of angular momentum, which is defined in connection to an external reference, is called extrinsic angular momentum. A photon's orbit around a spot can be used to symbolize it. This is why it's called "orbital

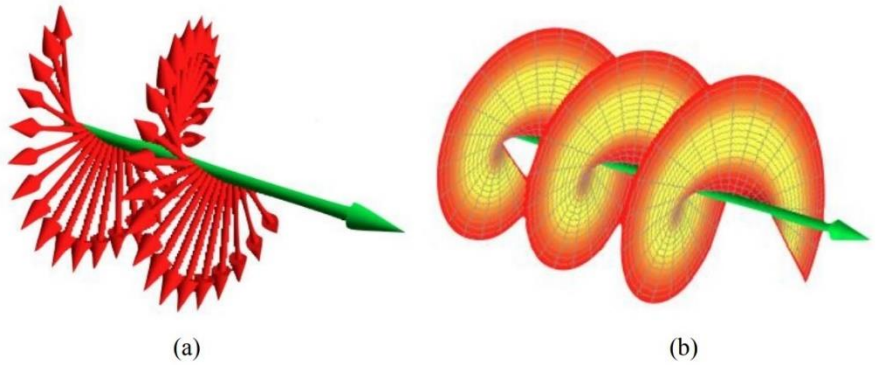

Figure 2-1 (a) The SAM of an EM wave; (b) the OAM of an EM wave [7].

angular momentum (OAM)" in **Figure 2-1**. This connects the equivalence between the sign ("+" or "-") and the rotational direction, but this time the value is related to the rotational speed (i.e. the number of jumps of 2π for each period). As a result, it can theoretically persist indefinitely. In 1992, a group from the University of Leiden [3] revisited the topic, focusing on the transformation of orbital angular momentum using the Gaussian beam. They were particularly interested in the Laguerre-Gaussian (LG) modes, which are defined by the same-named polynomials and have a variable term of exp(-ilφ) in their formulation. Here, l denotes the "topological charge," or the order of the OAM mode, and φ denotes the phase of the roll angle. In this situation, l is directly implicated in the expression of the OAM carried by the beam: to match the $l\hbar$ of the SAM and the k of the momentum. The latter would be of $l\hbar$ per photon. **Figure 2-2** depicts the Poynting vectors

associated with a linearly polarized LG beam (in the near field and without accounting for beam divergence), with l denoting the number of spirals. The vectors are not in the beam axis, but rather turnabout. The Poynting vector of a linearly polarized Laguerre-Gaussian mode of radius m(z) [3] is represented by the spiraling curve.

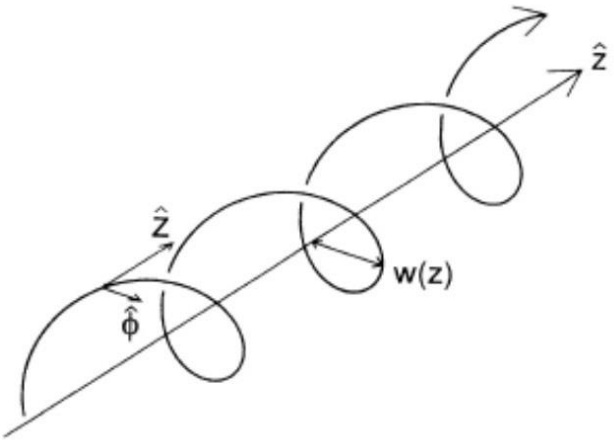

Figure 2-2 The Poynting vector of a linearly polarized Laguerre-Gaussian mode of radius w(z) is represented by the spiraling curve [3].

This phenomenon can be observed empirically by measuring the intensity and phase distributions [21]. An EM wave containing OAM can be decomposed into a sum of LG beams, denoted by LG_{pl} [22], just like any other EM wave within the limits of paraxial approximation

$$LG_{pl} = \sqrt{\frac{2p!}{\pi(p+|l|)!}}\frac{1}{w(z)}\left[\frac{r\sqrt{2}}{w(z)}\right]^{|l|}\exp\left[\frac{-r^2}{w^2(z)}\right]L_p^{|l|}\left[\frac{2r^2}{w^2(z)}\right]\exp(il\varphi) \quad \textbf{2-4}$$
$$exp\left[\frac{ik_0r^2z}{2(z^2+z_R^2)}\right]\exp\left[-i(2p+|l|+1)\tan^{-1}\left(\frac{z}{z_R}\right)\right]$$

where the l/e radius of the Gaussian term is given by $w(z) = w(0)[(z^2 + z_R^2)/z_R^2]^{1/2}$ with w(0) being the beam waist, z_R is the Rayleigh range, and $(2p + |l| + 1)\tan^{-1}(z/z_R)$ is the Gouy phase. $L_p^{|l|}(x)$ is an associated Laguerre polynomial, obtained from the more familiar Laguerre polynomials by:

$$L_p^{|l|}(x) = (-1)^{|l|}\frac{d^{|l|}}{dx|l|}L_{(p+|l|)}(x) \quad \textbf{2-6}$$

The OAM mode's order is l, and the number of radial nodes in the intensity distribution is p. We find a Gaussian distribution with the order l = 0. The intensity is dispersed in the form of a ring (donut) centered on the beam axis for any other value of l. **Figure 2-3** shows the intensity and phase graphs of LG modes of LG_{01}, LG_{11} and LG_{21}, as an example. An LG mode consists of p + 1 concentric rings with a zero on-axis intensity in terms of intensity on a plane perpendicular to the propagation axis. In addition, the phase distribution for each ring changes from 0 to 2π along the roll angle.

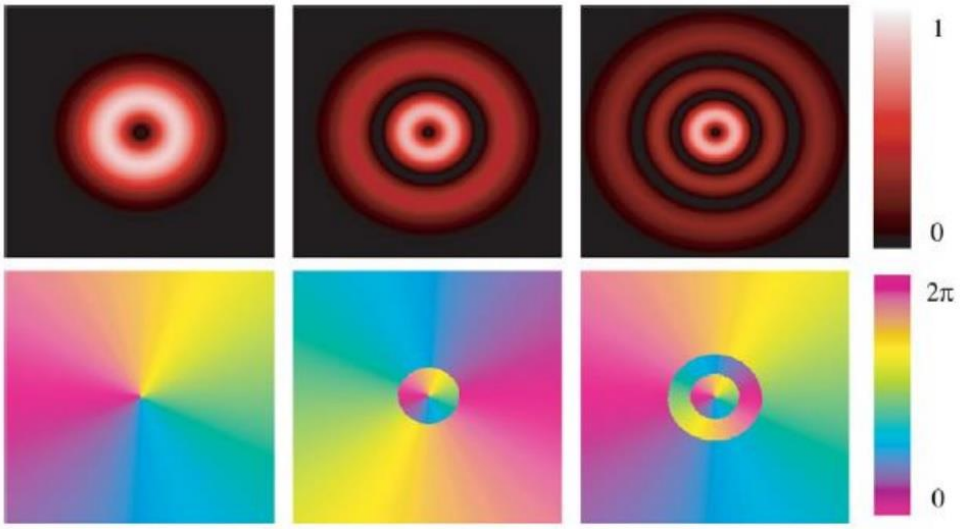

Figure 2-3 LG01, LG11, and LG21 (left to right) normalized intensity (top) and phase (bottom) plots showing the p + 1 concentric rings and their effect on the phase pattern [23].

2.2.3 Optical Frequency Methods for Generating OAM Waves

As shown in **Figure 2-4**, the EM waves carrying OAM have a helical phase front as exp(-ilφ) (l: the order of the OAM mode, φ: the roll angle). As a result, producing the helical phase front is crucial for creating OAM waves.

Many methods for creating OAM waves have been demonstrated since Allen's experiment in 1992. These approaches can differ from one another at different frequency bands. Because OAM is a physical phenomenon that occurs across the electromagnetic spectrum, each frequency band can benefit from the benefits of others.

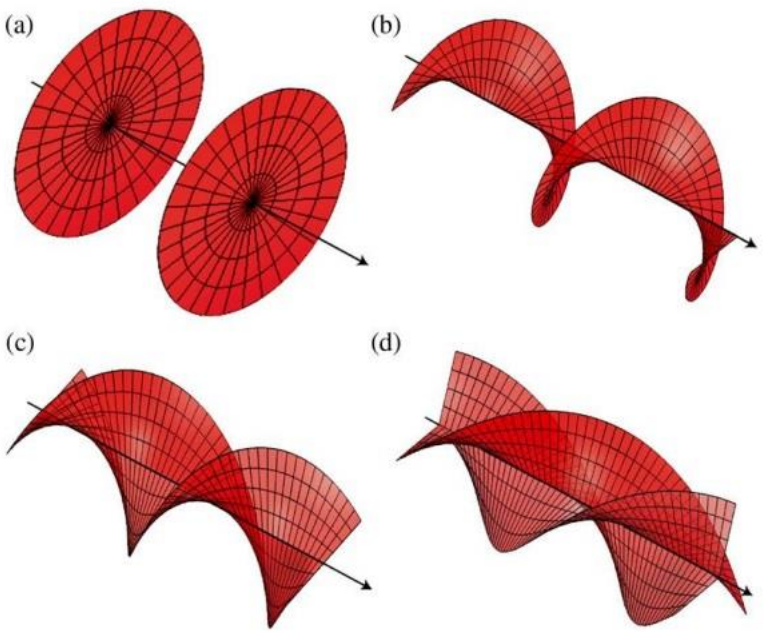

Figure 2-4 Plane phase front for (a) l = 0 and helical phase fronts for (b) l = 1; (c) l = 2; (d) l = 3 [23].

2.3 The Theoretical and Conceptions of Antenna and antenna array

The IEEE standard descriptions of terms for antennas defines an antenna as a device for transmitting or receiving radio waves [24]. A structure connected with the zone of transition between a guided wave and a free-space wave, or vice versa, is known as an antenna. The shift from guided waves to free space is a critical aspect in determining the radio link's quality. Two separate areas can be defined in the event of a vacuum surrounding the antenna (the radio links), as shown **Figure 2-5**:

- The near-field region $r_{ner} = \mathrm{D}^2/\lambda$ encompasses the immediate vicinity of the antenna and extends all the way to the far-field zone.
- Starting at a distance of $r_{far} = 2\mathrm{D}^2/\lambda$, where D is the all-out antenna measurement, the far-field area is the farthest distance from the antenna. At a distance from the antenna's phase center, the field distribution is independent in this region.

The far-field is the spatial Fourier transform of the near-field, which necessitates the complete E and H-fields in the near-field region. They are described using vectors.

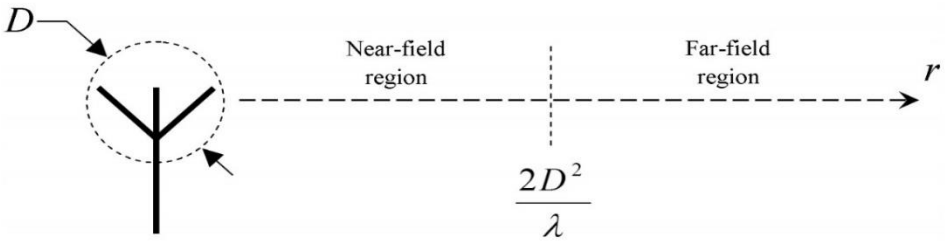

Figure 2-5 The near-field and far-field areas of an antenna are depicted in this diagram.

2.3.1 Polarization

To explain polarization, we employ the *axial ratio*, *AR*, and *tilt angle*, τ. The AR ratio is the length of the minor axis divided by the length of the major axis, and it ranges from 0 (linearly polarized) to 1 (radially polarized) (circularly polarized). The smallest angle between the axis and the major axis is the tilt angle. This indicates that it is somewhere between 0 and π/2. Circularly polarized radiation is either left-hand or right-hand in general. The polarization is right-handed if E moves in a clockwise direction while the wave propagates, and left-handed if E moves in a counterclockwise direction. Consider the situation [26].

The equation for AR simplifies is given as:

$$AR = \frac{E_{\varphi 0}}{E_{\theta 0}} \text{ or } AR = \frac{E_{\theta 0}}{E_{\varphi 0}} \quad \textbf{2-5}$$

In this case, the condition 0 or 1 determines which equation is accurate.

2.3.2 Array Factor of UCAA

The array's normalized field can be written as [26].

$$E_k(r,\theta,\varphi) = \sum_{k=1}^{NM} a_k \frac{e^{-ikR_k}}{R_k} \quad \textbf{2-6}$$

The distance between the K_{th} element and the observation point is R_k. This distance can be represented using the notations shown in **Figure 2-6**.

$$R_k = R_{mn} = (r^2 + a_{mn}^2 + 2a_{mn}\cos\psi_{mn}) \quad \textbf{2-7}$$

For $r \ll a$ this expression reduces to

$$R_{mn} \simeq r - a\cos\psi_{mn} = r - a\sin\theta\cos(\varphi - \varphi_{mn}) \quad \textbf{2-8}$$

If we suppose that for the amplitude $R_k \approx r$, we get the electric field expression as follows

$$E_{mn} = \frac{e^{-ikr}}{r} \sum_{m=1}^{M} \sum_{n=1}^{N} a_{mn} e^{ika_{mn} \sin\theta \cos(\varphi - \varphi_{mn})} \quad \textbf{2-9}$$

where a_{mn} is the excitation coefficient, which can be written as $I_{mn}\, e^{i\beta}$ resulting in

$$E_{mn} = \frac{e^{-ikr}}{r} \sum_{m=1}^{M} \sum_{n=1}^{N} I_{mn} e^{i(ka_{mn} \sin\theta \cos(\varphi - \varphi_{pn}) + \beta_{mn})} \quad \textbf{2-10}$$

In our situation, the phase β will be determined solely by which n we consider, not by the radius, because the phase should be equal in "beams" from the center. The variable φ will only be affected by n and not by m. Both m and n will influence the amplitude I. Finally, a will be solely relied on m.

$$E_{mn} = \frac{e^{-ikr}}{r} \sum_{m=1}^{M} \sum_{n=1}^{N} I_{mn} e^{i(ka_{m} \sin\theta \cos(\varphi - \varphi_{n}) + \beta_{n})} \quad \textbf{2-11}$$

The array factor, AF, is then obtained as:

$$[\mathrm{AF}] = \sum_{m=1}^{M} \sum_{n=1}^{N} I_{mn} e^{i(ka_{m} \sin\theta \cos(\varphi - \varphi_{n}) + \beta_{n})} \quad \textbf{2-12}$$

2.3.3 The Element Position in the UCAA

Each element has an A_g surface area. r_m and φ_n describe the position of each individual element, where m defines the ring the element is put in and n denotes the element's position within that ring. N is the total number of elements in each ring, and M is the total number of rings.

$$\frac{a_1^2 \alpha}{2} = A_g \quad \textbf{2-13}$$

$$\frac{a_2^2 \alpha}{2} - \underbrace{\frac{a_1^2 \alpha}{2}}_{A_g} = A_g \quad \textbf{2-14}$$

$$\frac{a_m^2 \alpha}{2} - (m-1)A_g = A_g \quad \textbf{2-15}$$

where α is the angle in which the area segments are divided. This provides us the formula for calculating the radii of each subsection.

$$a_m = \sqrt{\frac{m}{M}}a \qquad \textbf{2-16}$$

Let r_m stands for the radius vector of each subsection's center, which is where the antenna is positioned.

$$\frac{r_m^2\alpha}{2} - \frac{a_{m-1}^2\alpha}{2} = \frac{a_m^2\alpha}{2} - \frac{r_m^2\alpha}{2} \qquad \textbf{2-17}$$

As a result, we get the following expression.

$$r_m = \sqrt{\frac{(2m-1)}{2M}}a \qquad \textbf{2-18}$$

The element's φ_n is determined by

$$\varphi_n = \frac{2\pi n}{N} \qquad \textbf{2-19}$$

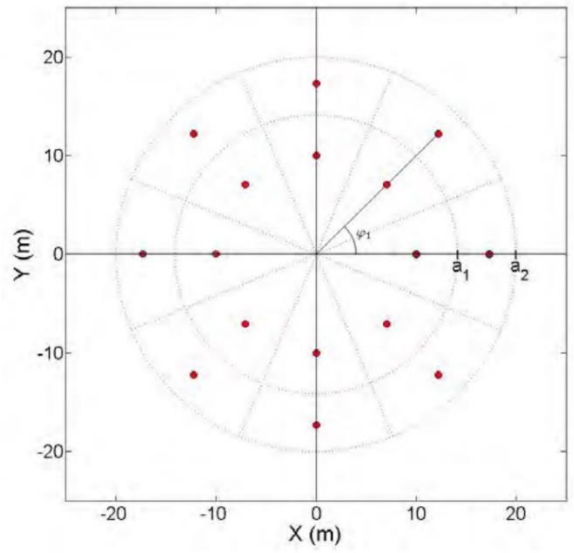

Figure 2-6 Circular grid with equal area segments.

2.3.4 Feeding Mechanism

The feeding of microstrip antennas can be done in a variety of ways. The microstrip line, coaxial probe, aperture coupling, and proximity coupling are the most four used methods. Coaxial feeding lines are common, with the inner conductor of the coax linked to the radiation patch and the outside conductor to the ground plane. The coaxial probe feed is quite simple to obtain the matching although it emits very little spurious radiation.

A- Coaxial Cable Impedance Calculator

The impedance of most RF Coaxial Cables is 50 ohms. They are easily available. Users may require a specific impedance value in particular instances. This can be accomplished by controlling the coaxial cable's inner and outer diameters, as well as the dielectric [25].

Because of the distance between the inner conductor with (d) diameter and the outside shield with (D) diameter of the cable, the coax cable has capacitance (C). The capacitance value changes depending on the conductor spacing, dielectric constant, and cable impedance. The following formula can be used to compute the capacitance.

$$C = \frac{7.354 \times \varepsilon_r}{\log_{10}\left(\frac{D}{d}\right)} \quad \textbf{2-20}$$

The dielectric constant of the material between the conductors has no effect on the inductance (L) of the coaxial cable, which is proportional to the length of the line. The following formula can be used to find the inductance.

$$L(\text{ Inductace })nH = 140.4 \times \log_{10}\left(\frac{D}{d}\right) \quad \textbf{2-21}$$

The diameter of the inner and outer conductors, as well as the cable's dielectric constant, determine the RF coaxial cable's impedance (Z_o). The impedance can be determined using the formula below.

$$Z_o(Ohms) = \frac{138 \times \log_{10}\left(\frac{D}{d}\right)}{\sqrt{\varepsilon_r}} \quad \textbf{2-22}$$

The relative permittivity of the medium, as well as the outer and inner diameters of the conductors, determine the cutoff frequency of the coaxial cable. The formula for calculating the cutoff frequency is as follows.

$$\text{Cutoff Frequency (GHz)} = \frac{11.8}{\sqrt{\varepsilon_r} \times \pi \times \left(\frac{D+d}{2}\right)} \quad \textbf{2-23}$$

B- Microstrip Line Impedance

Microstrip transmission lines are printed circuits that consist of a copper or other conductor strip on an dielectric substrate. The ground is metal and placed on the other side of the substrate. There is also a conductor printed

on the top side of the substrate. As a result, a microstrip is a two-wire transmission line with a different configuration as depicted in **Figure 2-7**.

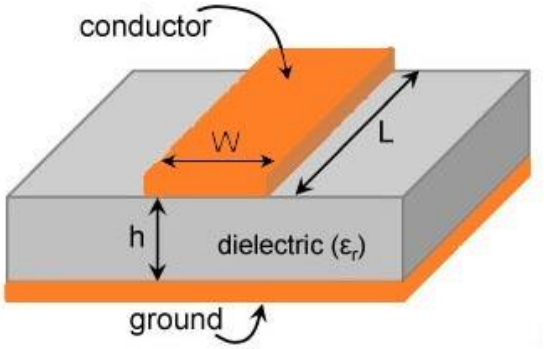

Figure 2-7 A microstrip transmission line.

Usually, the term "effective permittivity" or "ε_{eff}," is used for the microstrip transmission lines. It is obvious that ε_{eff} will be affected by W and h as will be below demonstrated. As a result, these characteristics will affect phase velocity along the microstrip. The phase velocity will be obtained by assuming that the relative permeability of all materials in the line design is well approximated by $\mu_r = 1$.

$$u_p = \frac{c}{\sqrt{\varepsilon_{eff}}} \qquad \textbf{2-24}$$

Because these features influence the line's characteristic impedance (Zo), we will have to deal with a change in phase velocity (or time delay) and, as a result, the wavelength of waves on the microstrip lines are smaller compared to free-space wavelength.

The effective dielectric constant is confined between

$$\text{maximum } \varepsilon_{eff} = \varepsilon_r \qquad \textbf{2-25}$$

And

$$\text{minimum } \varepsilon_{eff} = \frac{1}{2}(\varepsilon_r + 1) \qquad \textbf{2-26}$$

This results in a range:

$$\frac{1}{2}(\varepsilon_r + 1) \leq \varepsilon_{eff} \leq \varepsilon_r \qquad \textbf{2-27}$$

If $(\frac{W}{H}) < 1$:

$$\varepsilon_{eff} = \frac{\varepsilon_R + 1}{2} + \frac{\varepsilon_R - 1}{2}\left[\frac{1}{\sqrt{1 + 12\left(\frac{H}{W}\right)}} + 0.04\left(1 - \left(\frac{W}{H}\right)\right)^2\right] \quad \textbf{2-28}$$

and

$$Z_0 = \frac{60}{\sqrt{\varepsilon_{eff}}} ln\left(8\left(\frac{H}{W}\right) + 0.25\left(\frac{W}{H}\right)\right) \quad \textbf{2-29}$$

If $(\frac{W}{H}) > 1$:

$$\varepsilon_{eff} = \frac{\varepsilon_R + 1}{2} + \left[\frac{\varepsilon_R - 1}{2\sqrt{1 + 12\left(\frac{H}{W}\right)}}\right] \quad \textbf{2-30}$$

and

$$Z_0 = \frac{120\pi}{\sqrt{\varepsilon_{eff}}\left[\frac{W}{H} + 1.393 + \frac{2}{3} ln\left(\frac{W}{H} + 1.444\right)\right]} \quad \textbf{2-31}$$

The W/H ratio can be calculated using the required characteristic impedance.

2.3.5 Dipole Antenna

The simplest basic form of radio antenna is the dipole antenna, which consists of two conducting metal rods, separated by a small gap, with total length equal to a half of the maximum wavelength. Their far ends are left unconnected, while their near ends are connected the feeding network that supplies the RF signals to the two arms with equal amplitude but they have opposite phase. They are employed in many famous applications, particularly in rabbit-ear television antennas, and as driving components in other antennas. **Figure 2-8(a)** illustrates the electric field E lines generated between the arms of a tiny center-fed dipole in the first quarter of the period when the charge has reached its maximum value (assuming a sinusoidal time variation), and the lines have covered a radial distance of $\lambda/4$. Let us pretend that there are three lines generated in this example. The original three lines travel an additional $\lambda/4$ (a total of $\lambda/2$ from the initial location) over the next quarter of the period, and the charge density on the conductors

begins to decline. This is accomplished by adding opposite charges, which have neutralized the charges on the conductors by the conclusion of the first half of the period. **Figure 2-8(b)** depicts the three lines of E formed by the opposite charges, which are separated by a distance of $\lambda/4$ during the second quarter of the first half.

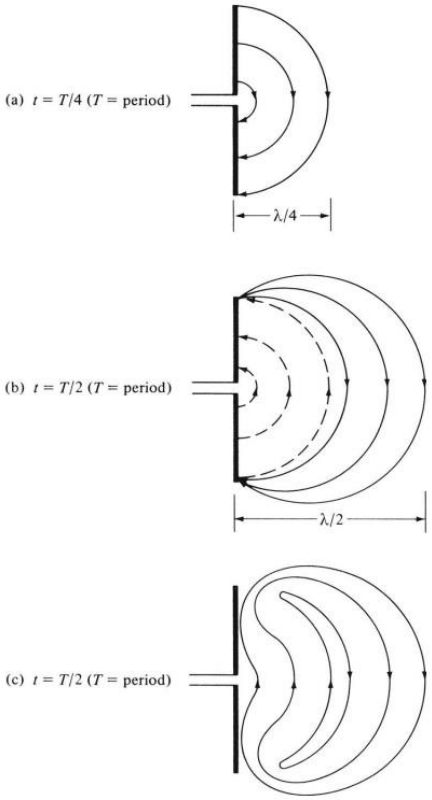

Figure 2-8 Electric field line formation and detachment for a short dipole a) [26].

The ultimate consequence is that the first $\lambda/4$ distance has three lines of E pointing upward and the second $\lambda/4$ distance has the same amount of lines pointing downward. Because the antenna has no net charge, the lines of force must have been forced to separate from the conductors and join together to create closed loops, see **Figure 2-8 (c)**. The identical procedure is repeated in the second half of the period, but in the opposite direction. The procedure is then repeated endlessly where the electric field E patterns emerge [26].

2.4 The Components of Single and Array Antenna Structure

In this section, all parts utilized in the antenna structures are described. Artificial magnetic conductors AMCs, electronic control switches such as

PIN diodes, smart feeding networks will be covered. All these parts will be integrated together as a step to enhance the overall performance of the proposed designs.

2.4.1 Artificial Magnetic Conductors

The AMC is made up of a series of uniformly sized metallic unit cells that are stacked in a regular pattern. **Figure 2-9** shows the electromagnetic structure, the circuit model and the corresponding inductance-capacitance for the AMC/HIS structure. The HIS surface impedance, Z_{HIS}, is provided by Equation (2-32), where L and C are inductance and capacitance, respectively, because of vias joining unit cells to the ground and the gap between two nearby metallic unit cells, and ω is frequency [27].

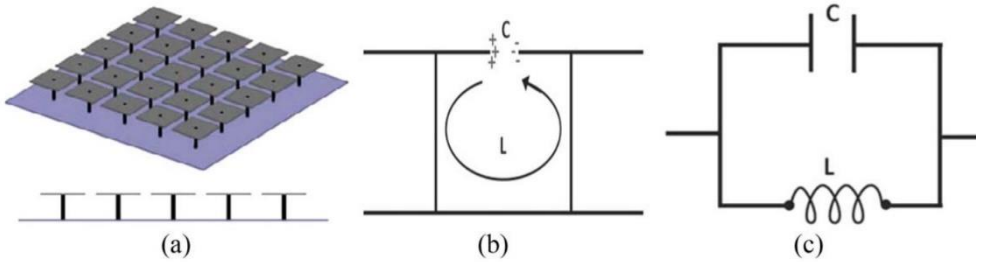

Figure 2-9 (a) AMC unit cells (b) the equivalent inductance capacitance circuit (c) the circuit model.

At the HIS resonance frequency, the $\omega_0 = 1/\sqrt{LC}$. A denominator of Equation (2-32) reaches zero at a specific frequency, resulting in an ideal surface with infinite impedance.

$$Z_{\text{HIS}} = \frac{j\omega L}{1 - \omega^2 LC} \qquad \textbf{2-32}$$

$$\theta = \text{Im}\left[\ln\left(\frac{Z_{\text{HIS}} - \eta}{Z_{\text{HIS}} + \eta}\right)\right] \qquad \textbf{2-33}$$

Equation (2-33) explains the reflection phase generated by the HIS when an incident wave is oriented normal to the surface. As the surface's impedance approaches infinity, the reflection phase of the surface approaches zero. In this case, the surface has the properties of the fictitious AMC.

As a ground plane, most conventional antennas use the perfect electric conductor (PEC), in practice, a conductive layer as the copper). The antenna's reflector is made up of the PEC layer. As known, the signals bounced back from the PEC have 180^o phase shift (i.e., out of phase) with

the source wave, J, as shown in **Figure 2-10(a**). The source wave is a wave (wave 1) that passes along the antenna's radiating section at first. The out-of-phase reflected wave (wave 2) interferes with the source wave destructively. The source wave from the antenna is cancelled or significantly attenuated as a result of this interference, lowering the antenna's radiation efficiency. Thus, the antenna's gain diminishes. Due to the significant field cancellation, the antenna may not correctly match in this instance. To reduce this influence, the gap separating the main radiator from the ground should be around a quarter wavelength, making the reflected signal has extra 180^o phase shift, see **Figure 2-10**(**b**). The p phase shift of the reflected wave (from the PEC) that will constructively interact with the source wave was used to calculate the relevant distance (from the antenna). Additionally, at the resonant frequency, the impedance matching is improved. The disadvantage of introducing such a gap is that it increases the overall antenna dimensions. As a result, the antenna structure is no longer low-profile, which is a desirable feature in antenna designs, especially in space-constrained situations like microwave circuits in portable devices.

PMC (or AMC in practice), on the other hand, generates reflected waves that are comparable in direction to the original current, with a reflection coefficient of magnitude |Γ| of +1. The reflected wave via AMC is in phase with the source wave, as seen in **Figure 2-10(c**). The additional reflected waves interfere with the original wave in a constructive way. The antenna's radiation efficiency and gain are improved by combining the effects of both reflected and source waves. As a result, a low-profile antenna can be created without the need for a $\lambda/4$ gap between the AMC ground plane and the antenna (as in the case of the PEC ground layer).

Moreover, as illustrated in **Figure 2-11**, AMC only shows unique PMC properties within a limited bandwidth. AMC's bandwidth ranges from $+90^o$ (lower frequency,F_l) to -90^o (higher frequency, f_h), with 0^o serving as the resonant frequency f_r. Z_s of AMC is identical to the impedance of free space at phases of $\pm 90^o$, the magnitude of surface impedance. AMC shows PEC characteristics in the remaining band.

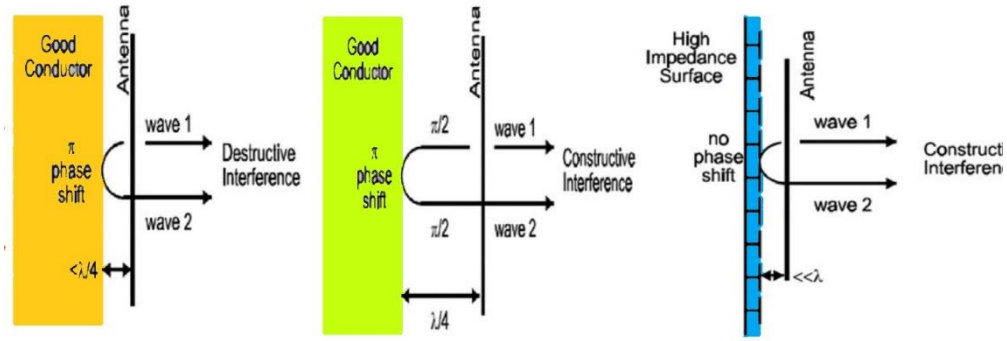

Figure 2-10 Antennas were spaced (a) near together and (b) apart from the ground plane. (c) The ground layer is quite close to the antenna combined with AMC.

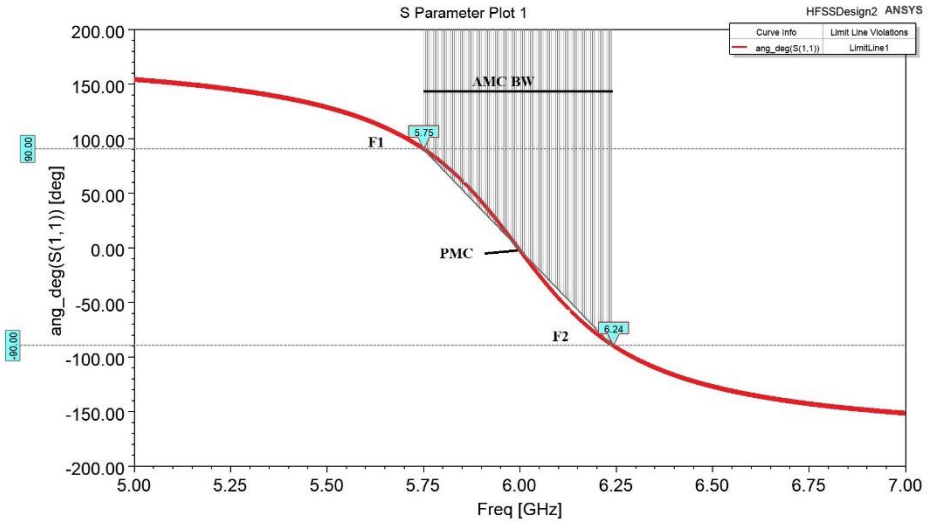

Figure 2-11 Usual reflection phase diagram of AMC.

2.4.2 PIN Diode RF Switches

A switch is an electrical component that is used to open and close circuit connections or to change the connection of a circuit [28]. In the "ON" state, a "Ideal Switch" has zero resistance to current flow and infinite resistance in the "OFF" state. A good switch design has a certain amount of flexibility. In the “ON” state, there is resistance, and in the “OFF” state, there is a finite resistance. The fundamental parameters that describe PIN diode switch performance as fellow:

A-Series SPST (single pole single throw switches) switch

The PIN diode (SPST) can be called the SPST as well. The maximum isolation (ISO) that may be achieved is determined by the capacitance of the diode (C_t). The forward biased series resistance of the diode determines the

insertion loss (I_L) and power dissipation (P_d) (Rs). The performance characteristics, as well as the calculations for ISO and I_L, are listed below.

$$I_L = 20\log\{1 + R_s/2Z_o\} \quad \textbf{2-34}$$

$$I_{SO} = 10\log\{1 + 1/(4\pi f C_t Z_o)^2\} \quad \textbf{2-35}$$

Power dissipation (P_d):

$$P_d = \{4R_s Z_0/(2Z_o + R_s)\}^2 P_{av} \quad \textbf{2-36}$$

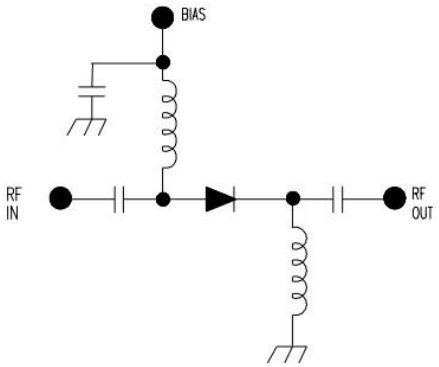

Figure 2-12 Series SPST Switch.

where P_{av} is the maximum available power, $V_g^2/4Z_0$ (Watts).

Only matched SPST switches are included in these equations. P_d is calculated by multiplying these equations by the factor [2 σ / σ + 1], dubbed "sigma," for VSWR (σ) > 1.0.

Peak RF current of the (SPST)

$$I_p = \sqrt{2P_{av}/Z_0} \text{ Amps} \quad \textbf{2-37}$$

Peak RF voltage of the (SPST)

$$V_p = \sqrt{8Z_o P_{av}} \text{ Volts} \quad \textbf{2-38}$$

Multiply the previous calculations by the factor "sigma" if the series SPST switch is not matched.

In a network like the one depicted in Figure 2.10, there are **lumped circuit elements**. There are also equations for computing the comparable L and C values.

$$L = Z_o/2\pi f_o \text{ (H)} \quad \textbf{2-39}$$

$$C = 1/2\pi f_o Z_o \quad (F) \qquad \textbf{2-40}$$

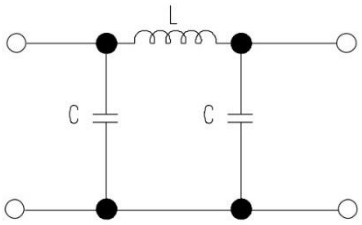

Figure 2-13 Equivalent lumped circuit.

2.5 Smart Antenna (feeding network)

There are two types of smart antenna systems: switched systems and adaptive-array systems. In the switched system the Butler Matrix and the Rotman lens are the widely used ones mainly in OAM antenna, it looks easy to fabricate but it needs more challenge with accurate steps especially in high frequencies to design it. We will be focus on Butler Matrix in this thesis. Butler Matrix BM is the most widely used beamforming network based feeding circuit type. Butler matrix using microstrip transmission lines is easier to implement than Blass Matrix since their implementation is less complex. The standard Butler Matrix [29] is a $2^n \times 2^n$ network with 2^n inputs, 2^n outputs, $2^{n-1} \log 2^n$ hybrids, and numerous phase shifters. It typically contains N number of inputs and N number of outputs to generate N number of orthogonal beams The Butler Matrix is the most well-known configuration which is a 4 x 4 as shown in **Figure 2-14**. However, having the same number of input and output ports may not be necessary. For instance, in [16], the Butler matrix is changed to include just three inputs but four output ports, with the goal of producing three beams, one of which is broadside beams. Butler Matrix can generate N orthogonal beams using N input and M output ports. The number of beams produced by the Butler Matrix is determined by the N number of inputs, whereas the number of radiating elements is determined by the M number of outputs, which affects the beam width size of the main lobe.

The matrix is made up of transmission lines, the dimensions of which are computed using Equation (2-29). It is assumed that is standard value of 50Ω

will be used. 3-dB couplers, 0 dB couplers, and phase shifters are the various components of the Butler matrix. In the parts that follow, these are explained and simulated.

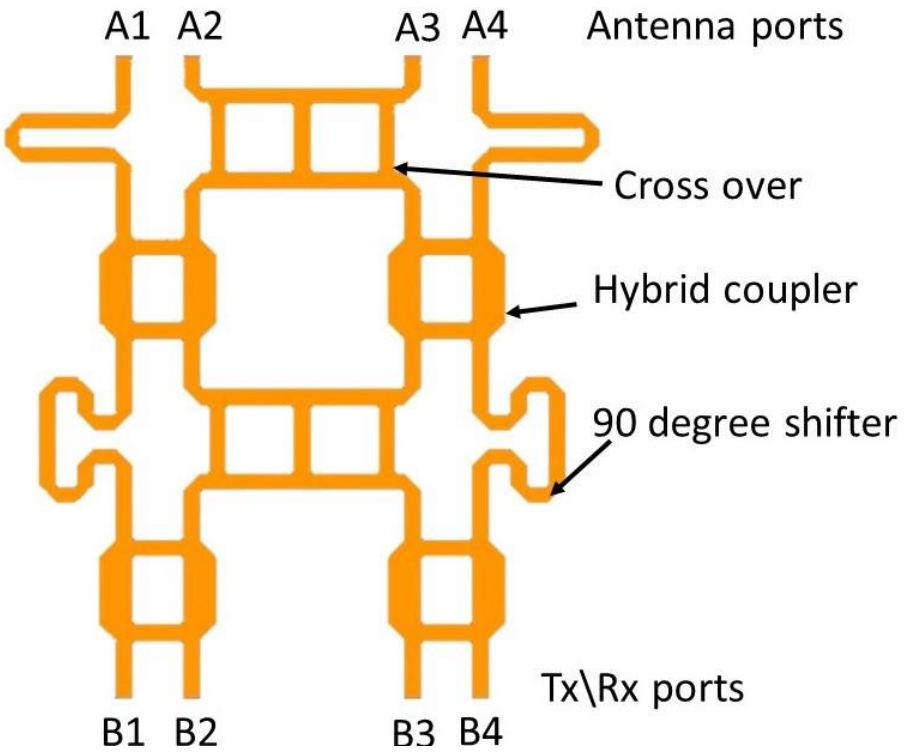

Figure 2-14 Block Diagram of 4 x 4 Butler Matrix [29].

2.5.1 Hybrid Coupler (3-dB couplers)

Quadrature hybrids are 3dB couplers that produce two same outputs that are 90^o degrees out of phase. The layout of a directional coupler is shown in **Figure 2-15**. When all of the ports impedances are equal, the power entering port 1 is evenly distributed across ports 2 and 3, with a 90^o phase shift between them. Because there is no power connected between port 1 and port 4, port 4 is isolated. We can prove [25] that the S-matrix is as follows using even-odd mode analysis:

$$S = \frac{1}{\sqrt{2}}\begin{bmatrix} 0 & j & 1 & 0 \\ j & 0 & 0 & 1 \\ 1 & 0 & 0 & j \\ 0 & 1 & j & 0 \end{bmatrix} \qquad \textbf{2-41}$$

The 90^o hybrid coupler is made up of two main transmission lines that shunt together and are joined by two secondary branch lines. It has two 50Ω

transmission lines and two 35.4Ω transmission lines with lengths of $\lambda/4$. As a result, the square's circumference is roughly equivalent to one wavelength.

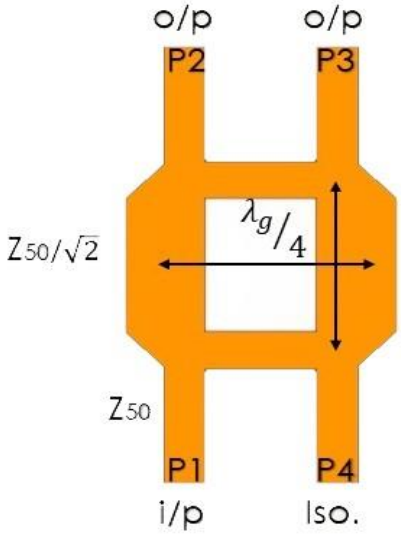

Figure 2-15 Microstrip hybrid coupler design [25].

2.5.2 Crossover Coupler (0 dB couplers)

This component ensures that the two inputs can cross each other without influences. It is also known as 0dB coupling. It further claims that by combining two hybrid couplers, a cross-coupling can be achieved. The geometry used to create this device is shown in **Figure 2-16**, and the matching S matrix [25] can be represented as follows:

$$S = \begin{bmatrix} 0 & 0 & j & 0 \\ 0 & 0 & 0 & j \\ j & 0 & 0 & 0 \\ 0 & j & 0 & 0 \end{bmatrix} \qquad \textbf{2-42}$$

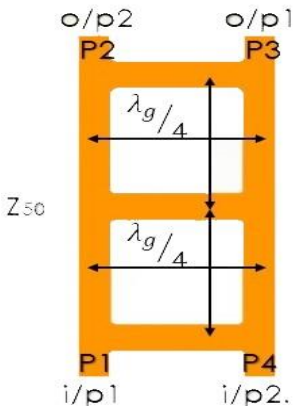

Figure 2-16 Layout of the crossover (0 dB) coupler [25].

2.5.3 Phase Shifters

The notion behind phase shifters depicted in **Figure 2-17** is that a length of the transmission line that can generate a lag phase shift confined between 0^o and 360^o. As a result, a transmission line of length L with this approach gives a phase difference of

$$\varphi = \frac{2\pi}{\lambda} L \qquad \textbf{2-43}$$

where λ is the wavelength. Equation (2-44) is used to compute the effective wavelength

$$\lambda = \frac{\lambda_o}{\sqrt{\epsilon}_{reff}} \qquad \textbf{2-44}$$

Figure 2-17 The phase shift

Chapter 3: Design of Printed Crossed-Dipole Antenna

According to our motivation, and the problem statement, and also the outcome of SWOT analysis in subsection (1.7), we will look for a new modern antenna that can be then used in antenna arrays in the next chapter to generate the OAM waves that never used before, with the circular polarization and high efficiency. Choosing the crossed dipole antenna CDA with enhanced performance is the goal to be carried out in this chapter. This will be very useful as mentioned in the previous chapters. Aim (1.6) will be addressed and it will be the current chapter core.

3.1 Cross dipole antenna

The cross-dipole antenna CDA has attracted a lot of attention among researchers in the last decade owing to its capability to generate almost pure circular polarization at a wide range of frequencies. As known, antennas with circular polarization are in high demand since they can receive and transmit signals at any orientation in space. Thus, mobile wireless communications and satellite applications cannot be indispensible of this type of antennas to guarantee a good connection between two wireless ends. Historically, the CDA was invented in the 1930s, following the invention from Brown which was the first CDA under the name of "turnstile antenna". After that, in 1940s, the "superturnstile" antenna was developed with a wider impedance bandwidth design compared with the previous ones [30]. In the1960s, a new design of the CDA used a single feed, where the CDA had arms with unequal lengths. This aids to balance the phase difference between the two components of electric fields to generate perfect circular polarization signals with an axial ratio close to 0dB. In other words, the condition was that both dipoles had equal real part admittance but different input angle by 90° leading into generation of the circular polarization [31].

3.1.1 CDA application

The most important criteria in the CDA is the circularity of polarization because the circular polarization antennas are the solutions for prohibiting multipath effects and alleviating the polarization mismatch problems as known among the wireless communication community. Here are some

examples using the circular polarization antennas where they are recalled for the sake of integrity such as: navigation satellite system (global position system GPS, broadcasting services BDS and global navigation satellite systems GNSS), wireless local area network (WLAN) [32], radio frequency identification (RFID) [33], and wireless personal area network and worldwide interoperability (WiMax) [34], for microwave access. Therefore, the Cross-dipole antennas are sophisticated for the present and future communication systems. Moreover, the CDA can generate isotropic, dual, omnidirectional radiation patterns with circular polarization capabilities. Also, the cross-dipole antenna is convenient for single, multiband, wideband, and broadband applications [35].

3.1.2 Antenna mechanism

As depicted in **Figure 3-1** and **Figure 3-2**, the antenna is a pair of rectangular arms connected together by the feeding network acting as driven elements. The feeding network consists of a pair of vacant quarter rings [36], and they are used to connect the two cross boomerang arms with $\lambda_g/4$ length (λ_g is the guided wavelength at the design frequency). Each side of the substrate has a single vacant quarter ring printed on its faces. The substrate used in the design has proper thickness with a special type of dielectric. The semi-rigid coaxial cable of 50Ω allows a 180° phase different between the two arms of each dipole. The inner conductor of the SMA is connected to the top arm and the outer conductor is connected to the bottom arm. The ground plane is placed on height H of $0.25\lambda_0$ (λ_0: free space wavelength) from the main radiator. The ground is a metal square shape and its side length is equal to $0.785\lambda_0$, in which this size is optimized to mitigate the ground effects on the antenna performance, with keeping the overall size is acceptable.

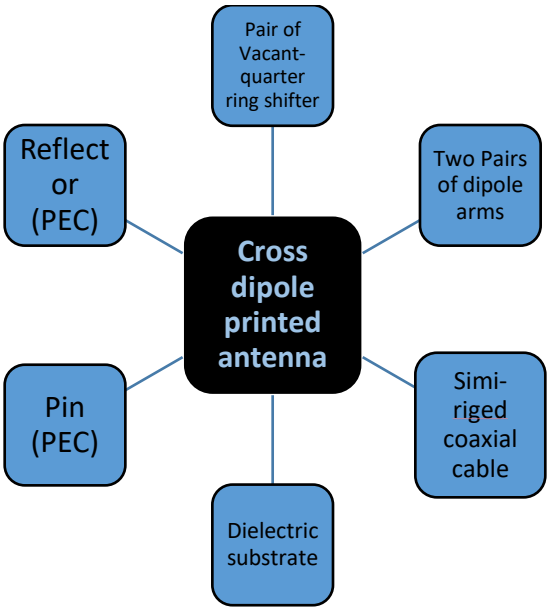

Figure 3-1 Printed cross-dipole antenna parts

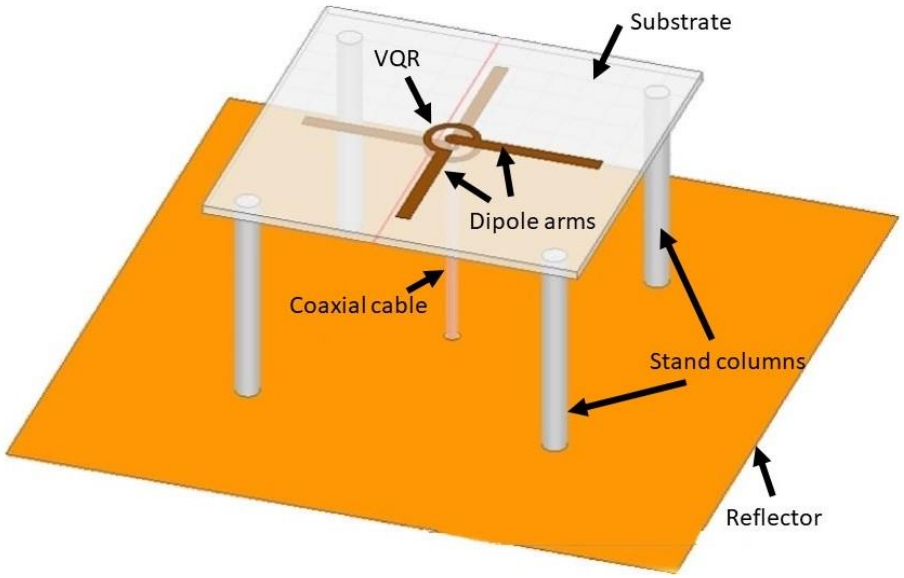

Figure 3-2 Printed cross-dipole antenna assembly configuration

3.1.3 CDA types and Modifications

To make the antenna more usable, several modifications have been made to widen the circular polarization bandwidth using parasitic elements. The CDA was first designed in 2008 with strip-line transmission lines which had 15.6% axial ratio bandwidth ARBW in [36]. The same author proposed, in 2011, the same antenna design with open loop parasitic elements to enhance -10dB the impedance bandwidth IBW and 3dB ARBW [37]. Subsequently, in [38] authors have used a single parasitic cross-loop. A cross strip-dipole with a pair of dipoles to get wide band CP in [39], the same author enhanced

his design by adding four square-slot patches to provide the broadband CP [40]. In [41] authors have used a dual cavity structure to widen the CP wideband. Son Xuat has used in [42] a single cavity and magneto-electric ME, which has good influences on the 3dB AR. Coupled rotated dipoles is presented in [43]. Also, a simple single parasitic element with utilizing a bias circuit to turn on-off the parasitic elements is introduced in [44]. Other types and shapes to design the main arms of cross-dipole antennas to widen the ARBW and IBW were reported in [45]. Authors have used the bowtie shape with two slot-made etched on the main arms to come up with a structure radiating at dual frequencies with the IBW and 3dB-ARBW of 57% and 51%, respectively. In [46], the same shape in the previous reference, the author has utilized four parasitic patches where the results are seemingly enhanced to have the IBW of 47.73% and 3dB ARBW of 42.8%. More enhancements have been obtained on the IBW and ARBW compared to the previous references mentioned above. The obtained IBW and the 3-dB ARBW were 93.1% and 90.9%, respectively. This extraordinary enhancement is owing to using the sequentially rotated feeding lines and unequal cross-slots [47]. In addition, the trapezoidal bowtie CD antennas are presented in [48]. On the other hand, different shapes of radiating cross-dipole antenna arms have been reported as in [49] and are used with the elliptical shape, giving good results in front-to-back ratio FBR, IBW and 3dB ARBW when using the reflector cavity. Moreover, there are more different shapes are presented. All of those antennas are designed for one aim which is to enhance the IBW and the 3dB-ARBW.

3.2 Antennas configuration and results

3.2.1 Individual test for CDA features

To make a confidential worked, we checked every piece forming the proposed CDA to test it individually as follow:

A-Coaxial cable

Referring to subsection (0), the coaxial cable characteristic impedance Z_o in **Figure 3-3** is calculated using Equations (2-20-2-23). We have used the Tefelon with permittivity of 2.1, loss tangent of 0.001, and radiuses of inner

conductor of 0.075mm and outer conductor of 0.28 to get$Z_o = 50\Omega$. Also, the cutoff frequency is determined as 202.6GHz, capacitance is 29.5 pF/ft, inductance is 73.4nH/ft.

The transmission coefficients are high because S21 and S12 are closed to 0dB (i.e., all signals can pass through a line) whereas the return loss is less than -46dB.

(a)

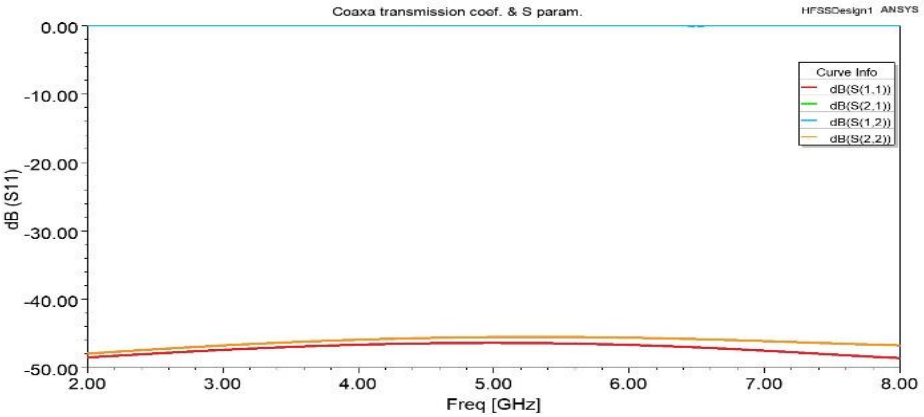

(b)

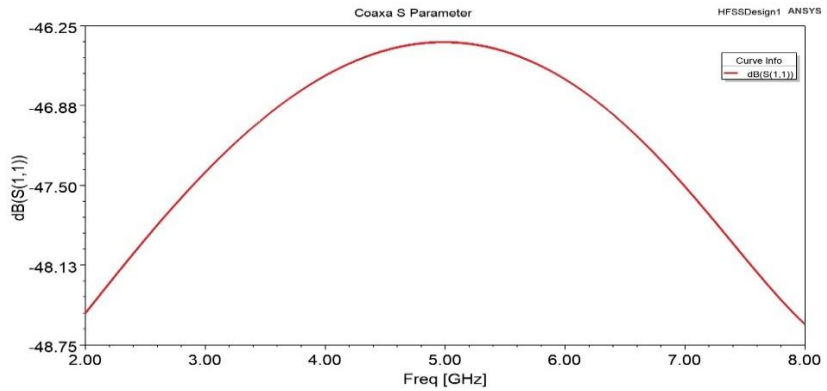

(c)

Figure 3-3 Coaxial cable a) model b) transmission line coefficient c) S parameters.

B- Vacant Quarter Ring

The vacant quarter ring (VQR) is reported in 2008 by Bike [36]. By introducing $\lambda_g/4$ length, the VQR with 0.4mm thickness can introduce the 90 degree lag phase. We have tested it by using the de-embedding property as shown in **Figure 3-4**. The 90 degree lag phase shift is exactly obtained at 6GHz.

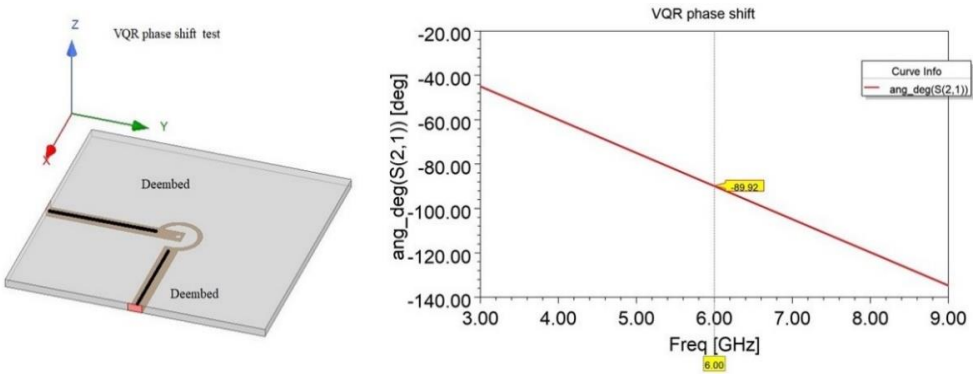

Figure 3-4 VQR with phase shift of the S21 parameter.

C- Rectangular Line Test

The matching impedance is very important to get on good power radiation or power transmission as shown in **Figure 3-5.** We have high transmission coefficient S21 closed to zero dB and return loss less than -36dB. The transmission line width parameter is 0.93mm for the substrate type used in the simulation, which in turn, depends on a height and dielectric constant of the substrate. These two factors can also govern many other design properties which are not mentioned here for the sake of simplicity. In the simulation, permittivity of the dielectric(ε_r) is 4.4 and the substrate thickness h is 0.5mm.

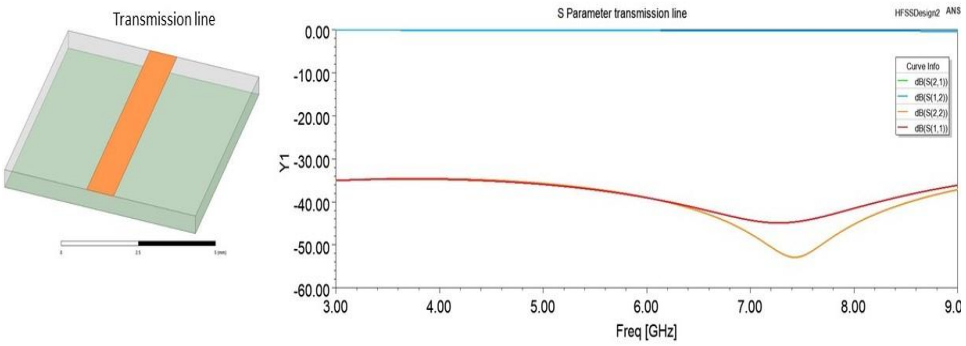

Figure 3-5 the transmission line coefficient and return loss.

3.2.2 Integration of the CDA

According to advantages of the CDA mentioned earlier, several structures adopted the classic form are studied [36]. Wideband CDA has recently introduced as a result of various modifications to the conventional form, including addition of the parasitic elements [40]–[44], [46]– [51] . Here, we start with the tradition form (rectangular shape) as depicted in **Figure 3-6** with dimensions given in **Table 3-1.** As can be seen, antenna **I-R** means antenna number one in the rectangular family.

The antenna is designed at 6 GHz where$\lambda_o = 50\,mm$. It is made up of two orthogonally aligned straight dipoles, referring to the subsection (3.1.2). The

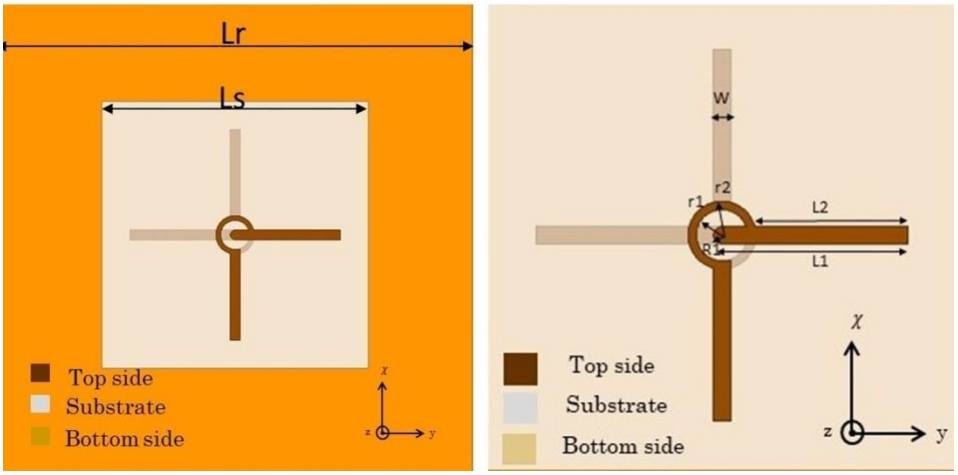

Figure 3-6 Dimension parameters of CDA (top view) antenna I.

arms of the dipole are printed on the two sides of a FR4 substrate with a thickness of 0.5 mm ((ε_r) = 4.4, tan = 0.02) and is immediately connected by the semi-rigid coaxial cable of 50Ω which allows to obtain a 180° phase difference between two arms of each dipole. The antenna structure was modeled with the help of the High Frequency Structure Simulator by Ansoft Inc. The (HFSS) relies on the finite element method FEM algorithm to analyze designs.

The results show a wide IBW of 32.21% from 5.34 to 7.39 GHz and a narrow ARBW of 14.15% from 5.58 to 6.66 GHz. The CDA gain is 7.4 dB

Table 3-1 A summary of the antenna dimensions (unit: mm)

Lr	**Ls**	**W**	**r1**	**r2**
39.25	22	0.8	1.2	1.6
L1	**L2**	**R1**	**H**	
8.7	7.15	0.4	12.5	

and the efficiency is 97.37%, see **Figure 3-7**.

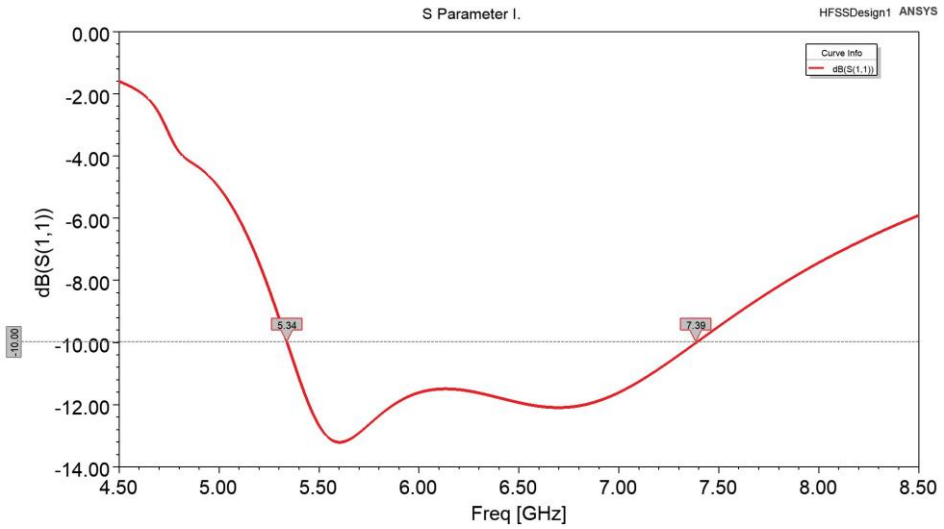

(a)

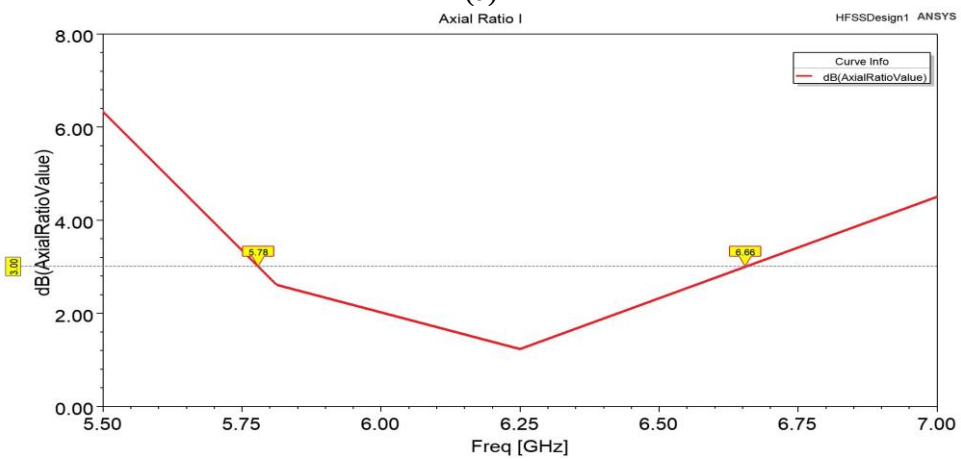

(b)

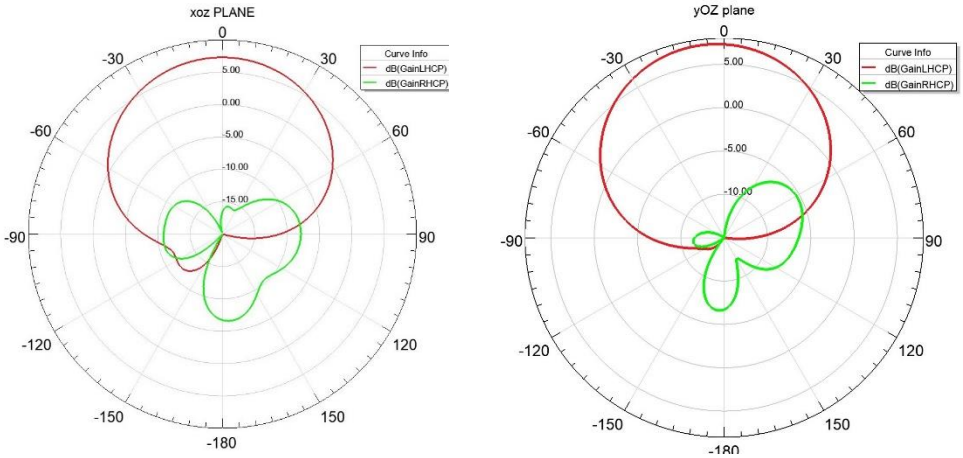

(c) (d)

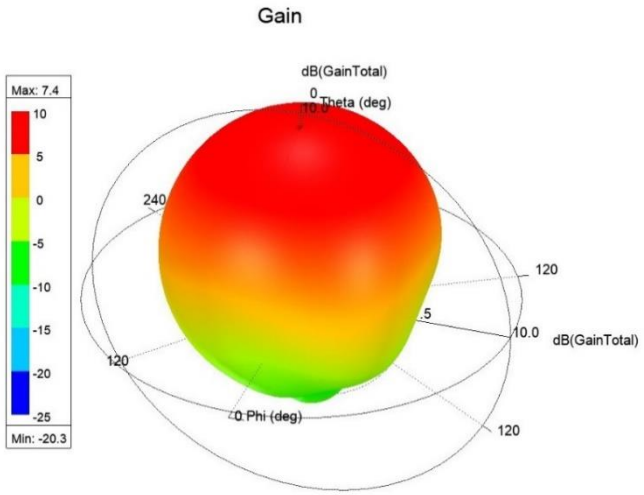

(e)

Figure 3-7 Simulated results of the antenna I (a)RL (b) AR (c) (d)two plane radiation patterns (co-polarization and cross-polarization) (e) 3D gain plot.

Figure 3-7 (c) and (d) shows the simulated radiation patterns at 6 GHz in xoz-plane and yoz-planes.The patterns in xoz-plane are symmetrical to those in yoz-plane. The antenna generates unidirectional CP patterns in a boresight direction. The right-hand circular polarization (RHCP) is higher than the left-hand circular polarization (LHCP) by 24 dB, generating exceptional RHCP radiation.

The evolution of all proposed antennas presented here is demonstrated precedingly to show up the mechanism for improving bandwidths. The first step in the design is to make the antenna having good matching at the design frequency. A mechanism of the impedance matching is qualitatively, where

the equivalent circuit model of the antenna is provided in **Figure 3-8**. The symbol Yin characterizes the total input admittance of the proposed antennas, YA means the antenna without the interlaced rectangular patches, whereas $C1$ and $C2$ mean the parallel-plate capacitors as seen in **Figure 3-9**.

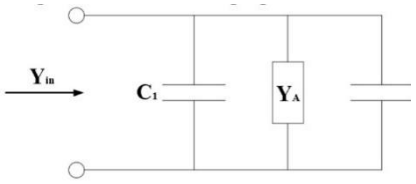

Figure 3-8 Equivalent circuit model of the antennas.

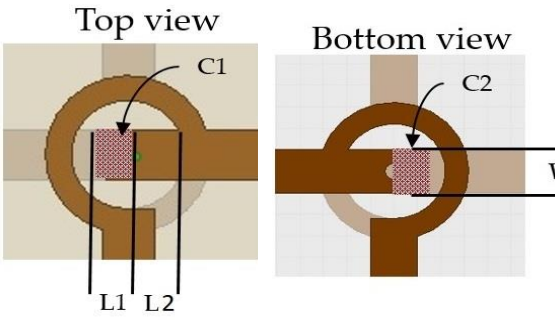

Figure 3-9 Structure of overlapped rectangular patch: (a) top view, (b) bottom view.

The capacitance of parallel-plate capacitors $C1$ and $C2$ can be considered when the density of electrical charge on the plates is uniform, where the fringing fields at the edges are ignored. From **Figure 3-9**, the input admittance of the proposed antennas can be indicated by:

$$Yin = YA + j\omega(C1 + C2) \approx YA + 1\ \frac{2j\omega\varepsilon_r\varepsilon_o\, WL1}{h} \qquad \textbf{3-1}$$

The approximation is derived from the small slot on the rectangular bottom patch that reduces the overlapping area of the condensers of the two parallel plates. It is shown in Equation (3-1) that the rectangular patch width W and length L1 define the antenna input admittance Yin. Therefore, these two parameters can be tuned to get the required impedance characteristic of the antenna to achieve a good impedance matching. However, the rectangular stub is widen the -10dB-IBW by 190 MHz as shown in **Figure 3-10**, called the antenna **II** in the rectangular family.

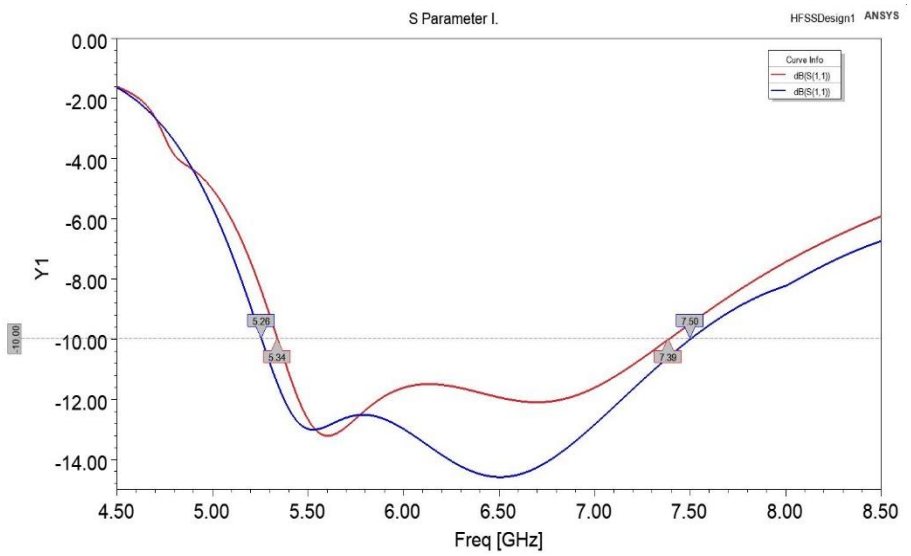

Figure 3-10 Antenna II with rectangular stub.

Because we are looking for antenna that introduces wide IBW with less arm lengths compared with all others proposed CDA, the antenna should be more compact. This feature enables our antenna to be a good candidate to be utilized in antenna array since it reduces the mutual coupling and increases the gain in the antenna arrays. The **Boomerang** shape is designed and simulated to be a new shape that will be added to the CDA shapes list.

3.2.3 Parametric Study

The CDA results for designs mentioned above come from the microwave calculations but also it come from the parametric study to the most important antenna's parameters such as the physical length and width as follows in figures below: see **Figure 3-11**, **3-12**, and **3-13**

- Physical length of the dipole arm.

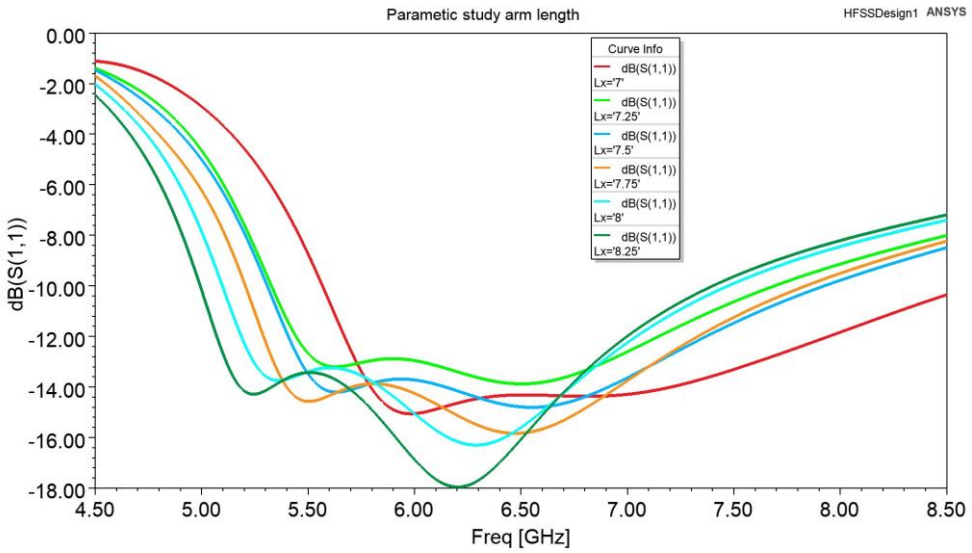

Figure 3-11 L1 arm's length parametric study.

- Width of the dipole arm.

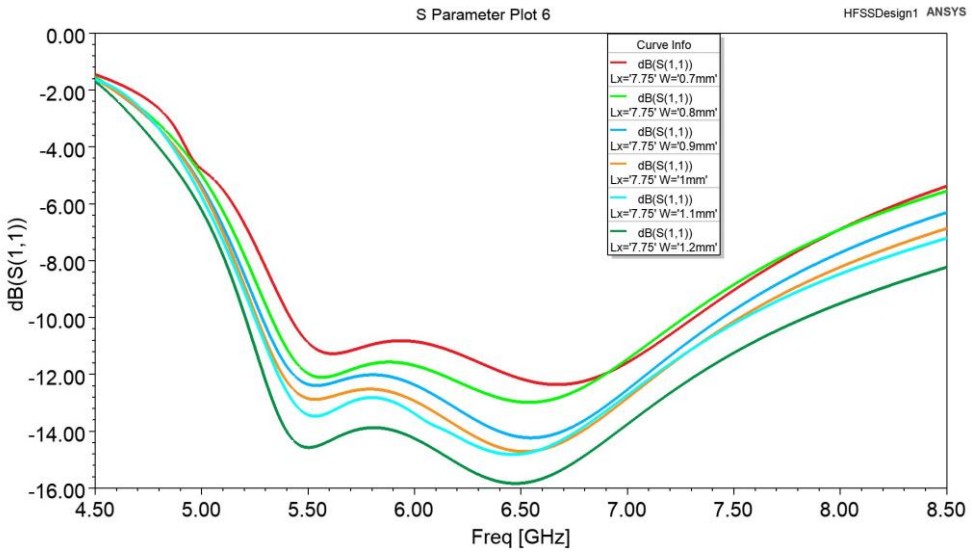

Figure 3-12 W the rectangular width parametric study.

- Vacant quarter ring width (i.e., increasing or decreasing the width of the strip effects on the VQR length because it is a ring).

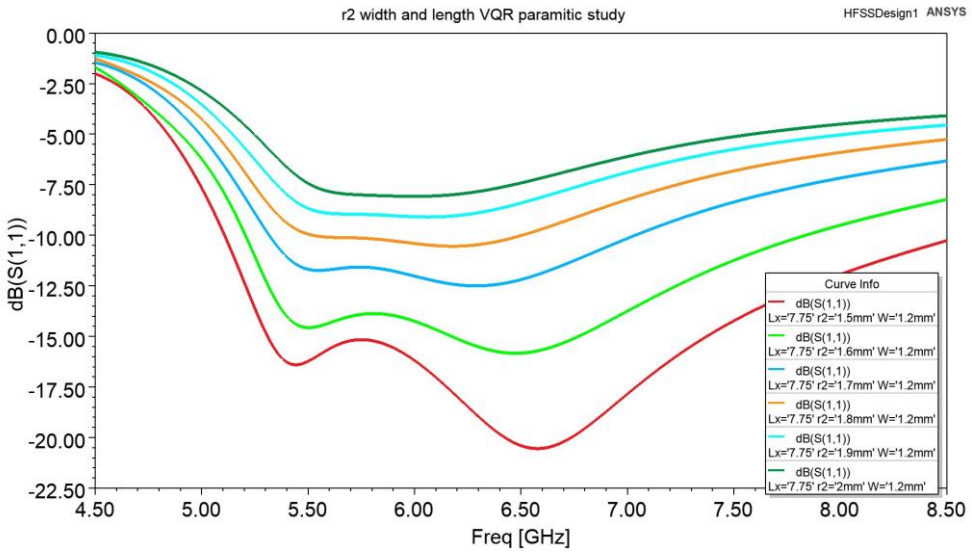

Figure 3-13 r2 width and length VQR parametric study.

Typically, if we want to have the best results, the structures should be optimized. In other words, this can be said that all parameters affecting the performance should be optimized separately and then together. As a consequence, we have made a trade-off between all the results to obtain the good matching.

3.2.4 Boomerang Shape

Here, the boomerang shapes to design dipole arms are employed. As will be seen later, the boomerang arms aid to make the structure resonating at several frequencies and leading into a wideband structure compared to other CDA designs. The multi-resonance phenomenon belongs into the coupling between ends of each arm.

- It is new idea has been taken from the boomerang stick.
- Draw by AutoCAD and then HFSS software.
- Reduce the horizontal arm length.
- It will be more attractive with antenna arrays.
- More efficient than the strip line.

See **Figure 3-14.**

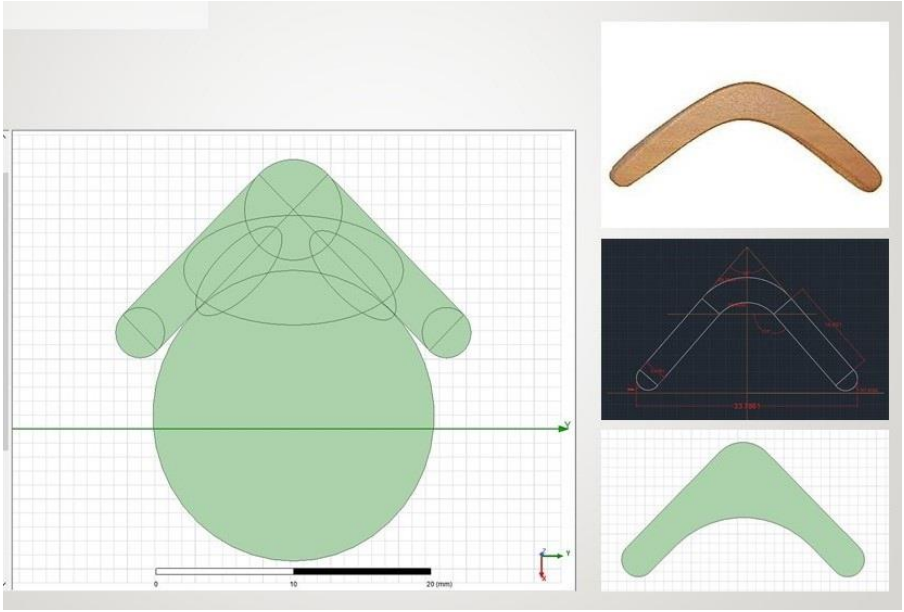

Figure 3-14 The structure of Boomerang shape design.

As depicted in **Figure 3-15** and introduced in **Table 3-2**, the antenna No. **III** is a pair of boomerang arms connected together by the feeding network as driven elements. The feeding network consists of a pair of vacant quarter rings [36], and they are used to connect the two cross boomerang arms with $\lambda_g/4$ length (λ_g is the guided wavelength at the design frequency). Each side of the substrate has a single vacant quarter ring printed on its faces. The substrate used in the design has 0.5mm thickness where its type is FR4 (ε_r is 4.4 with loss tangent of 0.02). The semi-rigid coaxial cable of 50Ω allows a 180° phase-difference between the two arms of each dipole. The inner conductor of the SMA is connected to the top arm and the outer conductor is connected to the bottom arm. The ground plane is placed on height H of $0.25\lambda_0$ (λ_0: free space wavelength at 6GHz) from the main radiator. The ground is a square shape and its side length Lr is equal to 0.785 λ_0, in which this size is optimized to mitigate the ground effects on the antenna performance, while keeping the overall size acceptable. **Table 3-2** summarizes the antenna dimensions.

Table 3-2 A summary of the antenna dimensions III (unit: mm).

Lr	Ls	W1	W2	L1	L2
39.25	22	1	0.95	2.3	3.55
r1	r2	Rb1	Rb2	Rb3	H
1.1	1.6	2.6	0.9	0.45	12.5

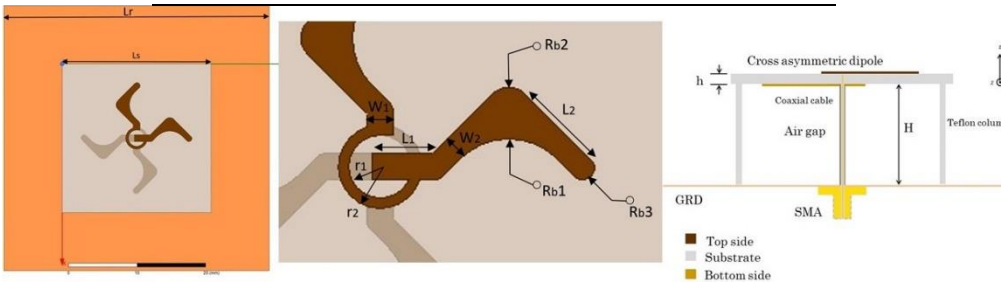

Figure 3-15 The geometrical structure of the proposed antenna iii showing the top view and the magnifying view of arms on the top with side view from right to left.

The -10dB IBW is 2.24GHz with a center frequency of 6.38GHz and 3dB ARBW is 0.63GHz with a center frequency of 5.9GHz. Moreover, the most important property is the craving shape that introduces 25% length reduction than all the other CDA shapes as depicted in **Figure 3-16**, there is a 2 mm reduction arm's length from both sides of CDA arms, comparing with the strip arm which has 7.75 mm length. This reduction form is very useful in antenna arrays to increase space between antennas which in turn reduces the mutual coupling and increase the antenna efficiency. This antenna will be antenna **III,** -10dB IBW of 42.47% (5.1-7.85GHz) and the 3dB ARBW of 7.72% (5.85-6.32GHz). In addition to that, the simulated gain was about 7.4dBi with efficiency of 97.37%, and the overall size is about (0.18 ×0.18 ×0.27λ_0). See **Error! Reference source not found.**.

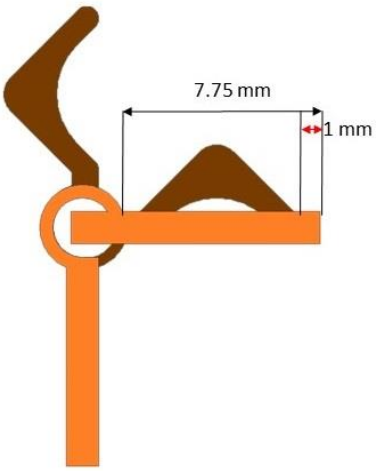

Figure 3-16 The Boomerang shape reduction length of CDA by 25% from any opposite two sides.

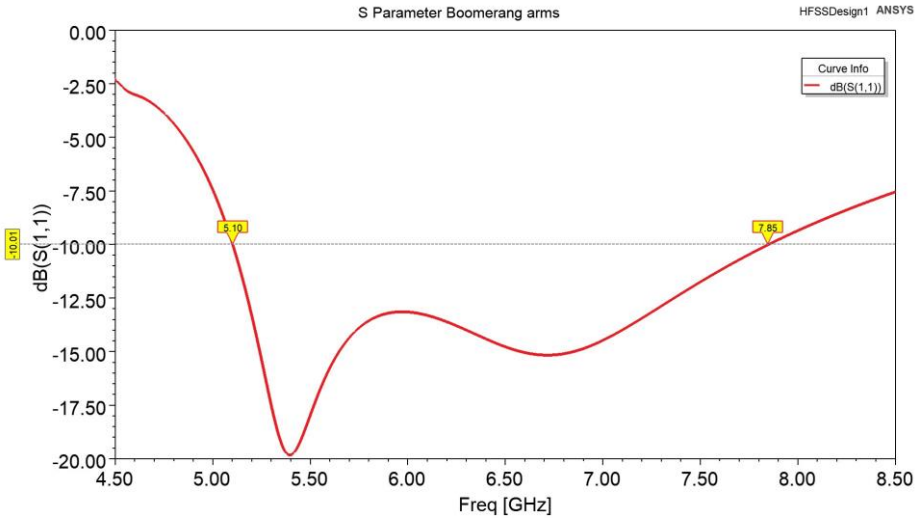

(a)

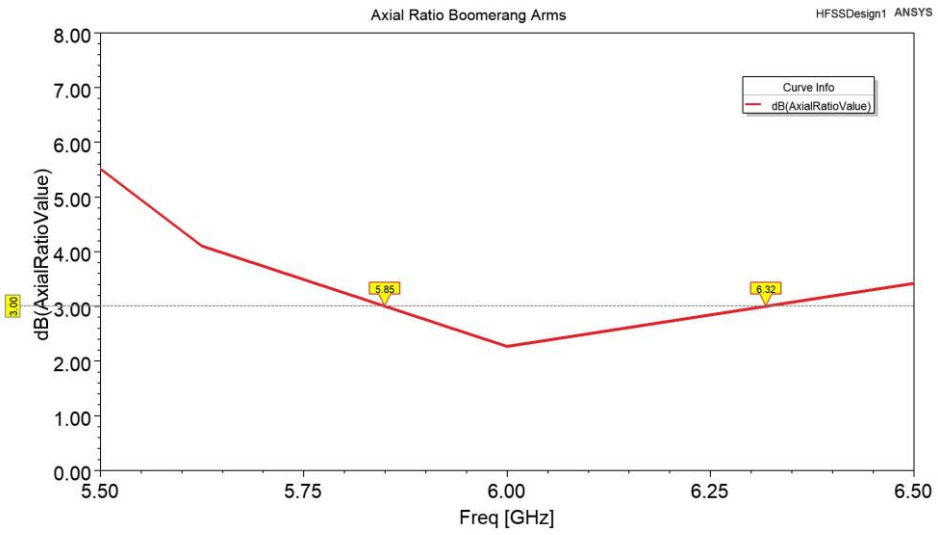

(b)

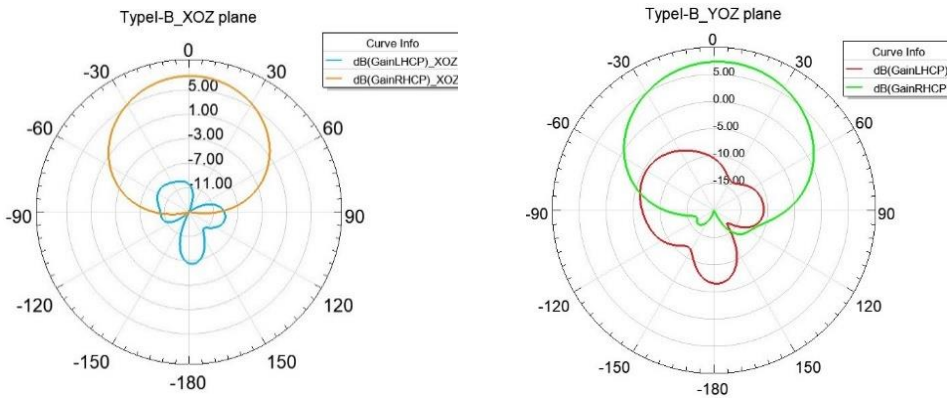

(c) (d)

Figure 3-17 Simulated results of the antenna III (a)RL (b) AR (c) and (d)two plane radiation pattern.

3.3 Antenna Enhancements

Now as a result, we have prepared three CDA traditional (rectangular) shapes with circular stubs and with square stubs. Also, we prepared new shape (boomerang) that it will be entered to the CDA-CP world because the enhancements and modifications are necessary. AMC and Wall perfect electric PEC could improve the antenna performance and miniaturize the overall dimensions, especially one of the disadvantages of CDA that it is a high profile antenna. Then, other CDAs with different modifications have been prepared within those two families of the CDAs (rectangular &boomerang) arms. Finally, we will compare between the two families and also compare the results with other reported in the literature table.

3.3.1 Cavity Reflector

To create a single square cavity, four conducting walls are inserted as rim borders. A cavity-backed antenna's radiation is a mixture of two radiators, including the original exciter and the cavity's rim edges. The rim is excited up when the primary radiator is turned on. Radiation coupling excites the edges, which is followed by a radiating process. A secondary radiator is generated by the aperture made by the rim edges. In [41], it has pointed out that this secondary radiator is able to improve the antenna's performance, where the pattern is more stable and has a bigger broadside gain compared with those of a traditional reflector that does not have rim edges.

Figure 3-18 depicts for both antennas families (rectangular and boomerang) that have same dimensions with side walls height (H_{cavity}) of $0.9*\lambda_o/4$ which it equal to 11.25mm.

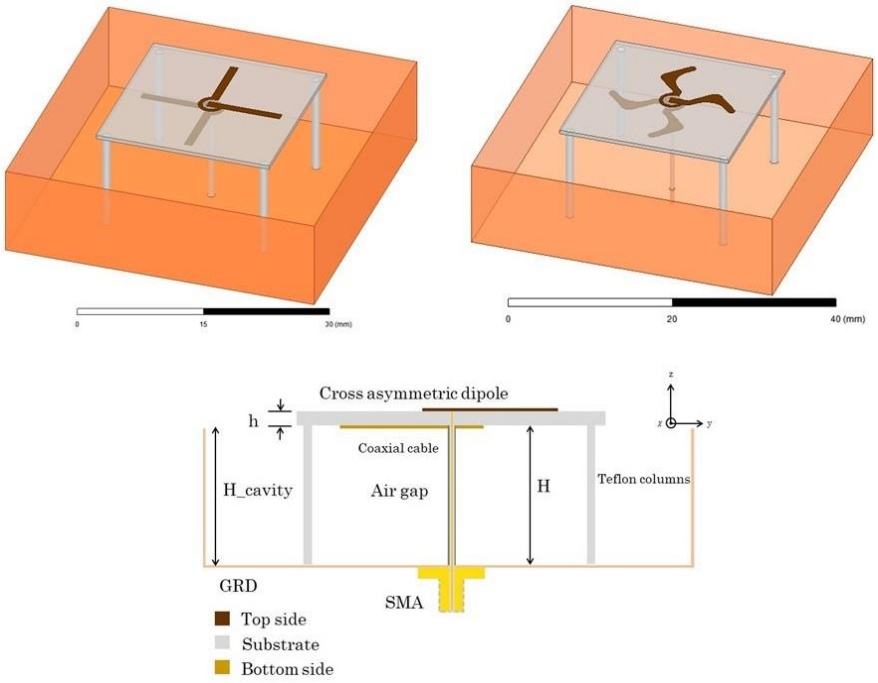

Figure 3-18 CDA models the two families on top right antenna IV and on left antenna V and side view of cavity reflector for both in bottom.

Both antennas have the same dimensions with four metal side walls to create the cavity, but the only one that is fabricated and tested is the CDA with boomerang arms.

A- CDA-Cavity Reflector the Stimulation and the Measurements Results

The CDA with square-box cavity is analyzed where the back-lobe radiation is highly attenuated. In other words, this structure can offer better back-lobe reduction compared to the CDA that has only sheet reflector (i.e., flat ground plane). This increases the efficiency which is primariy factor due to suppressing the surface waves and blocking the diffracted waves produced at edges of the flat ground. Thus, the antenna from the boomerang family with a metal cavity introduces very good results with wideband impedance bandwidth -10dB-IBW of 50.37% (5.08-8.5GHz) and the 3dB-ARBW of 26.4% (5.72-7.46GHz). The simulated gain was about 8.3dBi with an

efficiency of 97.65%, as shown in **Figure 3-19 (b)**. There is no change in the overall size, whereas for the antenna from the rectangular family introduces also very good results with wideband impedance bandwidth -10dB-IBW of 42.27% (5.28-8.11GHz) and the 3dB ARBW of 10.58% (5.73-6.37GHz). The simulated gain was about 8.4dBi with an efficiency of 97.67%, as shown in **Figure 3-19 (a)**. Also, there is no change in the overall size.

B- Compassion Results between the Two Stimulated Families

The return loss is more than -14dB for the boomerang dipoles comparing with the return loss (S_{11}) more than -12 dB for the rectangular dipoles. We have 0.5GHz additional bandwidth in with the boomerang arms compering to the traditional one (rectangular). The -10dB-IBW and 3dB-AR are larger and with additional bandwidth and higher return loss in the boomerang shape which are 1.1 GHz IBW and 1.14 GHz AR. Meanwhile, the radiation pattern is uniform shape and wide difference between the LHCP and the RHCP as shown in **Figure 3-20**. The difference is 26 dB and 15 dB in boomerang and rectangular dipole shapes, respectively. As known, the desired component in the radiation pattern is called the co-polarization component, whereas the undesired one is called as the cross-polarization component. Always, researchers interested in the analysis of antenna structures seek to find what antenna parts can cause the undesired components and how they can be avoided.

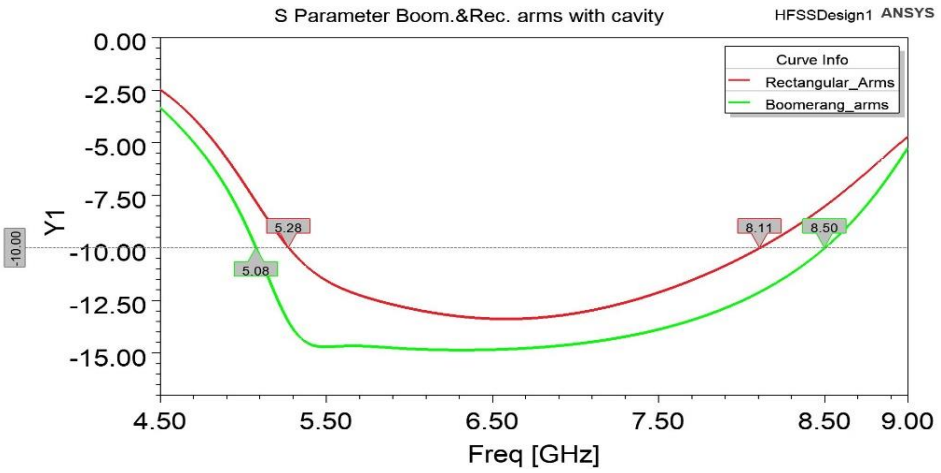

(a)

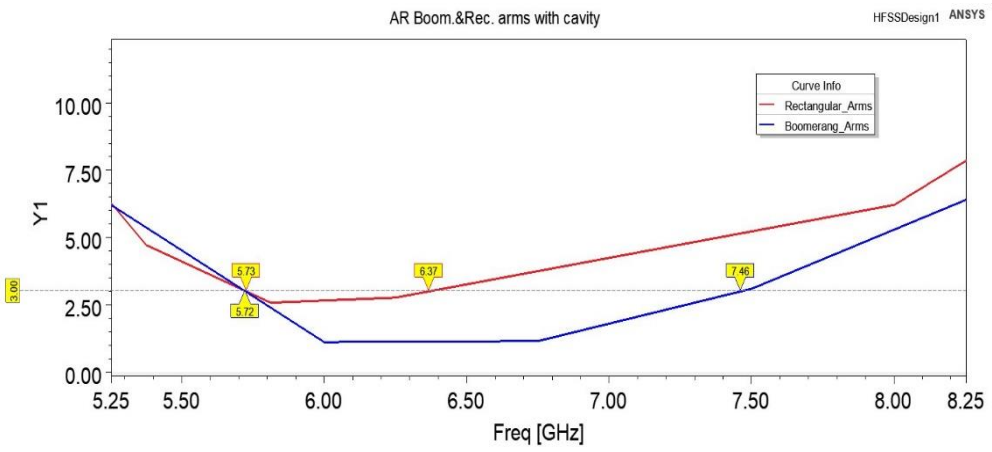

(b)

Figure 3-19 Rectangular IV and boomerang V arms the (a) RL and (b) AR.

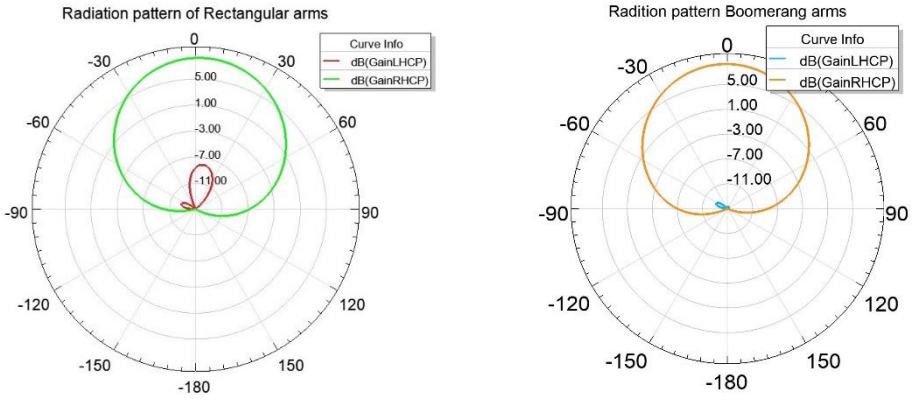

(a) (b)

Figure 3-20 Radiation patterns of antenna with cavity reflector (a) Rectangular arms IV (RHCP is cross-polarization and LHCP is co-polarization) (b) Boomerang arms (LHCP is cross-polarization and RHCP is co-polarization) V.

Therefore, we have a unique antenna even when compare it with other works in the next subsections. These efforts lead us to **fabricate** and **tested** by the specialist. We have made parametric studies for the cavity size as seen in **Figure 3-21.** As can be seen, the IBW does not widely change when the side length of the square cavity Lr is varied from 37mm to 40mm with a step of 0.5mm.

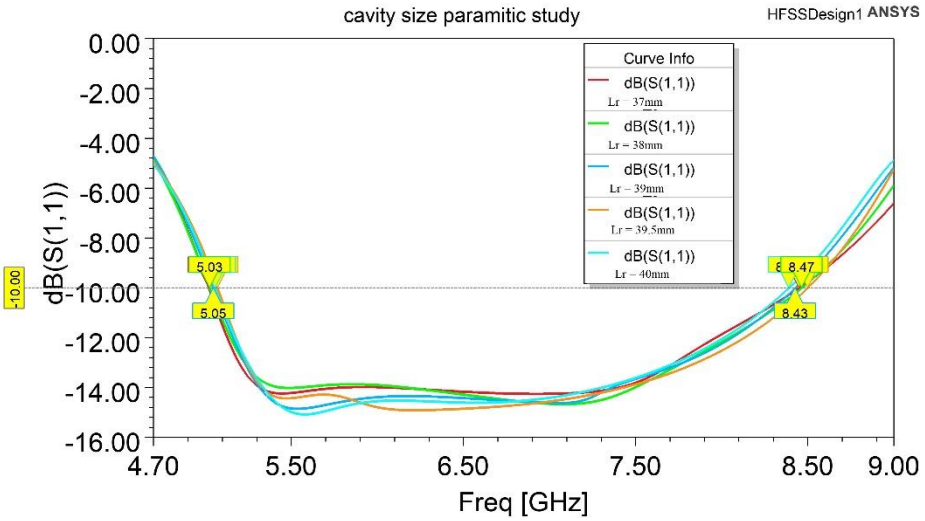

Figure 3-21 Parametric study for the side length of the cavity size Lr of the ground dimensions of antenna V.

C- Compassion Results between Stimulations and Measurements Results of the Boomerang Dipole Shape Antenna V.

The fabrication and test have done at National University of Sciences and Technology NUST in the Islamic Republic of Pakistan. The **Figure 3-22** is fabrication stages and the **design** under test in the anechoic chamber as well. There is a very good agreement between the stimulation and measurement results as shown in **Figure 3-23**.

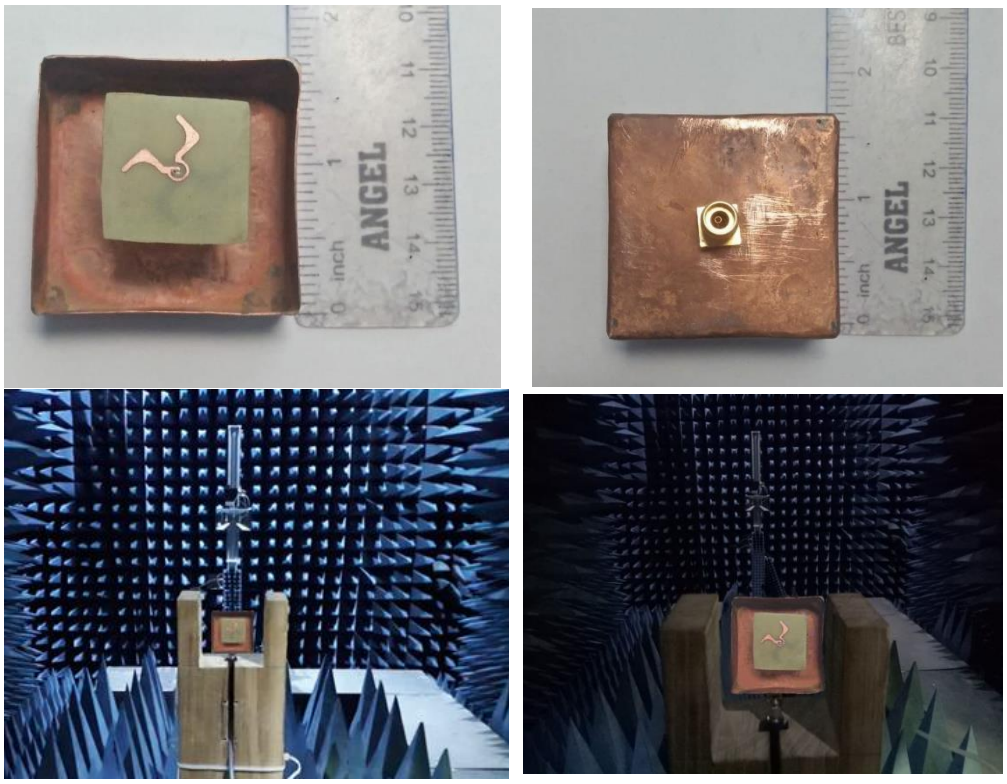

Figure 3-22 CDA Boomerang dipole arms with cavity reflector fabrication and test antenna V.

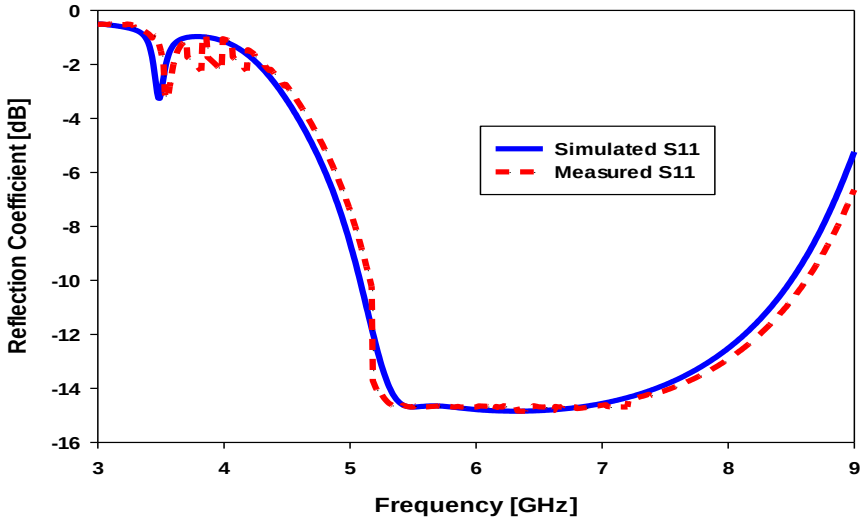

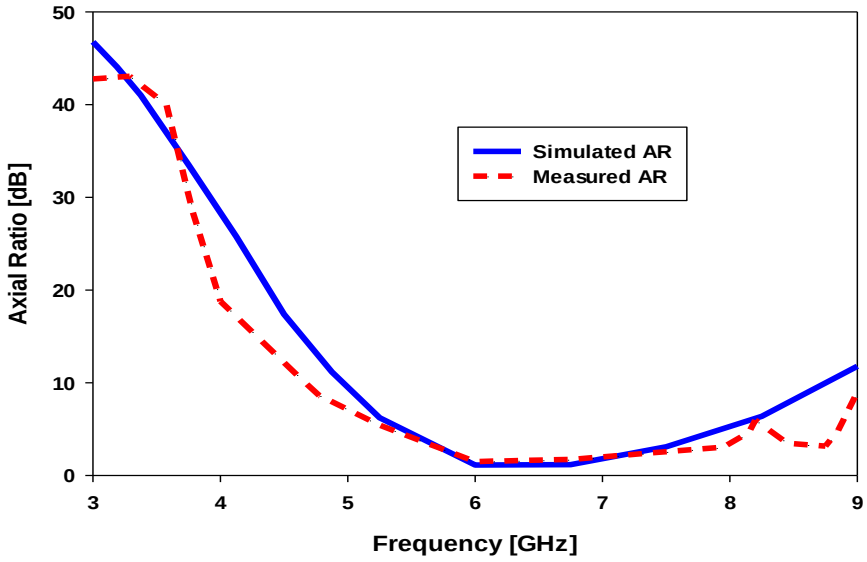

Figure 3-23 The stimulation and measurement -10dB IBW and 3dB AR antenna V.

The slight difference between the measured and simulated results belongs for many reasons, but the main one is because of the fabrication errors. The measured -10dB-IBW of 50.27% is from 5.15GHz to 8.55GHz and the 3dB-ARBW of 28.4% is from 5.74GHz to 7.86GHz. Both measured IBW and ARBW are larger than the simulated one. However, the gain and efficiency are 7.9dB and 94.04%, respectively, in which both of them are lower than the simulated ones.

3.3.2 Artificial magnetic conductor AMC

A- AMC Conception

Artificial Magnetic Conductor (AMC) is one of the metamaterial structures that have been used in a variety of antennas, applied electromagnetic, and microwave applications. This structure is able to reflect the incident signals with zero phase shifts in contrast to the conventional metallic reflectors that add 180-degree phase shift to the signals bounced off them. The AMC behaves as parallel circuit resonator offering on open circuit impedance at the resonance. Also, the AMC surfaces impede the surface currents to flow through them. This feature enhances especially the antenna array performance due to reducing the mutual coupling. Both these two features are exploited to leverage the antenna design in our research thesis. As a fact, no material in nature can offer this type of structures, so it should by

artificially synthesized. It consists of a metal patch placed over the ground separated by thin dielectric and connected by a metallic via, constructing one unit cell. This unit cell is repeated in two dimensions to form the whole design. For more detail, interested readers can refer to subsection (2.4.1). The artificial magnetic conductor AMC is presented in the literature with the cross-dipole antennas to reduce the height which is equal to a quarter wavelengths in the conventional CDA. Using the AMC operates to alleviate the need to add this space between dipole's arms and the ground to make the interference between signal radiating from the dipole's arms and bouncing from the ground constructive. Then, the AMC has in-phase reflection, leading into adding the arms and ground adjacently. Additionally, the AMC gives new resonant frequencies, improving the impedance bandwidth [27], [50].

B- The Proposed AMC Structure

As shown in **Figure 3-24 (a)**, it produces more consistent pattern and greater gain with a comparison to traditional reflector patterns [41]-[52]. The enhancement is because of the use of the artificial magnetic conductor AMC. The AMC surface consists of 7×7 unit-cells, printed on the top side of the lower substrate, with a thickness of 0.708mm where the martial type is Rogers RT/duroid 6010/6010LM (tm) ($\varepsilon r = 10.2$ and $\tan\delta = 0.0023$). Each unit-cell has a side length of Wc=6mm about $0.12\lambda_0$, the spacing between the cells is Ws= 0.5mm and the edge spacing is We= 0.25mm. Then, the overall reflector size is 46×46 mm^2. The AMC reflector is placed with a height of H_{AMC}=6mm about $0.12\lambda_0$ less by 50% than the antenna **I**, **II** and **III** in the vertical dimension. This is one of the aims to use the AMC surfaces (i.e., to make a low prfile antenna) [27], see **Figure 3-24 (b).**

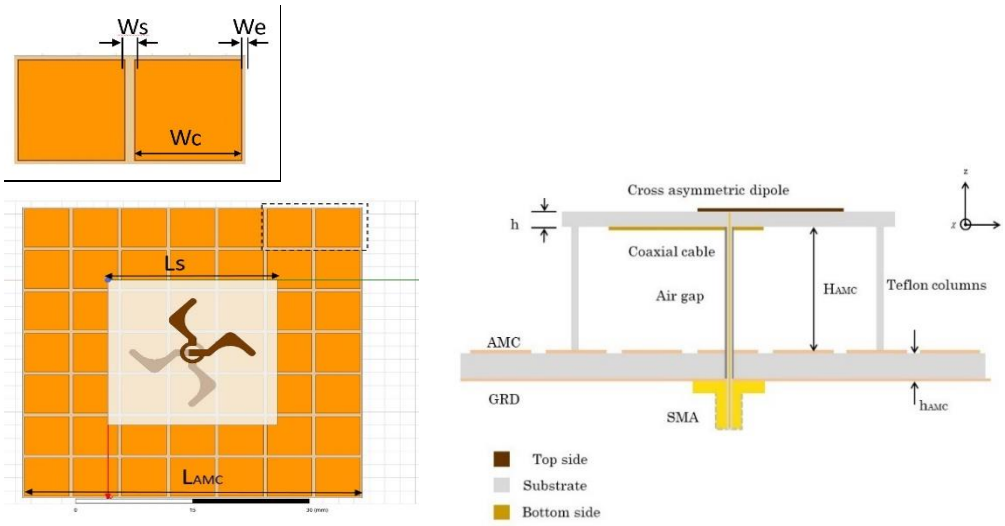

(a) (b)

Figure 3-24 The proposed antenna VI (a) top view (b) side view.

The proposed antenna **VI** is studied numerically to obtain its results. Before integrating the conventional CDA into the AMC, we should analyze and check the performance of the AMC layer. To do so, a single unit-cell is placed in a cavity structure to mimic its periodicity. This method aids to decrease the solution time and offers results close to the original structure. The AMC unit-cell can be modeled as an identical parallel LC resonator with a resonant frequency of f =1/(2π(LC)^1/2), here C and L represent equivalent capacitance and inductance, respectively. The range of acceptable phases offered by the AMC is from –90° to 90° [27]. **Figure 3-25** shows the reflection phase of the AMC structure. For further analysis of the parameter effect on the reflection phase, complete numerical analysis of the AMC cell has been conducted by simulation software HFSS **Floquet Ports**. As can be seen, this phase range can cover a wideband of frequencies.

C- Antenna VI Results

The -10 dB IBW is 38.19% (5.36-7.89GHz) and the 3dB ARBW is about 15.16% (5.79-6.74GHz). The vertical size was reduced to half, thanks to the use of the AMC layer. It is clear that the efficiency a little bit less than the efficiency of the Antenna **III** but all other parameters are better. Generally, the AMC layer considers lossy type because of its high permittivity, but we

can obviously see the enhancement in CP-AR bandwidth, as shown in **Figure 3-25**.

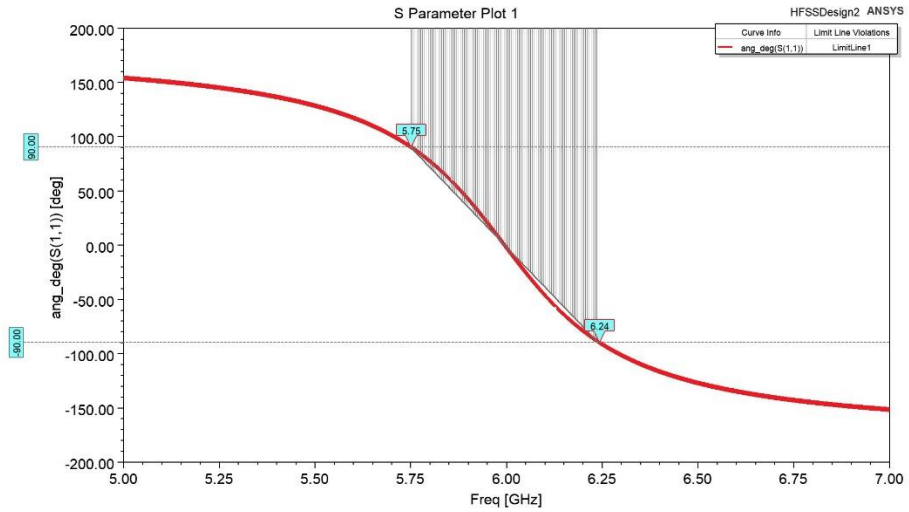

Figure 3-25 Reflection phase of the AMC structure.

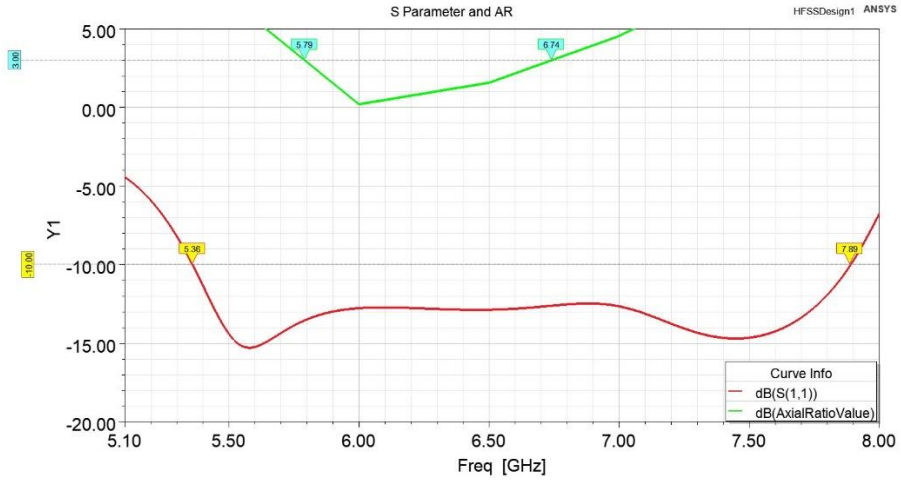

Figure 3-26 Simulated results of the antenna VI, RL and AR.

Figure 3-27 shows the simulated radiation patterns at 6 GHz in xoz-plane and yoz-planes.The patterns in xoz-plane are symmetrical to those in yoz-plane. The antenna generates unidirectional CP patterns in a boresight direction. The right-hand circular polarization (RHCP) is higher than the left-hand circular polarization (LHCP), generating exceptional RHCP radiation.

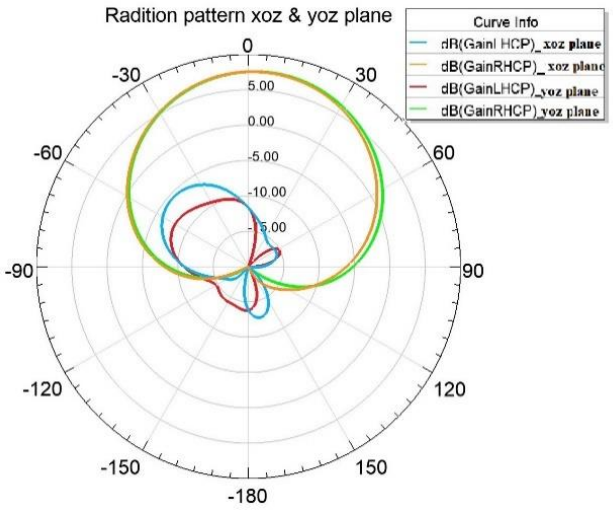

Figure 3-27 Simulated radiation pattern xoz and yoz planes of the proposed CP CDA antenna VI at 6 GHz.

3.3.3 Reconfigurable CDA

By regulating the PIN diodes, a reconfigurable antenna is presented that may be used to broadcast or receive diverse modes and instances of electromagnetic wave EM. To control the transmitting EM wave states, the feeding network has four PIN diodes, all of which are coupled to the biasing circuit.

A- The Parameters of PIN Diode

We will focus on the new CDA shape (Boomerang) to make a new reconfigurable antenna by using PIN diode according to subsection **(2.4.2**) and **Figure 2-12** Series SPST Switch. Has been placed in a gap engraved in a middle of the transmission line to test the PIN diode using the SPICE equivalent circuit with parameter values in the **Table 3-3** and **Figure 3-28** below.

The S parameters (S11and S22) are closed to 0dB in the OFF state while

Table 3-3 PIN diode parameters values.

PIN diode parameters	On state	Off state
R_s		15KΩ
C_p		0.32 fF
R_f	1Ω	
L_f	0.15 nH	0.15 nH

S21 and S12 close to 0dB in the ON state where a model and the results are displayed in **Figure 3-29,**

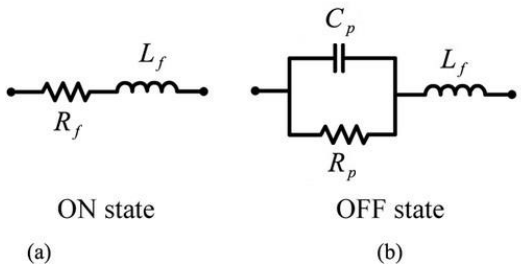

Figure 3-28 The equivalent circuit EC of PIN diode (a) ON state (b) OFF state.

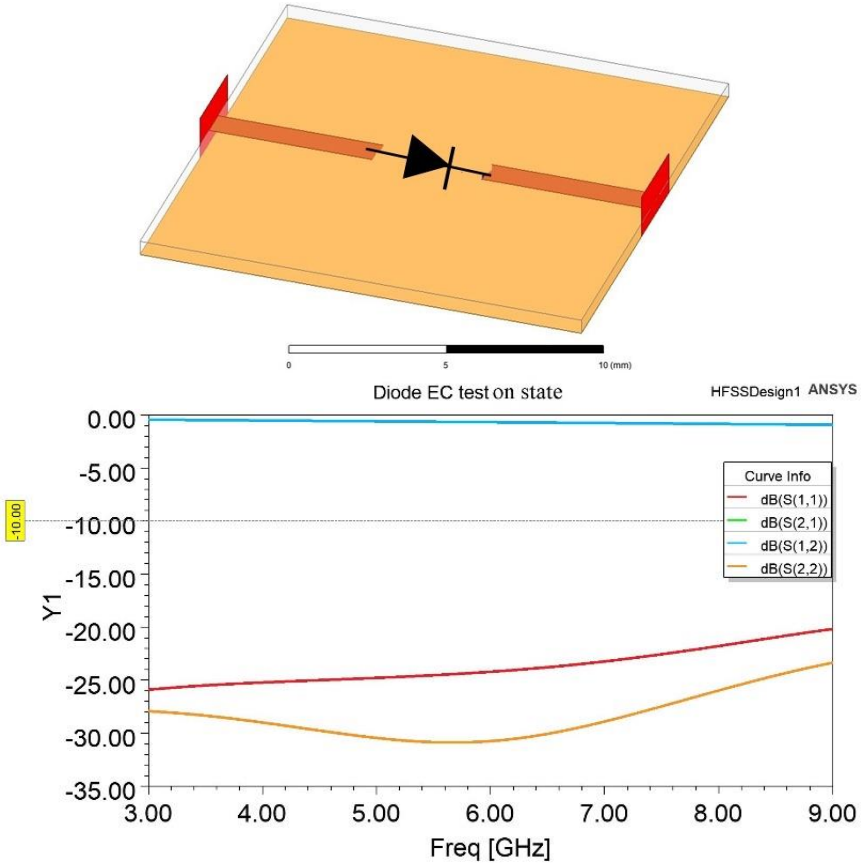

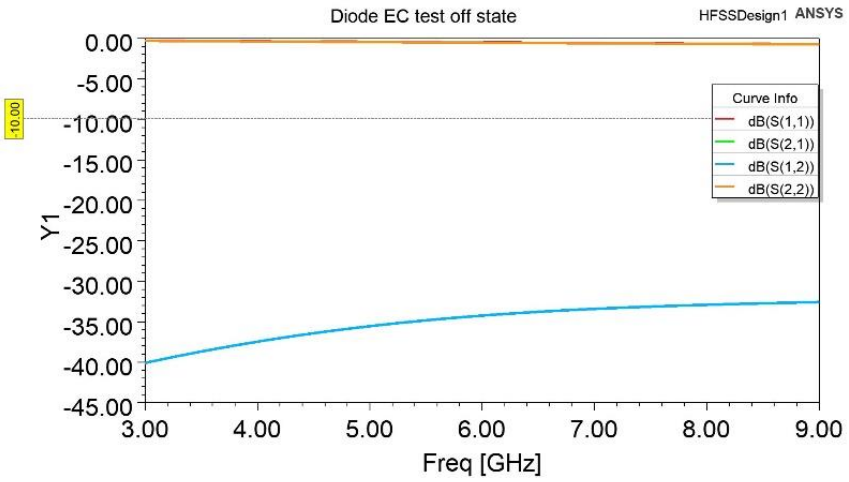

Figure 3-29 The TL tested diode model and S parameter for ON and OFF state from top to bottom.

B- Biasing Circuit

PIN diodes are biased by an inductor, which isolates the bias supply from the transmitter's high-power RF signals. The capacitors ensure that no DC signal reaches the transmitter or receiver. The bias of the diodes is simply altered from forward to reverse to switch ON/OFF. The diodes have a very low resistance when forward biased. As a result, the transmitter will see a direct link between the transmitter and the antenna. When facing the receiver, the quarter wave transmission line converts the short circuit to ground into infinite impedance. **Figure 3-30** below explains the equivalent circuit of the bias circuit witch can be employed by Advance design system ADS software.

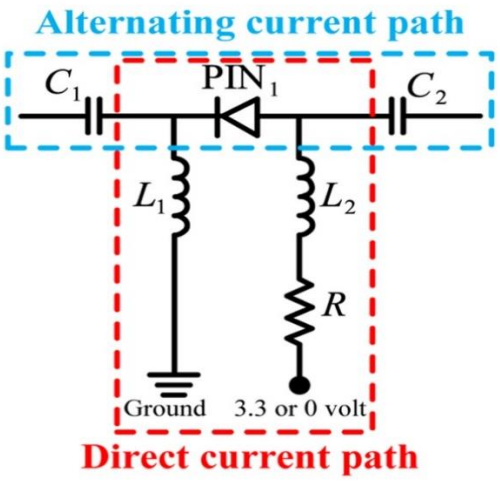

Figure 3-30 Bias equivalent circuit.

This is one of four biasing circuits available. The blue dashed line represents the AC path for the phase-shifting network, while the red dashed line represents the DC path for controlling the working state of the PIN diode. PIN1 is in the ON state when the microcontroller outputs 3.3 volts; otherwise, it is in the OFF state. C1 and C2 capacitances are 150 pF in the simulation to suppress DC power, L1 and L2 inductances are 10 nH to suppress alternating current signal, and R resistance is an adjustable resistance (0–500ohm) to protect DC power and can be modified to optimize the return loss of the proposed antenna.

C- Reconfigurable Antenna Mechanism

Change the bias voltages V1, V2 of the PIN diodes to change the rotation direction. If the bias voltages for arm A depicted in **Figure 3-31**, four PIN diodes, labeled D1, D2, D3, and D4, are soldered between the crossed-dipole arms and feeding patches. To isolate DC current, two chip capacitors are placed into the $3/4\lambda_g$ ring. The suggested polarization reconfigurable antennas PRA can switch between three polarizations by appropriately regulating the ON/OFF states of two pairs of PIN diodes.

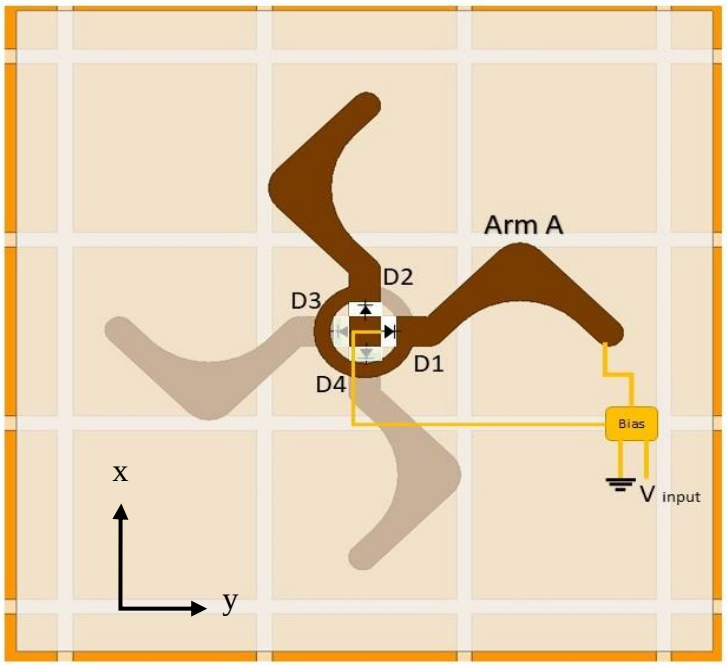

Figure 3-31 Configuration of the reconfigurable antenna VII

When D1 and D3 are turned off, and D2 and D4 are turned on, the RF signal is first transmitted from the feed point to the two arms of the crossed dipole in the y-direction, and then via the 3/4 λ_g Microstrip to the other two arms of the crossed dipole in the x-direction, resulting in a current phase difference. The current phase of the crossed dipole in the x-direction lags by 90° against the y-direction after antenna optimization, resulting in LHCP radiation. When D1 and D3 are turned off and D2 and D4 are turned on, the current phase of the crossing dipole in the x-direction leads by 90 degrees against the y-direction, resulting in RHCP radiation. There is essentially no current phase difference between the two arms of the crossing dipole when all four switches are turned on, resulting in LP radiation. **Table 3-4** lists the three functioning modes and their respective switch states.

Table 3-4 antenna's modes.

Modes	**(D1, D3)**	**(D2, D4)**
LHCP	OFF	ON
RHCP	ON	OFF
LP	ON	ON

D- Reconfigurable Antenna Results

We have proposed three types of the reconfigurable CDA, the flat reflector, cavity reflector and the AMC reflector. Here, we will present the reconfigurable CDA with the AMC reflector, even if the result of this type is not the best because of diodes loss and AMC loss. **Figure 3-32** shows the electric field in RHCP and LHCP states.

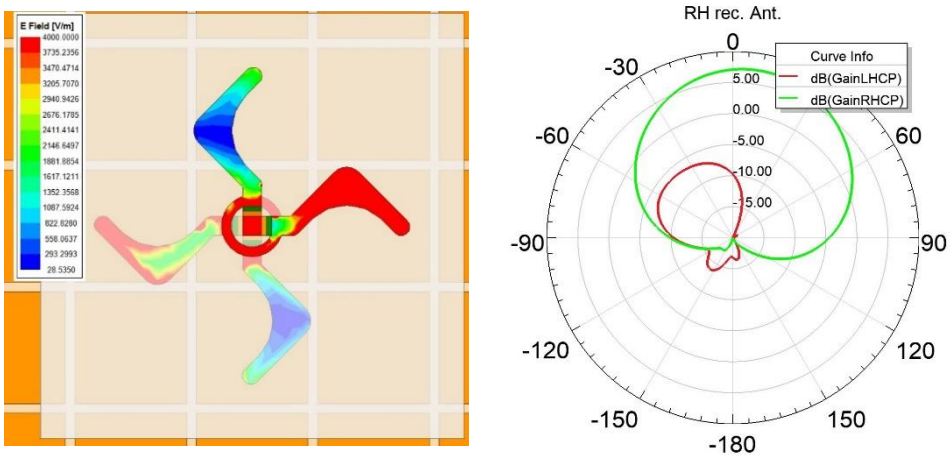

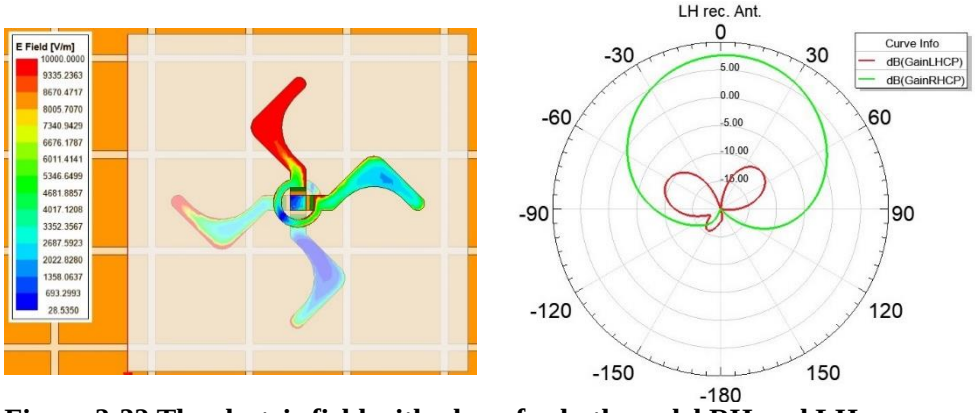

Figure 3-32 The electric field with phase for both model RH and LH.

Here, the electric field with phase on the CDA model for both cases of RH and LH is presented. In the right, the radiation pattern is clear how it changes between the RH and LH polarization through controlling PIN diodes.

The antenna **VII** has -10dB-IBW of 21.63% (5.03-6.25GHz) and the 3dB-ARBW of 8.89% (5.64-6.17GHz). In addition to that, the simulated gain is about 7.4dBi with an efficiency of 93.59%, in which the overall size is about ($0.18 \times 0.18 \times 0.13\lambda_0$).

3.3.4 Parasitic enhancement

A- Antenna Mechanism

Wideband CDAs have recently become available as a result of various modifications to this form, including the addition of parasitic elements [39]-[45]. Here, four quarters are placed among the four arms which give unique results as the increment in the IBW compared to the different shapes of CDAs in [46]-[49]. The antenna **VIII** has the same design with the previous antennas as materials used in the design and dimensions. Modifications in the arm widths are conducted to obtain the enhancements in results of antenna **II** but we will call it sub antenna **II**. Thus, for the cross-strip lines (rectangular) dipole are presented with four quarter parasitic added on the top side of the substrate as depicted in **Figure 3-33** and in **Table 3-5**.

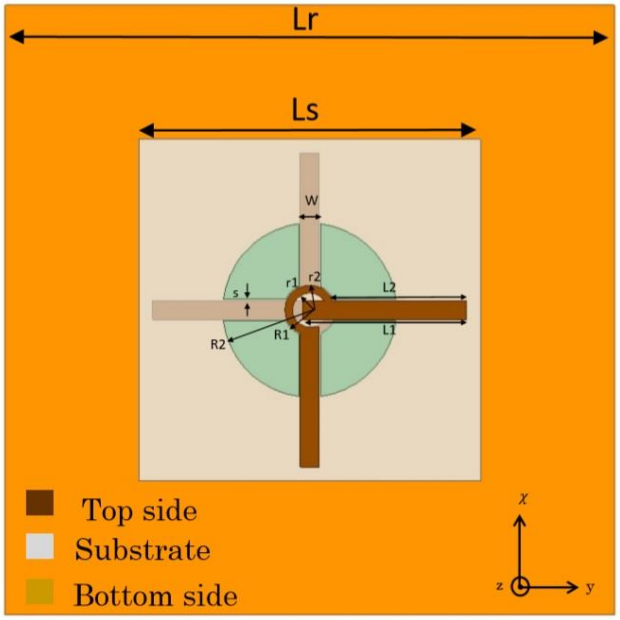
Lr
Ls
W
s
r1
r2
L2
L1
R1
R2
Top side
Substrate
Bottom side
x
z
y

(a)

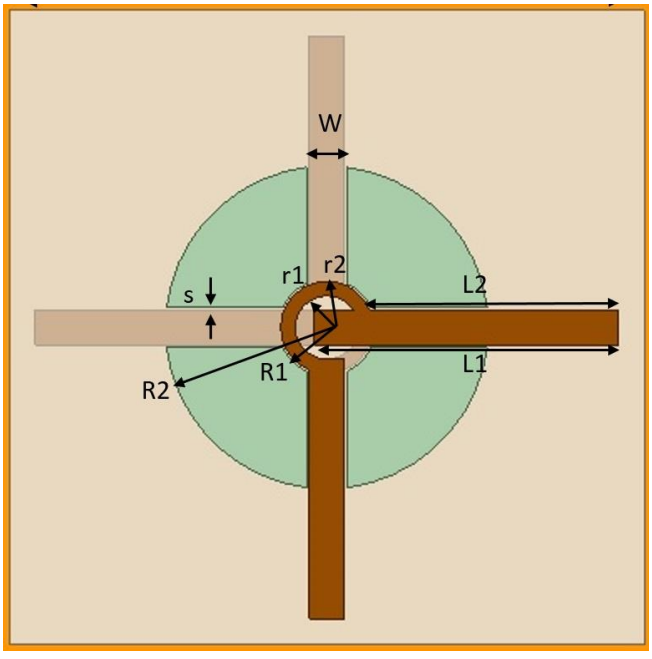
W
s
r1
r2
L2
L1
R1
R2

(b)

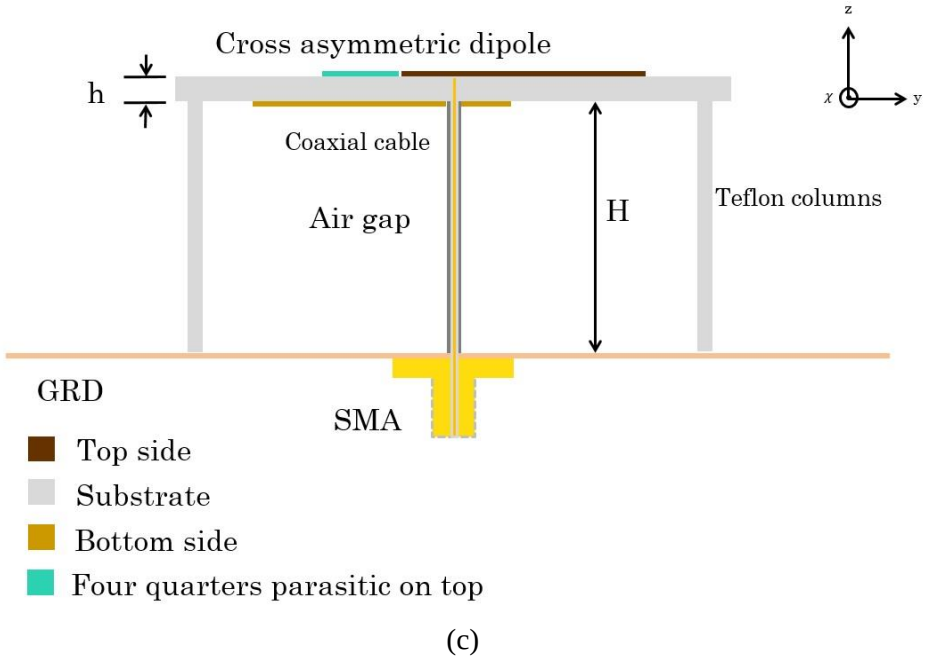

(c)

Figure 3-33 The geometrical antenna VIII (a) top view (b) zoom out arm top view (c) side view.

Table 3-5 Dimensions of the antenna(unit: mm)

Lr	**Ls**	**W**	**S**	**L1**	**L2**
39.25	22	1.2	0.1	9.3	7.3
r1	**r2**	**R1**	**R2**	**h**	**H**
1.1	1.6	1.58	5.6	0.5	12.5

B- Antenna Results

Figure 3-34 presents the comparison between antennas **II** and **VIII**. Since there is only one CP resonance mode, the Antenna **II** has an IBW of 35.11% from 5.26 to 7.5 GHz and a narrow ARBW of 10.67% from 5.59 to 6.22 GHz. The IBW is increased from 35.11% to 88.38% and the ARBW is increased from 11.54% to 55.80% simultaneously, when four quarter parasitic inclusions are added.

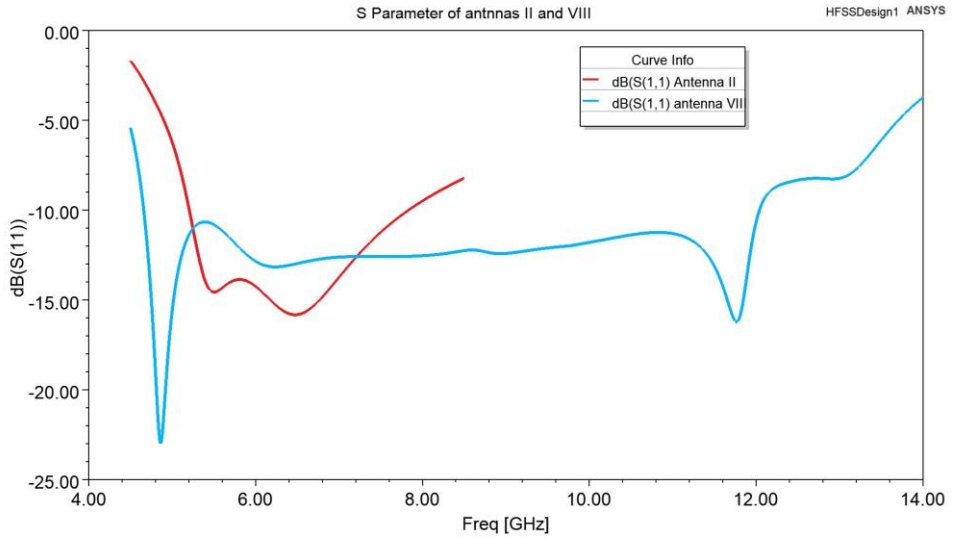

(a)

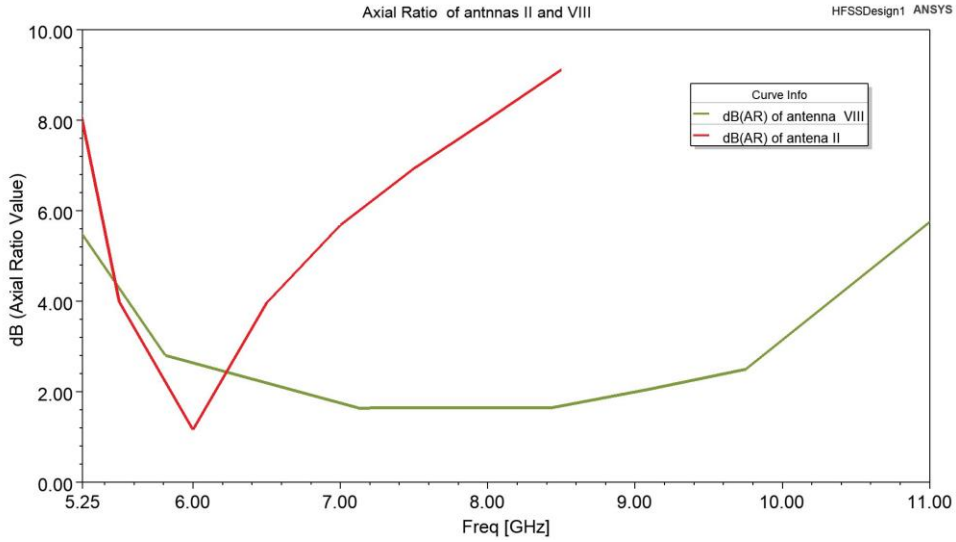

(b)

Figure 3-34 Comparison of output between two antennas II and VIII: (a) RL (b) AR.

The main parameter is changed in R2 with fixed R1 to investigate the effects of the dimension and position of the four quadrants (inner parasitic) dipoles on the output of the proposed antenna to provide good sequentially between the cross dipole arms then getting on wideband -10 dB and 3dB ARBW according **Figure 3-35**.

It is clear the value R2 equal to 5mm is gave best return loss but is not in AR because we need to generate circular polarization so we by optimizing the value of R2 to 5.6mm, and so on, the -10dB IBW 88.38% (4.66-12.04GHz) and the 3dB AR is 55.80% (5.75-10.2 GHz) as well as the four quadrants parasitic resonators and the sequentially rotated configuration as reported in [40], [43], which generate the two minimum points in the IBW and AR curves. In other words, the crossed dipole and four quadrants parasitic with R2-R1 radius, respectively, produce the two deep points of the simulated IBW and AR curves in regions 1 and 2 as seen in **Figure 3-35**. A broadband CP efficiency is achieved in the proposed CP antenna by integrating the two minimum points properly.

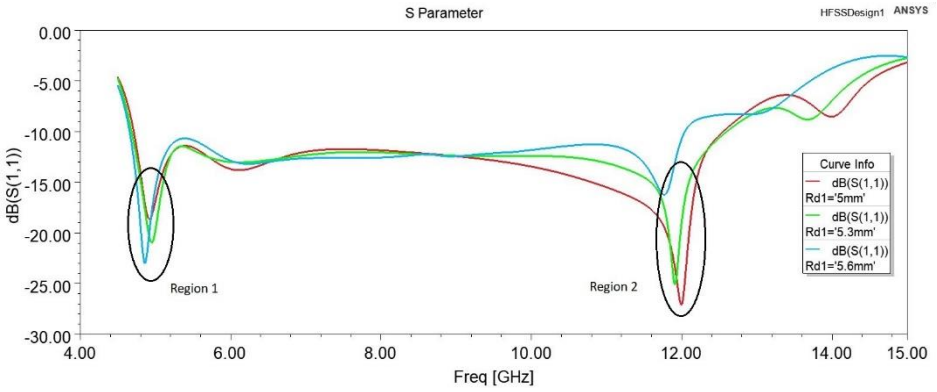

(a)

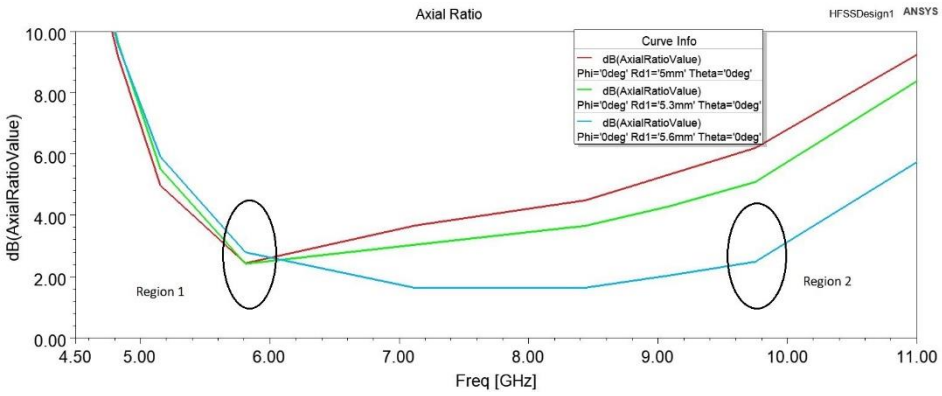

(b)

Figure 3-35 Simulated different value for parameters R2 of antenna VIII: (a) RL (b) AR.

Figure 3-36 depicts the simulated radiation patterns in the xoz- and yoz-planes at 6GHz. In xoz-plane, the patterns are symmetrical to those in yoz-plane. In the boresight direction, the antenna produces unidirectional CP patterns. The RHCP (right-hand circular polarization) is greater than the

LHCP (left-hand circular polarization), resulting in exceptional RHCP radiation.

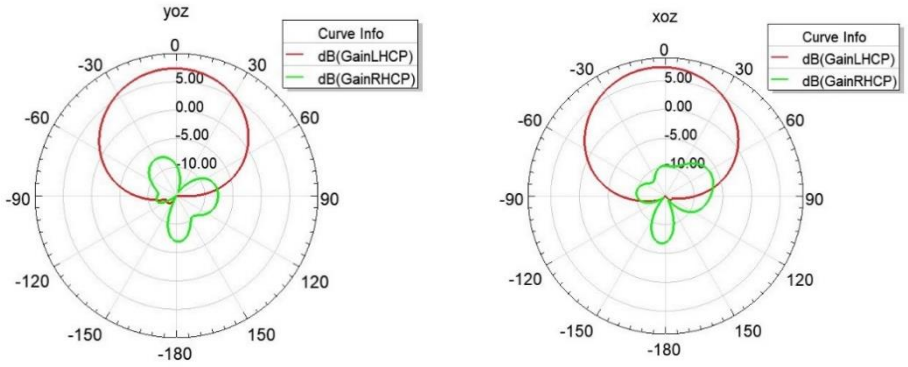

Figure 3-36 Simulated radiation pattern of the proposed CP antenna at 6 GHz.) Antenna VIII.

3.4 Upgrading to the microwave frequencies

5G networks consider the future revolution of the wireless communication systems to introduce better services for the customers. This needs to develop such structures to keep up with the new requirements. Furthermore, to come up with what explained above, using larger bandwidth is necessary, but low frequency bands are crowded. Thus, looking for another frequency bands providing large bandwidth becomes mandatory. The 28-32GHz frequency band is the most candidate one. Here, we have designed a new CDA operating at this frequency band. The CDA of the two families (boomerang& rectangular) are designed and simulated. They will be the first CDAs working at 28GHz in the literature according to the best of authors' knowledge. This belongs to that it is challenge to matching dimensions of the rectangular stubs with short length of VQR witch they will be approximately 1.75mm as shown in **Figure 3-37.** Thus, it will be a challenge, but we have exceeded the dilemma with accurate design and unique results as explained in next subsection.

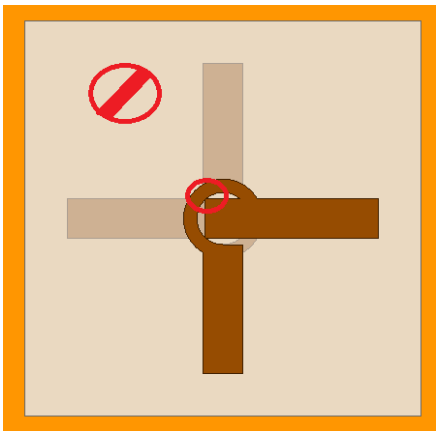

Figure 3-37 failure CDA at 28GHz.

3.4.1 28 GHz CDA

No researchers have previously worked on this design. Here, we have more than distinguished results for both families (boomerang & rectangular) as follows:

A- The 28 GHz Rectangular Shape

The antenna has designed at 28GHz at $\boldsymbol{\lambda_o = 10.7\ mm}$. It is made up of two orthogonally aligned straight dipoles, referring to the subsection (3.1.2). The arms of the dipole are printed on two sides of the FR4 substrate with a thickness of 0.25 mm (($\boldsymbol{\varepsilon_r}$) = 4.4, tan = 0.02) and immediately connected by the semi-rigid coaxial cable of 50Ω which allows to have a $\mathbf{180}^{\circ}$ phase difference between the two arms of each dipole. Referring to subsection (0), the coaxial cable characteristic impedance $\boldsymbol{Z_o}$ as shown in **Figure 3-3** is calculated by Equations (2-20, 2-21, 2-22 and 2-23). The material used in calculations is the Polyflon CuFlon (tm) of permittivity 2.1 and loss tangent of 0.00045 with a radius of 0.16mm. A radius of the inner conductor is 0.045mm and a radius of the outer conductor is 0.18mm to get$Z_o = 50\Omega$. Furthermore, the Cutoff Frequency is 318GHz, while the equivalent capacitance and inductance are 29pF/ft and 74.7nH/ft, respectively. The antenna dimension is depicted in **Figure 3-38** and dimensions are provided in the **Table 3-6** as below:

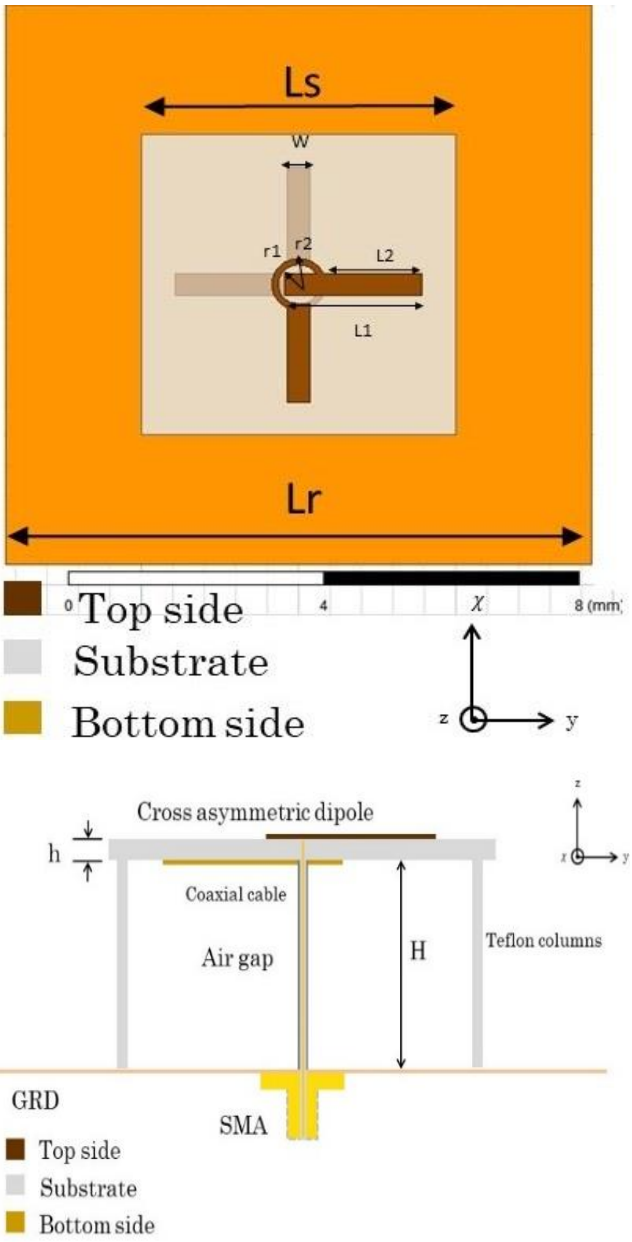

Figure 3-38 The proposed antenna IX (a) top view (b) side view.

The results shows IBW of 53.02% from 19.92 to 34.29 GHz and a ARBW of 19.33% from 26.43 to 32.11 GHz the gain 7.5 dB and the directivity is

Table 3-6 A summary of the antenna dimensions antenna IX (unit: mm)

Lr	**Ls**	**W**	**r1**
9.31	5	0.36	0.33
L1	**L2**	**H**	**r2**
2.185	1.56	2.675	0.43

7.5 dB with efficiency was very high **Figure 3-39.**

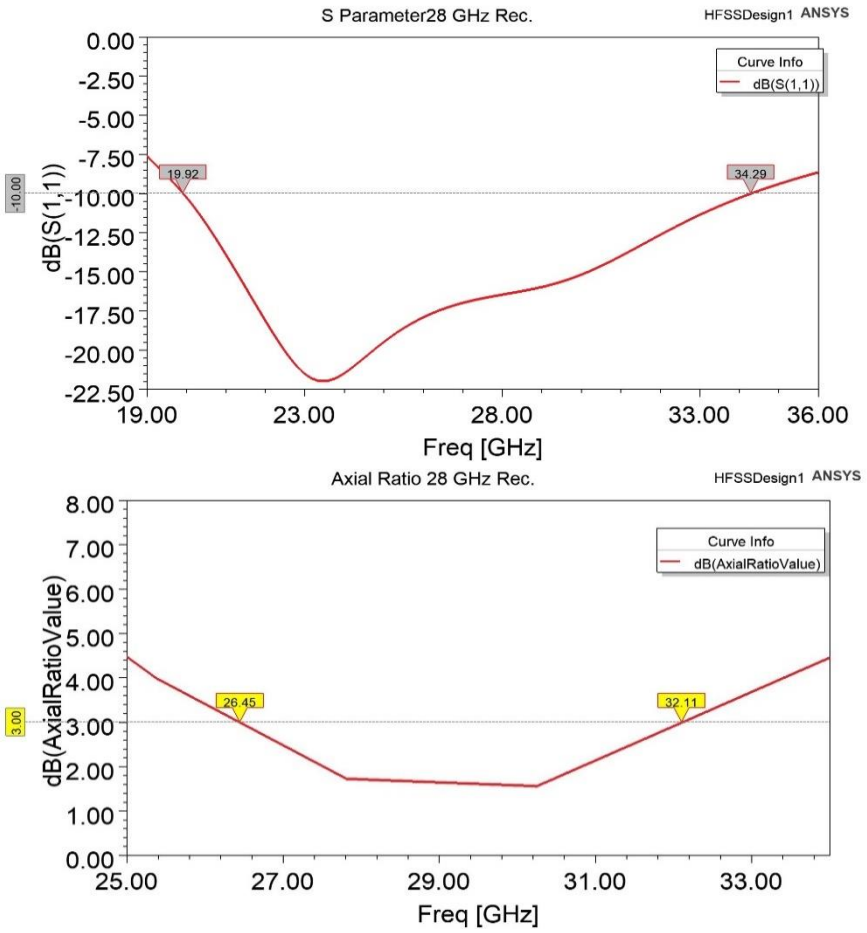

Figure 3-39 Simulated results of the antenna IX (top) RL (bottom) AR

Figure 3-40 (a) & (b) shows the simulated radiation patterns at 28 GHz antenna **IX** in xoz-plane and yoz-planes.The patterns in xoz-plane are symmetrical to those in yoz-plane. The antenna generates unidirectional CP patterns in a boresight direction. The right-hand circular polarization (RHCP) is higher than the left-hand circular polarization (LHCP) by 27.5 dB, generating exceptional RHCP radiation.

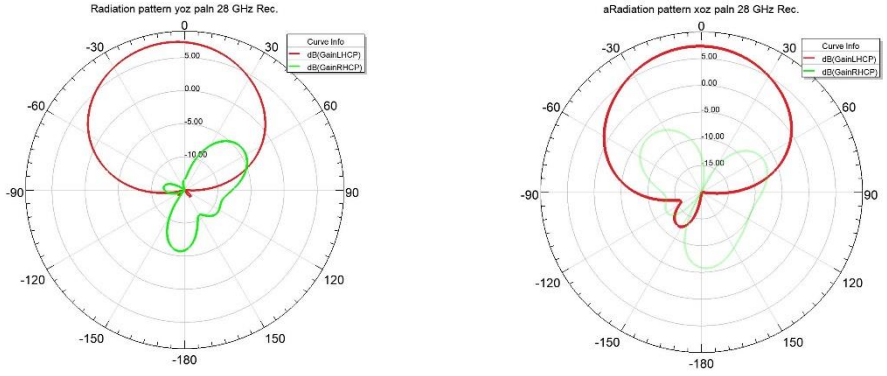

(a) (b)

Figure 3-40 Simulated radiation pattern of the proposed CP antenna at 28 GHz Antenna IX a) yoz plane b) xoz plane.

B- The 28GHz Boomerang shape

As depicted in **Figure 3-41**, the antenna **X** is a pair of boomerang arms connected together by the feeding network as driven elements. All others parameters and dimensions of the design are same for the antenna **IX** except the arms. Therefore, in **Table 3-7,** it is a list of dimensions.

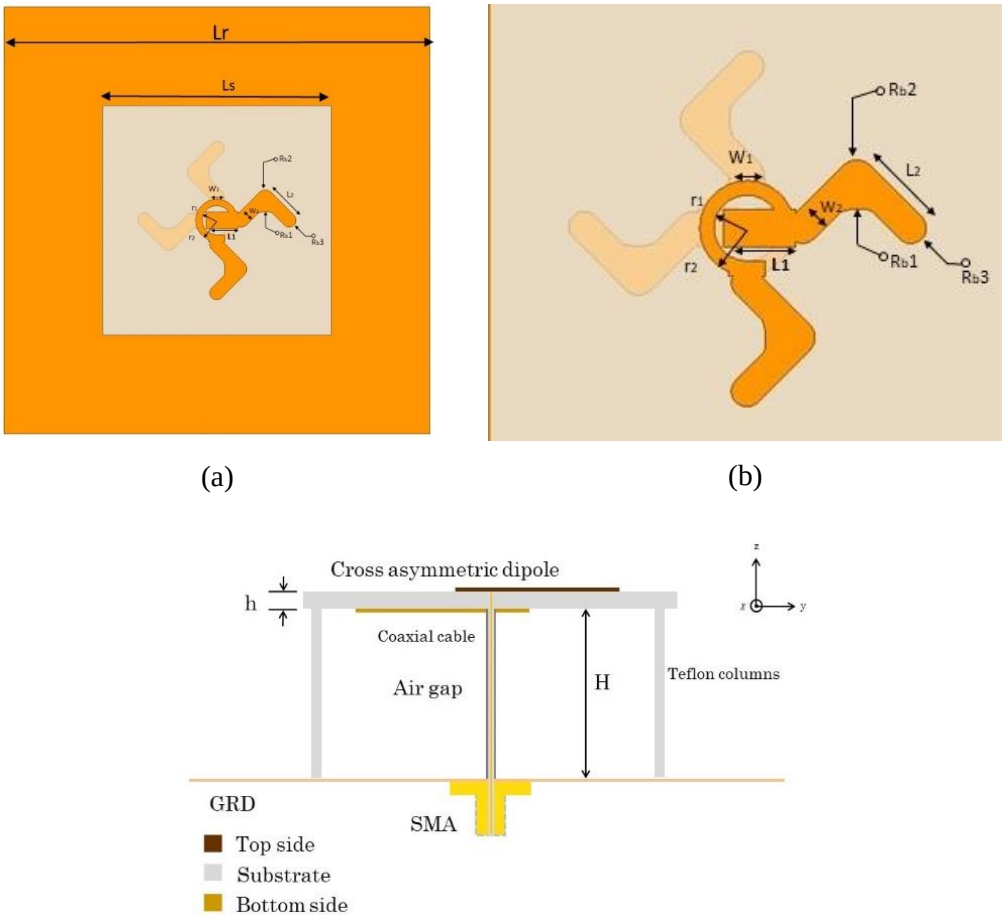

Figure 3-41 The proposed antenna X (a) top view (b) zoom out top view (c) side view.

Table 3-7 A summary of the antenna dimensions X (unit: mm).

Lr	**Ls**	**W1**	**W2**	**L1**	**L2**
9.3	5	0.36	0.3	0.695	0.71
r1	**r2**	**Rb1**	**Rb2**	**Rb3**	**H**
0.33	0.43	0.5	0.18	0.15	2.675

The results shows IBW of 46.40% from 21.35 to 34.25 GHz and a ARBW of 16.47% from 28.13 to 33.18 GHz. The gain is 7.5 dB and the directivity is 7.6 dB with efficiency of 98.68% as shown in **Figure 3-42.**

Figure 3-43 (a) and (b) shows the simulated radiation patterns at 28GHz for the antenna **X** in the xoz and yoz-planes.The patterns in xoz-plane are

symmetrical to those in yoz-plane. The antenna generates unidirectional CP patterns in the boresight direction. The right-hand circular polarization (RHCP) is higher than the left-hand circular polarization (LHCP) by 17.25 dB, generating exceptional RHCP radiation.

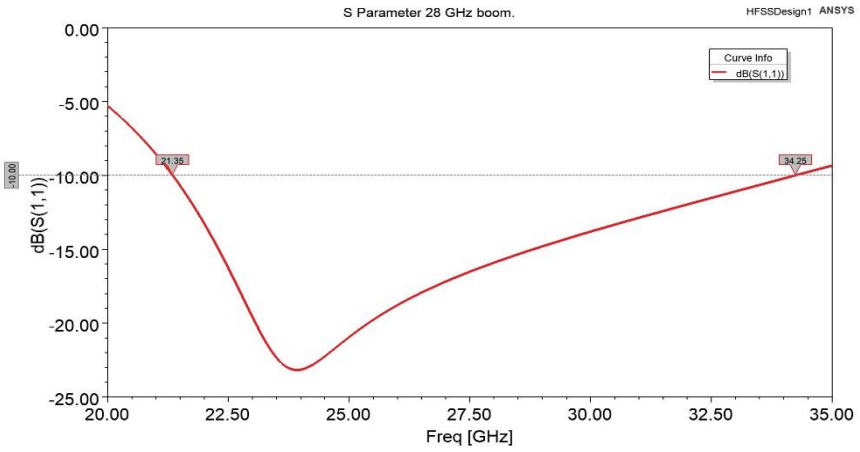

(a)

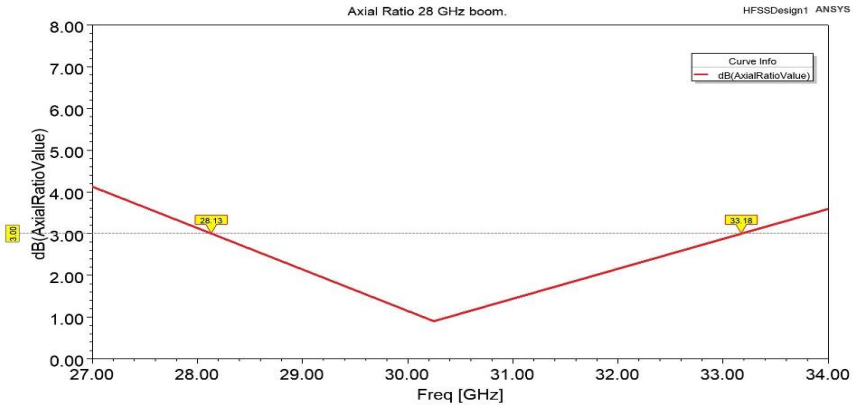

(b)

Figure 3-42 Simulated results of the antenna X (a) RL (b) AR.

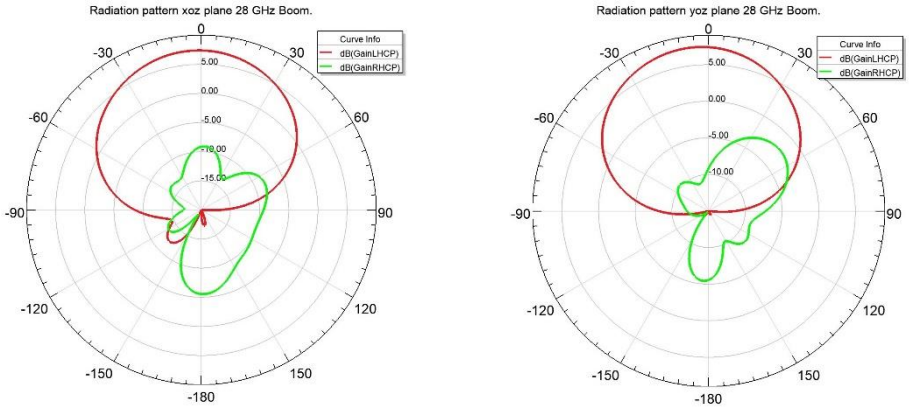

(a) (b)

Figure 3-43 Simulated radiation pattern of the proposed CP antenna at 28

GHz Antenna X (a) yoz plane (b) xoz plane.

3.5 Brief for the Proposed and presented CDAs

3.5.1 Summary the Proposed Antennas

The evolution of all proposed antennas presented here is demonstrated precedingly to show up the mechanism for improving bandwidths. The enhancements and modifications are divided into four parts of new shapes using the cavity, AMC and each one of them is designed to be reconfigurable antennas.The cavity is used to stop or at least to highly mitigate the backward radiation, especially a cavity with side walls. Therefore, we fabricate this structure because it offers the best results, but it is bulky. After that, the development is presented from the sub-5G spectrum frequency to 28GHz 5G spectrum frequencies. Also, the two families that we have discussed about them are presented with excellent results for both as shown in **Table 3-8**, **Table 3-9** and **Table 3-10** as shown below:

Table 3-8 List of the proposed antennas.

Ant. No.	NO	Design Name	Shape arms	Polarization type
I	Ant.1	Cross dipole-printed antenna (Strip line) circular edge	Strip line	LHCP
II	Ant.2	Cross dipole-printed antenna (Strip line) square edge	Strip line	LHCP
III	Ant.3	Cross dipole-printed antenna (Boomerang shape) square edge	Boomerang	RHCP
IV	Ant.4	Cross dipole-printed antenna (Strip line) square edge with cavity	Strip line	RHCP
V	Ant.5	Cross dipole-printed antenna (Boomerang shape) square edge with cavity	Boomerang	RHCP

VI	Ant.6	Cross dipole-printed antenna (Boomerang shape) square edge with AMC	Boomerang	RHCP
VII	Ant.7	Cross dipole-printed antenna (Boomerang shape) square edge with AMC and diodes	Boomerang	RHCP & LHCP
VIII	Ant.8	Cross dipole-printed antenna (Strip line) square edge with parasitic element	Strip line	RHCP
IX	Ant.9	Cross dipole-printed antenna (Strip line) square edge 28GHZ	Strip line	RHCP
X	Ant.10	Cross dipole-printed antenna (Boomerang) square edge 28GHZ	Boomerang	RHCP

Table 3-9 The results list of the proposed antennas part1.

Ant. No.	**,-10 db rang GHz**		**3db-AR rang GHz**		**Center frequency GHz**	**Ratio BW GHz**
	f_L	f_H	f_L	f_H		
I	5.34	7.39	5.78	6.66	6.365	1.38
II	5.26	7.5	5.59	6.22	6.38	1.43
III	5.1	7.85	5.85	6.32	6.475	1.54
IV	5.28	8.11	5.73	6.37	6.695	1.54
V	5.08	8.5	5.72	7.46	6.79	1.67
VI	5.36	7.89	5.79	6.74	6.625	1.47
VII	5.03	6.25	5.64	6.17	5.64	1.24
VIII	4.66	12.04	5.75	10.2	8.35	2.58
IX	19.92	34.29	26.45	32.11	27.105	1.72
X	21.35	34.25	28.13	33.18	27.8	1.60

Table 3-10 The results list of the proposed antennas part2.

Ant. No.	,-10 db IBW %	3 db-AR BW %	Gain db	Directivity db	Efficiency	Size of design λ_o
I	32.21%	14.15%	7.4	7.6	97.37%	0.78*0.78*0.27
II	35.11%	10.67%	7.4	7.6	97.37%	0.78*0.78*0.27
III	42.47%	7.72%	7.4	7.6	97.37%	0.78*0.78*0.27
IV	42.27%	10.58%	8.4	8.6	97.67%	0.78*0.78*0.27
V	50.37%	26.40%	8.3	8.5	97.65%	0.78*0.78*0.27
VI	38.19%	15.16%	7.7	7.9	97.47%	0.78*0.78*0.27
VII	21.63%	8.98%	7.3	7.8	93.59%	0.78*0.78*0.27
VIII	88.38%	55.80%	7.5	7.7	97.40%	0.78*0.78*0.27
IX	53.02%	19.33%	7.5	7.5	99%	0.88*0.88*0.24
X	46.40%	16.47%	7.5	7.6	98.68%	0.88*0.88*0.24

3.5.2 Comparison between the proposed and presented CDAs

In the next section, we will choose one antenna to be used in the proposed antenna array to generate then the OAM EM waves. Even if the side-wall cavity antenna offers the best results. The antenna **IX** and **X** will be chosen for the 28GHz 5G spectrum frequencies because they have good return loss compared to ones in [37]-[40]. The antenna **X** with boomerang arm shapes is a good alternative to other arm shapes like bowtie CDA which have a wide impedance bandwidth as known compared to other shapes of the CDA [41]-[46], see **Table 3-11** that summarizes the comparison between the proposed antennas with previous works in the literature.

Table 3-11 A comparison between the proposed chosen antenna with the previous works

Ref. Antenna	Size (λ0)	Antenna's Structure	-10 dB IBW GHz	3-dB ARBW GHz	Max Gain (dBi)
[37]	1.05x1.05x0.24	Crossed dipole +Parasitic Loop Resonators	0.93	0.75	8
[38]	1.1 ×1.1×0.28	Crossed dipole + Cross loop + Squared cavity reflector	3.2	2.79	8
[39]	1.04×1.04×0.26	Crossed dipole + Parasitic elements+ Conventional reflector	1.35	1.23	7.2
[40]	1.04x1.04x0.26	Crossed dipole + Parasitic elements+ Conventional reflector	1.68	1.7	6.8
[41]	0.57 ×0.57 ×0.24	Crossed dipole + Dual squared cavity reflector	2.8	2.5	8.5
[42]	0.65 ×0.65 ×0.16	Crossed dipole + Parasitic elements+ Squared cavity reflector	1.07	0.43	7.8
[43]	1.17 ×1.17 ×0.29	Crossed dipole + Parasitic elements	1.85	1.6	8.6
[45]	0.88 ×0.88 ×0.23	Crossed dipole + Squared cavity reflector	1.42	1.4	9.6
[46]	1.1×1.1 ×0.4	Crossed dipole + bowtie dipole loaded with three of four sitparasitic	3.82	4.07	8.6
Proposed IX	0.88 ×0.88 ×0.24	Crossed dipole strip line arms	14.37	5.66	7.5
Proposed X	0.88 ×0.88 ×0.24	Crossed dipole boomerang arms	12.9	5.03	7.5

Chapter 4: Antenna array OAM electromagnetic wave

4.1 Antenna array (normal uniform circular array)

A circular array is an array layout in which the components are arranged in a circle form. It is really useful because of its ability to scan its beam pattern in two directions in space in contrast to the linear array which can vary its beam pattern only in one direction. Thus, this type of arrays finds itself in a bunch of applications such as radio direction finding, air and space navigation. Navigation, subterranean propagation, radar, sonar, and a variety of other technologies are only a few of the systems available. Circular that is a newer term to be used in wireless communication, in particular smart antennas, has been proposed in [17], [18]. Looking for other new types of arrays that support different types of communication techniques is a hot research topic nowadays owing to increasing the communication system capacity.

To make any type of the antenna arrays very versatile, the antenna array should be fed with smart feeding. Another term that makes the array more sophisticated is the antenna element used in that array when having high performance with a simple structure. The antenna **IX**, designed in the previous chapter, will be the candidate to do the task, due to the simplicity of its structure, the ease to optimize and the operation at 28GHz. Undoubtedly, the CDA is a high profile structure, referring to the subsection (3.3.2), so the AMC technique will be presented here in the same manner as in the AMC reflector design introduced in subsection (3.3.2) for the CDA operating at 6GHz to design and simulate our proposed OAM antenna arrays.

In general, the proposed antenna arrays consist of several layers with different kinds of microwave components as following:

- Array of single elements CDAs.
- Array substrate.
- AMC structure (N×N unit cells).
- AMC substrate.
- Transmission feeding lines.

- TL substrate.
- Smart feeding network.
- Feeding network substrate (it can be merge the feeding network and TL in one level layer).
- In additionally the accessories, coaxial cable and perfect electric PE (reflectors & via).

All these components above-mentioned are integrated to form the OAM antenna array design with taking into account influences of the grounding system.

4.2 Enhancement the upgraded CDA

According to our demonstrations in subsection (3.3.2), the problem statements, and our motivations in Chapter one (1.5) and (1.4), respectively, the 28 GHz- CDA is adopted to eliminate the need for the conventional reflectors with height of a quarter wavelength as a requirement to have constructive interference between the signals coming from the main radiator and the signals bouncing back from the reflector. This occurs because the signal path from the radiator to reflector is equal almost to half wavelength which is electrically equal to 180degree phase shift. The reflection from the ground will add another 180degree phase shift. Totally, the phase difference will be 360degree which is equal to 0degree phase shift. So, if we have a reflector with 0degree phase shift, the quarter wavelength distance will not be needed at all. Thus, the space will be diminished, resulting in low profile structure.

4.2.1 The AMC Unit Cells and the Structure Design of 28-GHz CDA

In the same design manner introduced in subsection (3.3.2), the AMC unit cell, operating at 28GHz, can be modeled as an identical parallel LC resonator with a resonant frequency of $f = 1/2\pi\sqrt{LC}$, where C and L represent equivalent capacitance and inductance, respectively. The range of acceptable phases offered by the AMC is from –90° to 90° [27]. A complete numerical analysis of the AMC cell has been conducted by simulation software HFSS **Floquet Ports. Figure 4-1** shows the model and the master

and slave of Floquet technique. As can be seen, this phase range can cover a wideband range of frequencies.

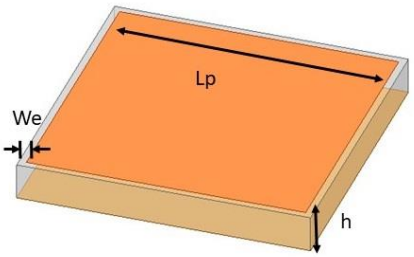

(a)

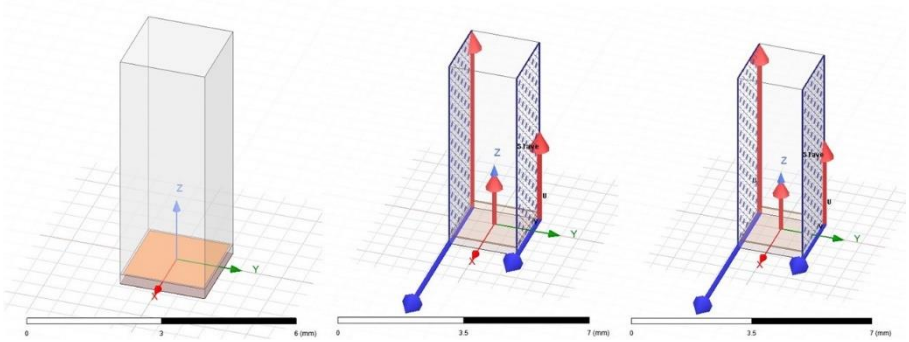

(b)

Figure 4-1 The AMC 28 GHz unit cell model (a) dimensions parameters (b) Floquet port technique.

Here, after doing parametric study for the parameter Lp, it has been found that performance of the convenient unit cell width to the whole unit cells AMC structure which is demonstrated in **Figure 4-2**, the reflection phase of the AMC structure. For further analyses, someone can change substrate type, thickness, and the patch shape to see their impacts on the phase shifts.

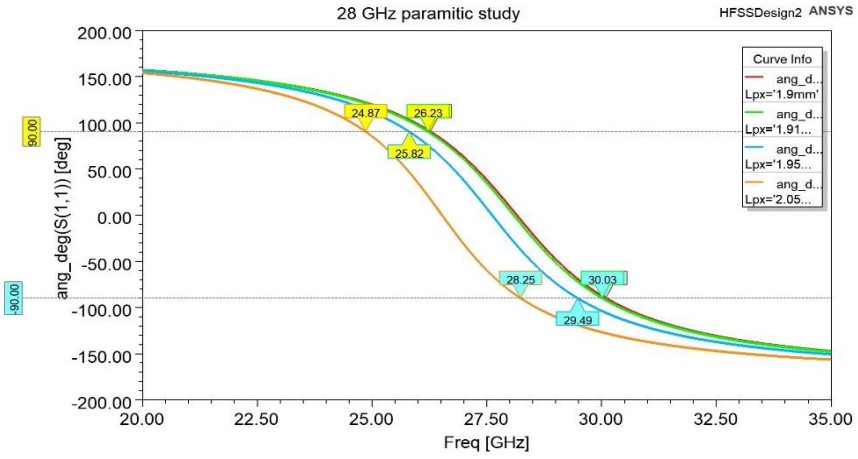

(a)

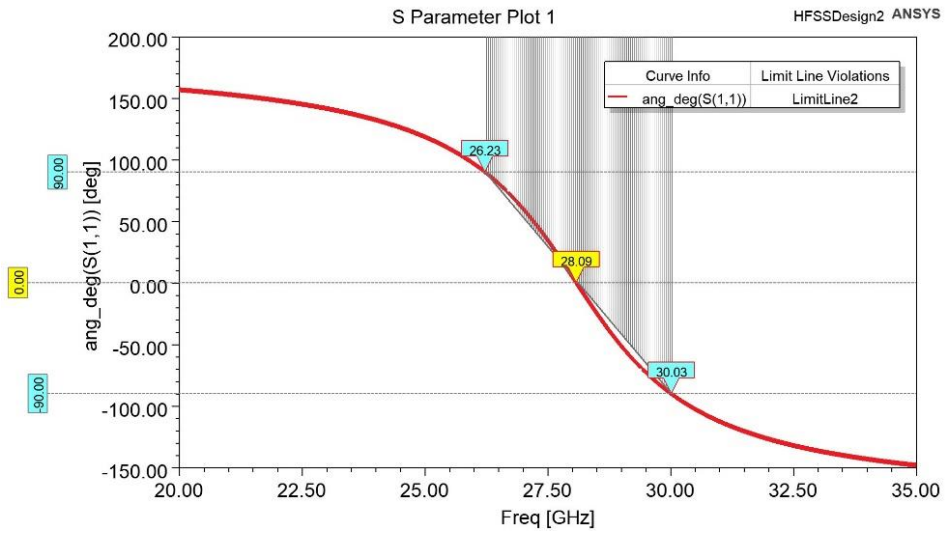

(b)

Figure 4-2 S parameter (a) Lp parameter dimension of AMC unit cell (b) phase reflection of Lp=1.91 mm.

The AMC surface consists of 6×6 unit-cells, printed on the top side of the lower dielectric substrate, with a thickness of 0.25 mm where the martial type is FR-4 (tm) ($\varepsilon r = 4.4$ and $\tan\delta = 0.02$). Each unit-cell has a side length of Lp=1.91mm about $0.17\lambda_0$, the spacing between the cells is Ws= 0.2 mm and the edge spacing is We= 0.2 mm. Then, the overall reflector size is 12.76×12.76 mm^2.

The AMC reflector is placed with a height of H_{AMC}=0.05 mm, where this number comes when optimizing a height of the radiation element within AMC array, see **Figure 4-3**. It is very low profile antenna where the separating distance is about $0.00046\lambda_0$ less by 88% than the antenna **IX** in the vertical dimension. This is one of the aims motivated us to use the AMC surfaces (i.e., to make a low profile microstrip antenna) [27]. **Figure 4-4** shows performance of the antenna **IX** 28GHz with AMC reflector for three different values of the antenna substrate high the parameter h. The substrate thickness high is fixed by 0.25 mm but has been manipulating by the air gap between the substrate to AMC reflector. the parameter h is equal to 0.3 mm is mean that the air gap equal to 0.05 mm in addition to the substrate's thickness

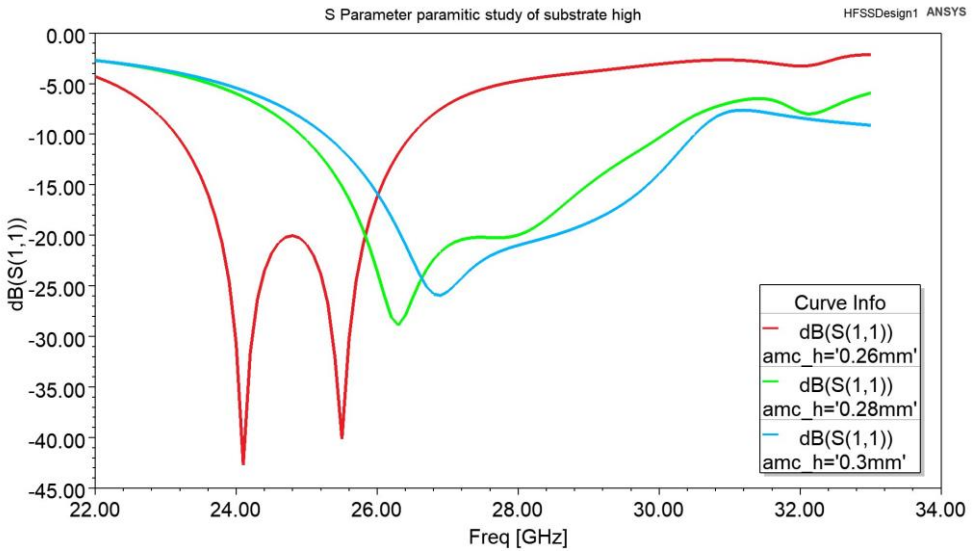

Figure 4-3 RL for different high substrate.

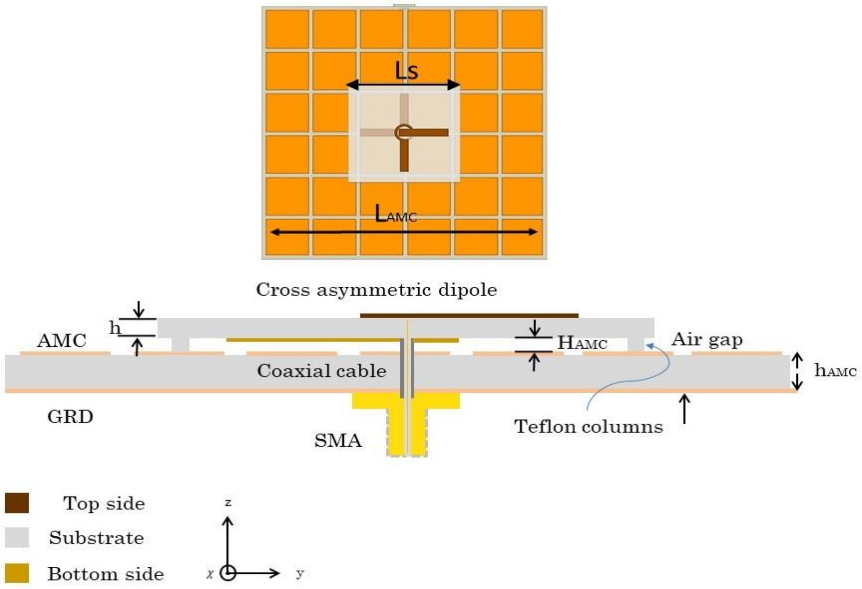

Figure 4-4 28GHz CDA with AMC structure top view and side view.

4.2.2 Result and comparison

The -10-dB IBW obtained from 25.25 GHz to 30.51 GHz is equal to 5.26 GHz bandwidth, the 3dB ARBW is from 27.11 GHz to 28.98 GHz, and the gain is 7.9 dB with an efficiency of 90.8%. Obviously, when we compare the same antenna **IX** without the AMC substrate, the former one has limited bandwidth. However, it has very small vertical dimensions which consider the promising solutions for many applications. In addition, the obtained gain is bigger by 0.5 dB with slight reduction in the efficiency owing to the extra losses added by the AMC layer. **Figure 4-5** shows the antenna **IX** results**.**

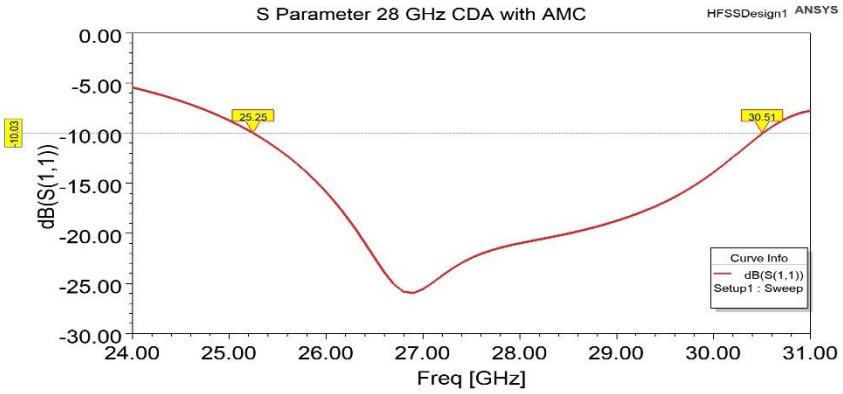

(a)

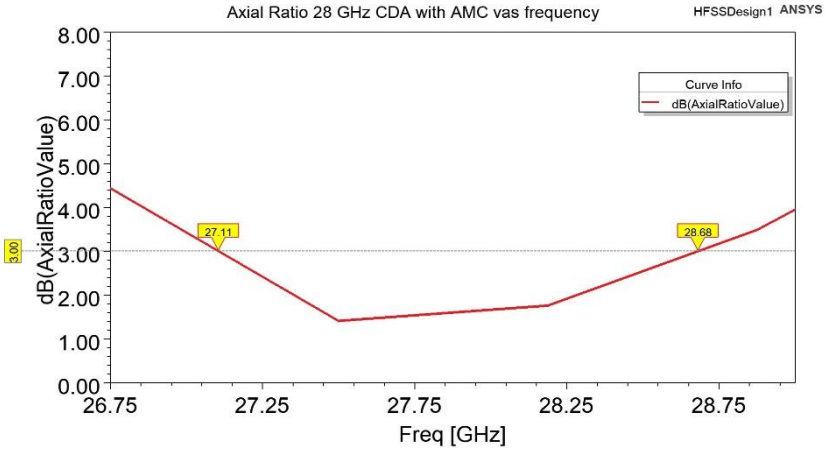

(b)

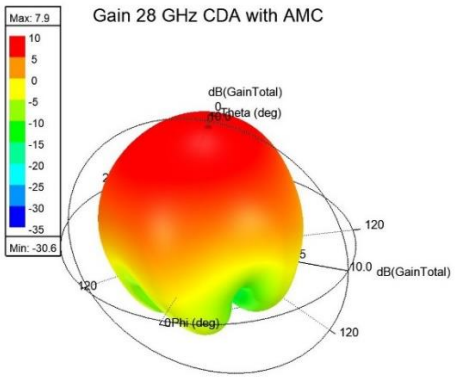

(c)

Figure 4-5: Results of 28GHz CDA with AMC (a) RL b) AR c) 3D gain plot.

Figure 4-6, shows the simulated radiation patterns at 28 GHz in the xoz and yoz-planes. Although the two patterns point to the same direction (i.e., the boresight direction), they are not identical. The antenna generates unidirectional CP patterns in the boresight direction. The left-handed circular polarization (LHCP, i.e., Co-polarization component) is higher than the right-handed circular polarization (RHCP, i.e., Cross-polarization component), generating the exceptional LHCP radiation.

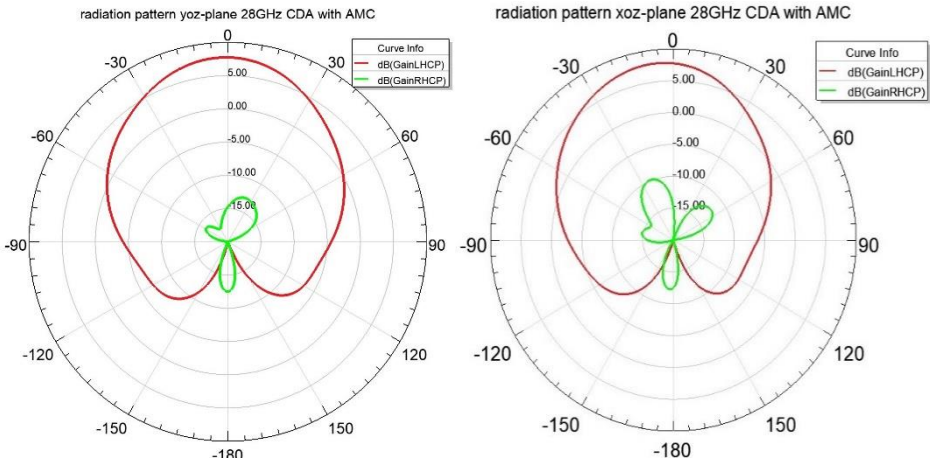

Figure 4-6 Simulated radiation patterns in the yoz and xoz planes of the proposed CP 28GHz CDA type IX with the AMC reflector.

4.2.3 Transmission Line Connected to the 28-Ghz CDA with AMC Reflector

To accommodate a feeding network in the array without noticeably increasing the overall size, it is preferred to feed the antenna from the bottom. In other words, a third layer underneath the AMC layer will be added to route traces of the feeding network. It is made of the microstrip transmission line type. Referring to the subsection (2.3.4) in chapter of theoretical background, 50-ohm microstrip transmission line width of 0.465mm is used and calculated by Equations (2-6 and 2-7).

To check and validate the feeding transmission line that can transfer the power from the SMA connector to the antenna without any problem, we use the same type of substrates in the third layer as in the AMC layer. This assumption will ease the feeding procedure for now. In the subsequent section, different type of the substrates will be utilized. Therefore, in this test, we have used the dielectric substrate FR-4 (tm) ($\varepsilon r = 4.4$ and $\tan\delta = 0.02$), with a thickness of 0.25 mm. **Figure 4-7** presents the test structure model with all important notations.

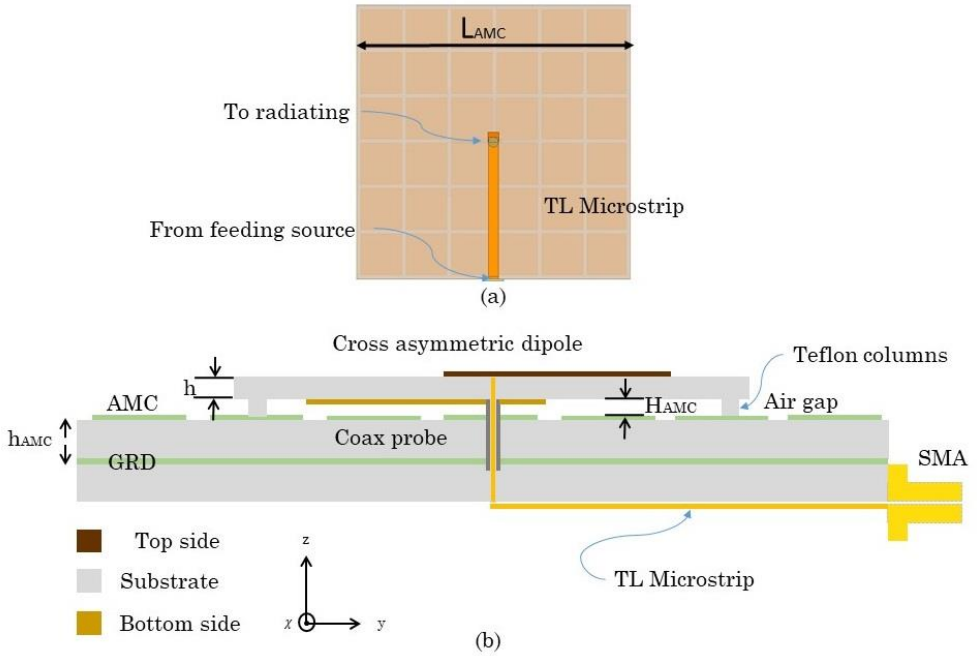

Figure 4-7 28GHz CDA with AMC structure and microstrip feeding TL (a) bottom view (b) side view.

The results indicate that there is a reduction in the performance due to using the lossy transmission line type (FR4) and via connection that transfers the power from the lower feeding line to the coaxial probe of the main antenna, but the results are still very good. This test step is very important in our research to have a smoother transition from the single element design into the whole array design. Grounding the AMC structure, coax probe, microstrip line, and the outer conductor of the coax probe is obtained by connecting them to the bottoms arms of the radiating elements. Thus, any short, for example, in the AMC cell or disconnecting the outer coax probe to reflector ground (see **Figure 4-7**) will collapse the integrity of antenna!!! The S11 -10-IBW (25.68-31.08 GHz) may look the same or little bit greater than the antenna without the feeding TL, even the AR 3-dB (26.43-28.38 GHz), but we mentioned earlier that there is a drop-down in the gain. It becomes 7.1dB with efficiency more than 83.5% compared to results shown in **Figure** 4-7. However, the antenna maintains on the same radiation patterns for the two planes yoz and xoz, but with bigger cross polarization than the previous antenna. **Figure 4-8** depicts the results.

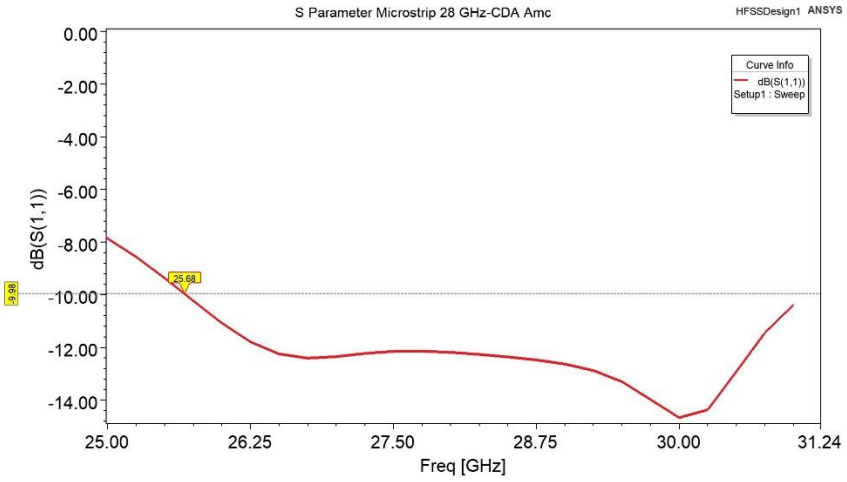

(a)

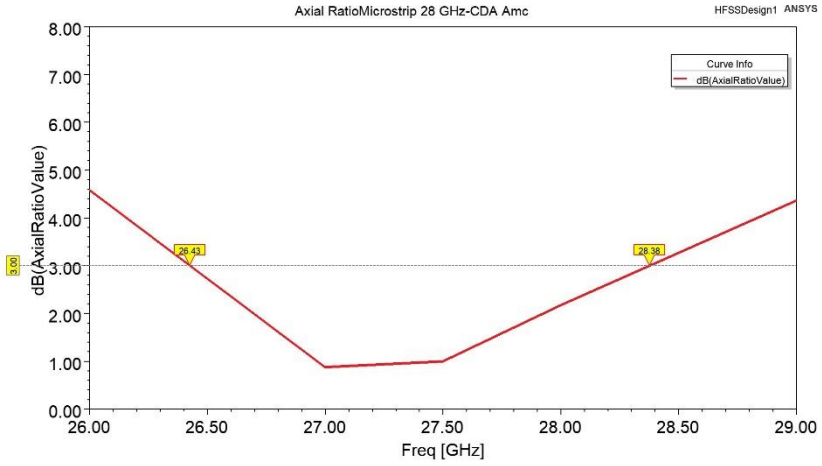

(b)

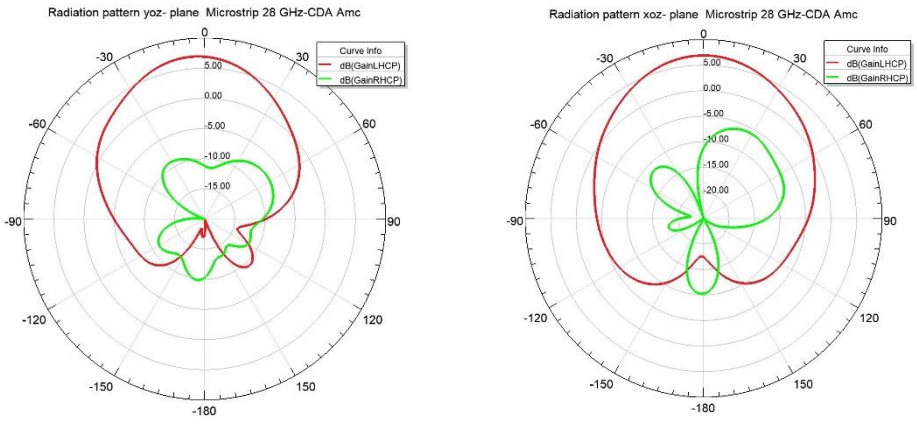

(c) (d)

Figure 4-8 The 28GHz CDA with AMC and microstrip feeding TL (a) RL (b) AR (c) and (d) radiation patterns in the yoz and xoz-planes.

4.3 OAM Antenna Array

The orbital angular momentum OAM term was common in the optics discipline for decades, but in microwave it appears recently with no more research efforts. This phenomenon can support the spatial multiplexing which is very useful in communication to increase the channel capacity without the change in time and frequency. Also, if the spatial property is used with the time and frequency, the benefit will be threefold. There are different approaches to make the antenna array operating with OAM radiation properties. In Chapter 1, most approaches are mentioned. For the sake of simplicity, one approach will be recalled here which is the vertical space (i.e., elevation). The vertical space was an option to be used in[17] to explain an innovative approach of introducing the phase delay. The antennas elements of an array are uniformly distributed along a circumference of the circle but with different elevations. However, the resulting OAM array will be a high profile structure and will not be compatible with our thesis aims. In this thesis, the feeding network will be responsible for providing the phase delay among elements. This makes the array elements radiating the electromagnetic signals with different times. In other words, the transmission phase delay will be obtained. Here, 4, 8 and 9-element uniform circular array UCA are proposed with different of feeding methods.

4.3.1 UCA N-elements

Referring to subsection (2.3.3), the procedure followed to achieve the OAM array mainly depends on the radius and a distance of the antenna element location from the circle center. If the right phase distribution is accomplished, the steady OAM radiation will be attained as will be seen later in this chapter. To recap briefly, **Figure 4-9** is employed to find the coordinate of each antenna, so to have the exact coordinate the below procedure should be followed as:

- Determine the array center.
- Derive the necessary equation to calculate the spacing distance.
- Use the spacing between any two successive elements as the input parameter in the equation.

By using the **Figure 4-10** and the equation given below, the exact coordinate for each element will be obtained to create a flexible circular OAM array

$$anl = \left(\frac{180 - \theta}{2}\right) \quad \textbf{4-1}$$

$$\theta = \frac{2\pi}{N} \quad \textbf{4-2}$$

$$R = Sp/(2 * cos(70 * pi/180)) \quad \textbf{4-3}$$

where sp is the spacing distance, R is the radius and anl the angle in radians.

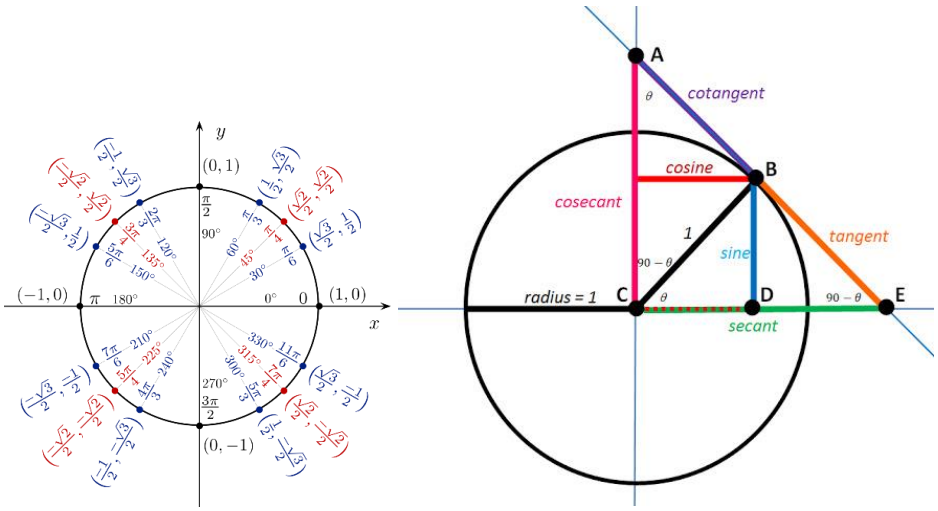

Figure 4-9 Trigonometric function to find array elements coordinates.

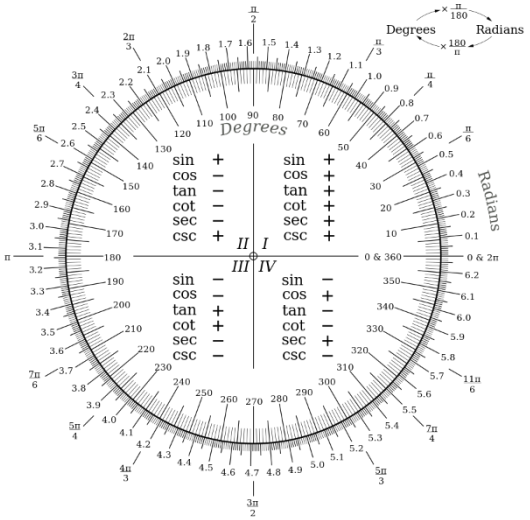

Figure 4-10 Radians and degree conversations.

4.3.2 4-Element UCA-OAM Antenna Array with the Conventional Cavity Reflector (Array I)

Even our target is a low profile CDA antenna array [12]–[14], but we would like to introduce something new in the OAM antennas designs (i.e., the OAM antenna array with the cavity reflector) to have results that can be considered as a reference for our next works. **Figure 4-11**shows the new proposed OAM antenna array work because it is the first time to use the printed crossed-dipole antenna in such a type of arrays according to the best of author's knowledge. It is based on the principle of the UCA. The optimization is for sure conducted here to have the best performance. Thirty five states are made with a step of 0.1mm. The OAM radiated wave is very sensitive to the sequential phase, and the phase can be effected by the mutual coupling. Then, the mutual coupling decreases if the spacing among elements increases, whereas the grating lobes will appear once the spacing increases. Thus, a reasonable spacing distance should be chosen. Furthermore, the situation here is a bit complicated because the operating frequency is 28GHz. If one antenna is slightly shifted, the overall performance of the antenna array will be influenced.

Other issue in the OAM is the gain. Since the radiated OAM beam is diverged into sides rather than to be directed into the boresight direction (i.e., pattern null at the center), the gain at, $\theta = \emptyset = 0°$, is minus. The divergence expands as we move far away from the array. This is one of most disadvantages facing the OAM antenna array. However, the OAM array capability to send multiple signals simultaneously with the same frequency and at the same time encourages researchers and designers to make notable efforts to develop such type of antenna arrays. Consequently, the OAM will be beneficial for short-distance communications where the optical fibers are not easy to be used. The one thing deduced from above is that the linear polarization array has bigger gain than gain of the OAM arrays having the same number of antenna elements.

Table 4-1summarizes few of the proposed OAM array-I performances when varying the sp parameter. As can be seen, the OAM gain tends to increase as the sp increases. However, the linear gain decreases. The sp parameter plays

a vital role to make the array operating in the OAM mode or the linear conventional mode. When the sp≤0.5λ_o, there is no OAM mode but the OAM mode appears when the sp>0.5 λ_o. The table shows only four states for the parameter sp, whereas thirty five states have been done to figure out the best OAM values. Co and cross polarizations are good as expected, especially the null in the pattern center as shown in **Figure 4-12**. This figure shows the 3D gain plots of the OAM array I for the sp states mentioned in **Table 4-1.**

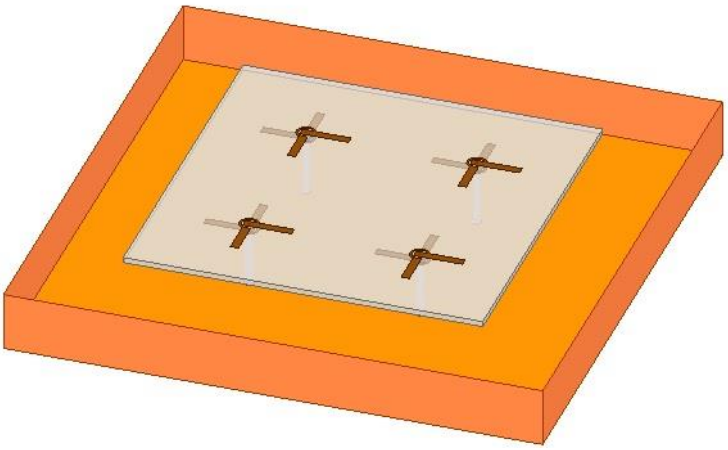

Figure 4-11 3D view of the OAM antenna array I.

The overall dimension (cavity reflector) is $2.24\lambda_o \times 2.24\lambda_o \times 0.5\lambda_o$where it is equal to 24×24mm^{2}and a height of the side walls is $\lambda_o/4$. The OAM array substrate is 16×16mm^2 while all other parameters are the same as

Table 4-1 The OAM antenna array I characteristics for different values of the sp parameter

SP mm	Length in λ_o	OAM gain	Liner gain	Radiation pattern		OAM shape	OAM AR
				yoz-palne	xoz-palne		
6	0.56	7.97	12.3	☒	☒	good	☒
6.1	0.57	8	12.6	☒	☒	good	☒
6.3	0.588	7.8	8.8	☒	☒	good	☒
7.6	0.71	8.2	8.8	☒	☒	good	☒

mentioned in the previous sections.

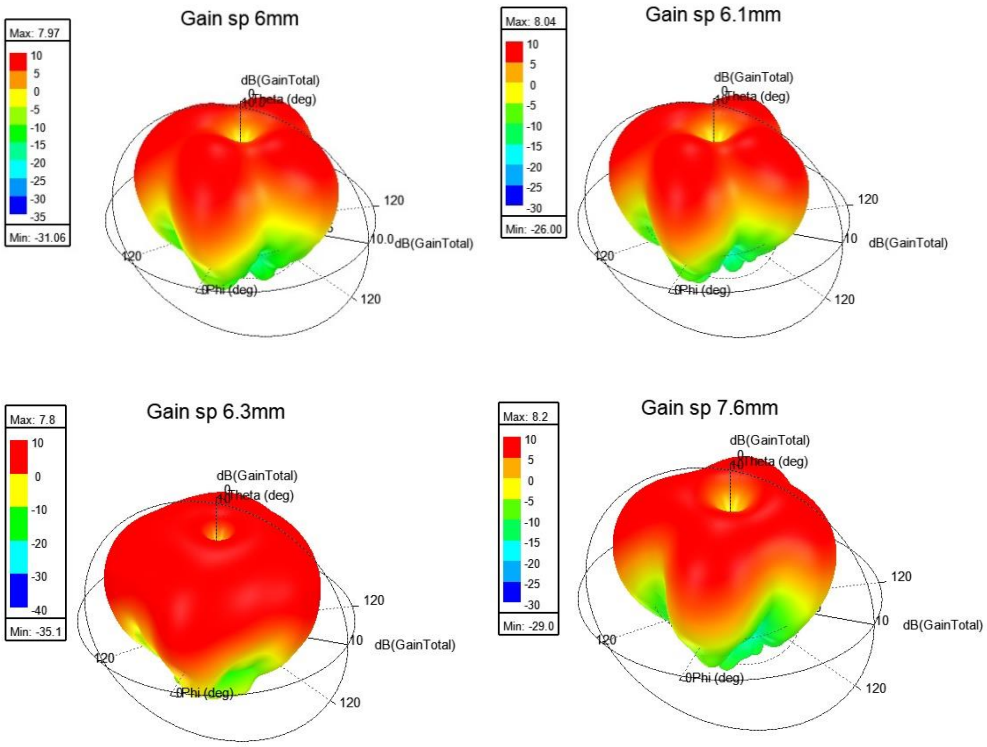

Figure 4-12 3D gain plots of the proposed OAM array I for different values of the sp parameter.

Figure 4-13 demonstrates the 2D polar and rectangular gain plots when the sp parameter varies. Both co-polarization and cross-polarization components are introduced. Here, the null location in the center is very obvious which considers as one of the OAM wave properties. Red traces represent the desired component, while the green traces denote the undesired or unintended components. Ideally, the green traces should not exist, but this is impossible in the practical designs.

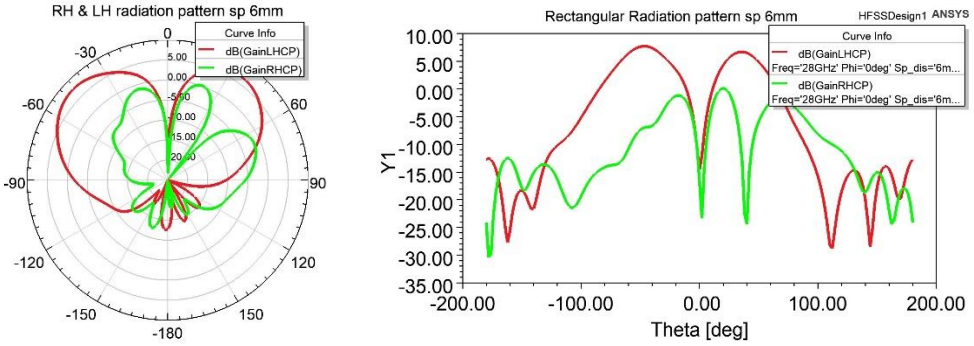

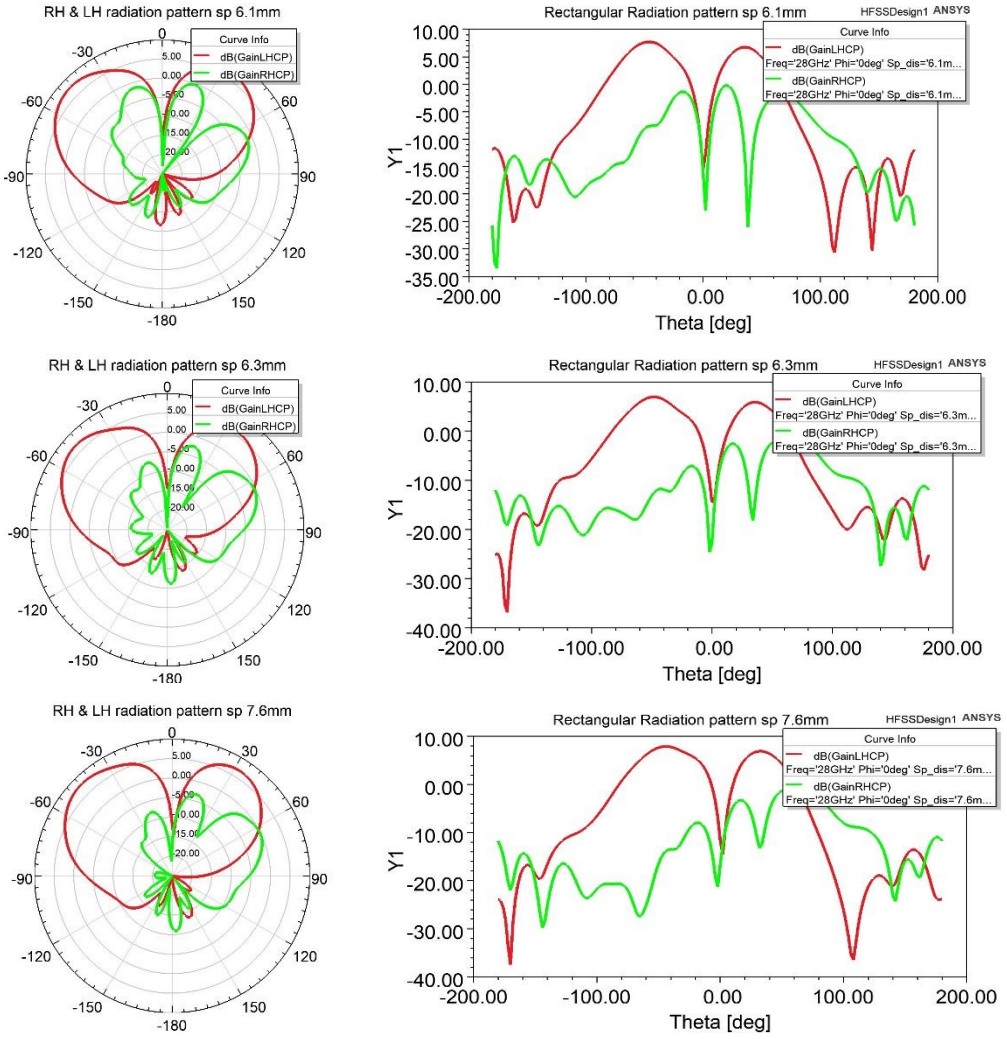

Figure 4-13 2D gain radiation pattern plots of the OAM antenna array I (polar and rectangular plots) for different values of sp parameter.

Also, the return loss of this array is numerically determined using the HFSS software. The S-parameters shows that the array elements resonate at wideband of frequencies, ranging from 19.25GHz to 34.5GHz for port 1 (S11) where for other ports the return loss can be calculated from **Figure 4-14.**

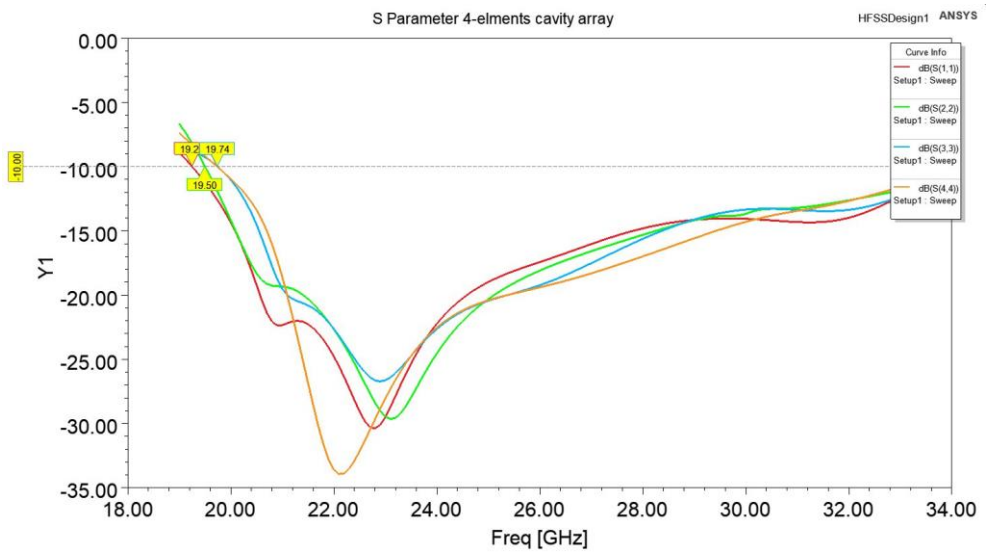

Figure 4-14 RL Snn parameters of the four input elements used in the OAM antenna array I.

4.3.3 The Proposed OAM Antenna Array with AMC Reflector (Array II)

The array is arranged circularly with $2.77\lambda_o$ as circumference, and the spacing distance between elements is 6.7 mm, being equal to $0.62\,\lambda_o$, see **Figure 4-15**. According to these values, finally **we have obtained the OAM EM wave** after optimizing 50 different values for 4-elements UCA antenna AMC reflector. In the same manner as in subsection (4.3.2), we have now an antenna array with very low profile array generating OAM EM waves according to values of the spacing distance SP given in **Table 4-2**.

The shape of the OAM wave is irregular, when the spacing distance is less than $\lambda_o/2$. Then, we can say that there is no OAM wave. Meanwhile, dimensions of the OAM array are very important parameter and should be carefully considered. Hence, the optimum sp is **6.7mm**, see **Figure 4-15**. The trading-off between the overall antenna array dimensions and the OAM EM wave shape is carried out. The overall dimension is $2.18\lambda_o \times 2.18\lambda_o \times 0.0046\lambda_o$ with 11×11 AMC unit cells, referring to the subsection (4.2.1). The array area is 23.41×23.41mm^2 and the array substrate is 14×14mm^2. All other parameters are the same as in the previous sections.

Table 4-2 The OAM antenna array II characteristics for different values of the sp parameter.

SP mm	**Length in λ_o**	**OAM gain**	**Liner gain**	**Radiation pattern**		**OAM shape**	**OAM AR**
				yoz-palne	xoz-pa ne		
5.9	0.55	5.7	10.5	☒	☒	good	☒
6.7	0.62	6.8	11.3	☒	☒	good	☒
6.9	0.64	6.1	10.9	☐	☒	good	☒
7	0.65	5.6	7.1	☐	☒	good	☐
7.7	0.71	6.2	10.7	☐	☒	average	☒
8	0.74	6.2	7.3	☒	☒	good	☐
8.3	0.77	6	7.5	☒	☐	good	☐
8.	0.8	6.16	8.9	☒	☒	good	☐
8.9	0.83	6.2	8.9	☒	☒	good	☒
9.2	0.86	6.1	8.96	☒	☒	good	☐
10	0.93	5.7	6.98	☒	☐	average	☐
11	1.02	6.5	7.6	☒	☒	average	☐

Where:

- The OAM shape (good, average, or even bad). This means that there is OAM EM wave and as symmetrical as possible in yoz and xoz planes with null in Theta equal zero.
- If the rectangular box is checked, it has OAM, and if not, it has no OAM waves.

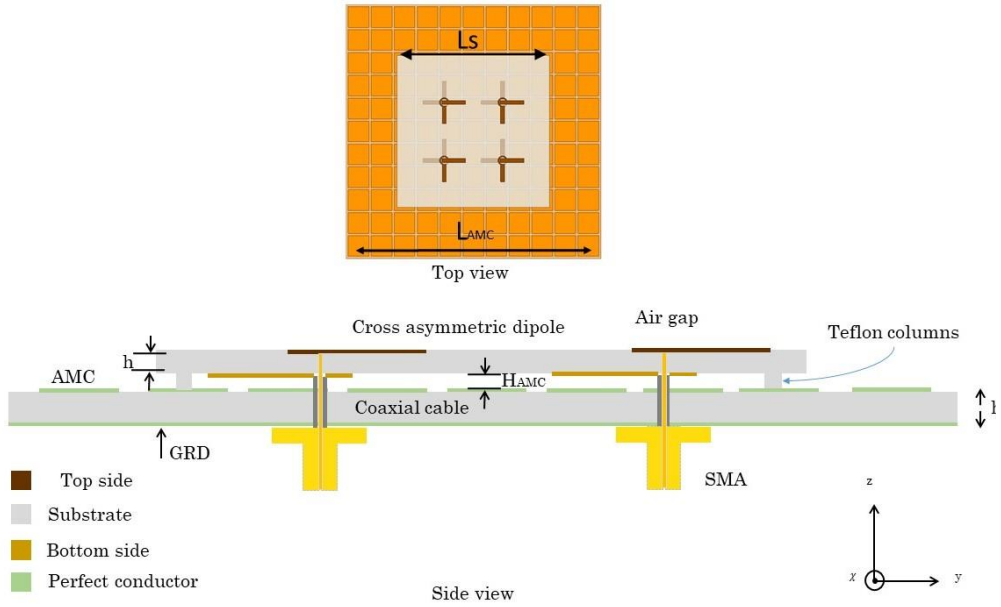

Figure 4-15 Structure of the 4-elemnet OAM array II (top and side views).

When the spacing distance sp=6.7mm in the **Table 4-2,** the max OAM gain is 6.8 dB with very good OAM shape, depicted the phenomena of quantum theory of OAM in radio frequency or in optical OAM. The liner gain is 11.3 dB. The 2D radiation patterns are depicted the null (vortex) at center (Theta=zero) for the two planes (yoz and xoz), being symmetrical. **Figure 4-16** and **Figure 4-17** show co and cross-polarization components with good results, and especially the null when theta=zero, it shows -18 dB less than the main beam.

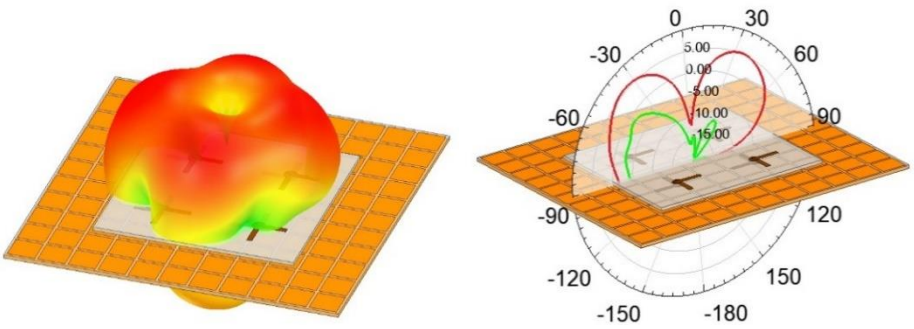

Figure 4-16 3D and 2D gain plots (along with the array models) of the proposed OAM antenna array II.

The IBW extends from 25.03GHz to 32.55GHz for port1 with -17dB return loss at 28 GHz, as shown in **Figure 4-18**. Although the return loss are non-identical, all ports have wide impedance bandwidths. When compare the results with results of the array I, the IBWs are less. This belongs to that the AMC structure has narrow bandwidth, resulting in a whole structure with

less bandwidth. In addition, the proposed array II has smaller front-to-back lobe ratio. The Array I is integrated with cavity that has four side walls, preventing the back radiation. However, the array II is low profile structure, being the main goal in this research.

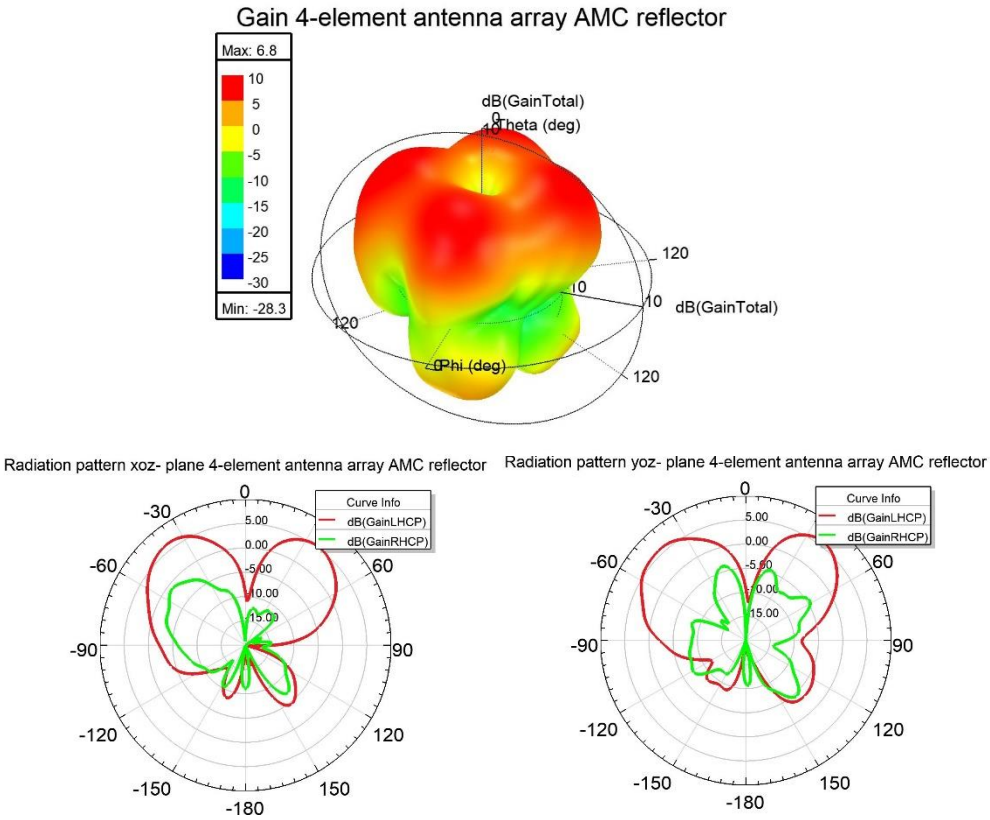

Figure 4-17 3D and 2D OAM waves of the proposed array II.

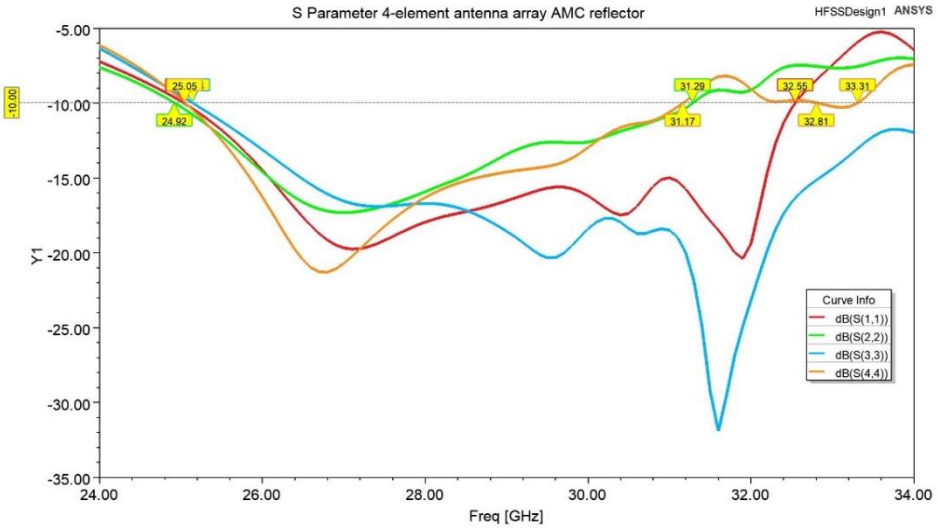

Figure 4-18 The RL Snn of the individual elements used in the proposed array II, where n=1-4, the port number.

In OAM's antennas, there is a very important parameter, which is the generated **mode degree** and a polarization of the mode (i.e., right-handed RH or left-handed LH component) as well as the liner mode (zero degree). In the last two proposed arrays, it is possible to generate three modes (0, +1 and -1) as depicted in **Figure 4-19**. Form the figures, it is very obvious that directions of phase progressing are like the vortex wave supporting our theoretical explanations mentioned in introductory chapters. This depends on how to feed the individual antennas with phase delay and which direction the elements will be fed. If we control the procedure to generate modes simultaneously, the spatial multiplexing property will be obtained readily as will be shown later in this chapter.

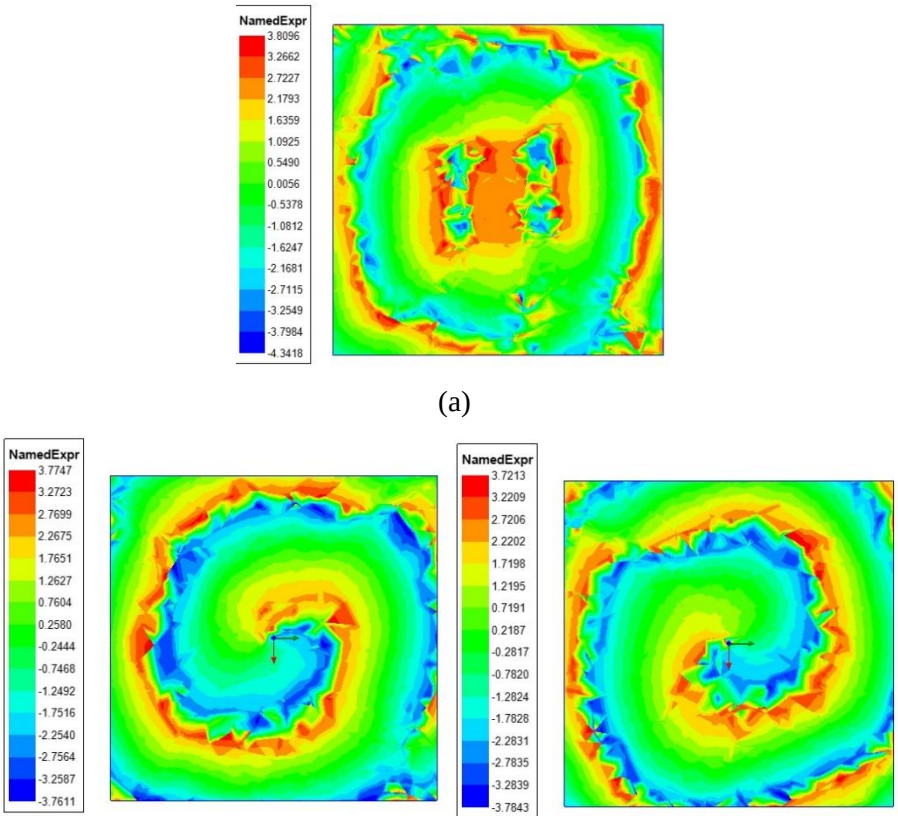

Figure 4-19 Near-field phase distributions at 28 GHz (a) state 1(0 mode) (b) state 2 (+1) (c) state 3 (-1).

In addition to the previous results, **Figure 4-20** depicts plots of the power density in near field. The density of power likes sequentially rotation with radiation elements of the array. This type of radiation is different from the

one generated by the liner radiation. The phase sequence is an azimuthal helical phase changing with power [3].

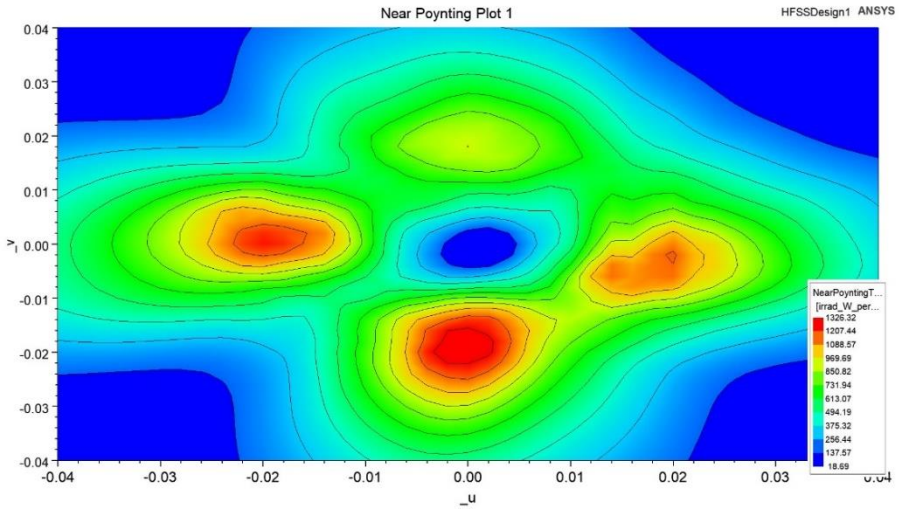

Figure 4-20 Contour plot of the near field of power density of the proposed array II.

4.3.4 8-element UCA-OAM Antenna Array with Flat Reflector (Array III)

Eight elements are circularly arranged following the procedure given above to calculate a location of each element and the distance among elements to produce the optimum OAM wave. As known, as a number of elements increases, a number of generated OAM modes increases as well. If a number of the generated modes increases, the channel capacity increases, thereby increasing a number of subscribers which considers one of the goals sought by communication companies. As usual, the printed crossed-dipole antenna is the element employed in the proposed array, but in this array the flat reflector will be utilized with height of $-\lambda_o/4$ from the antenna driven elements. Also, the AMC reflector with 19×19 unit cells assumed to be used, but this reflector has 361 patch, resulting in a huge computational with no possibilities to carry out this task with normal computers. Furthermore, the feeding network will be complicated as well. Many suggestions will be seen in a chapter of the Future works regarding in a large number of elements used in the OAM integrated with a large feeding network, see (5.2) next chapter. The structure of the array **III** is bigger with over all dimensions of 42×42×2.65 mm^3, and the array substrate has dimensions of 28×28×0.25 mm^3. At the spacing distance among elements 7.3 mm

($0.68\lambda_o$) is the best value as depicted in **Figure 4-21** along with the 3D gain plots of the radiation pattern.

The OAM wave is very unique and never been reported like this one. However, the direct feeding with coaxial cables is used here again as in the two previous proposed array models. To brief the results, the OAM max gain is 9.2 dB with efficiency of 96.8%. In **Figure 4-22 (b and c),** the 2D radiation patterns of the co and cross-polarization components gain plots are shown. Both xoz and yoz planes are demonstrated, being symmetrical. Because the structure is more complicated and needs high computation device to be simulated, the array **III** is simulated only in 1 GHz range from 27.5 GHz to 28.5GHz. The return loss ranges from 15.5 dB to 17.5 dB for all ports as shown in **Figure 4-22 (a).**

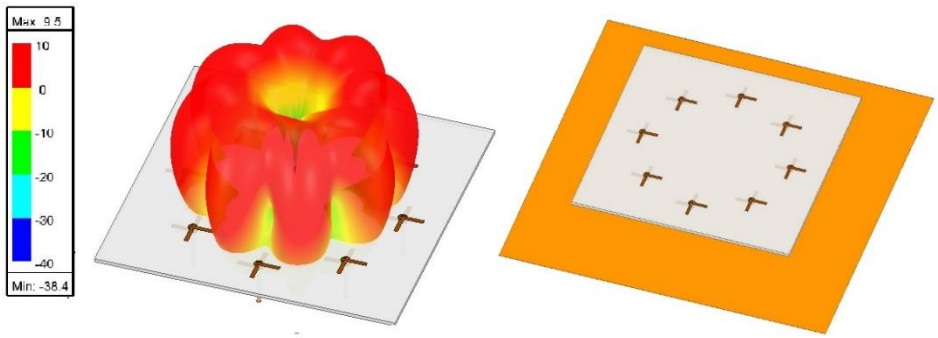

(a) **(b)**

Figure 4-21 8-element OAM antenna array III (a) 3D gain (b) the model 3D view.

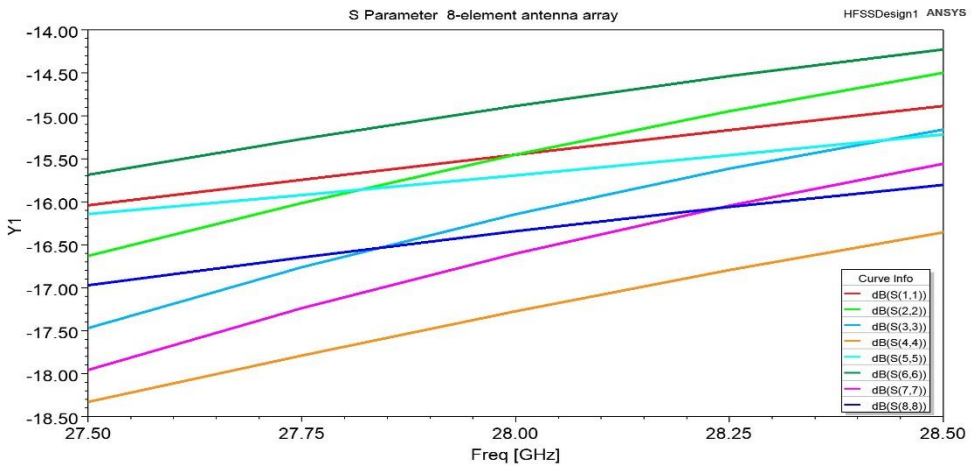

(a)

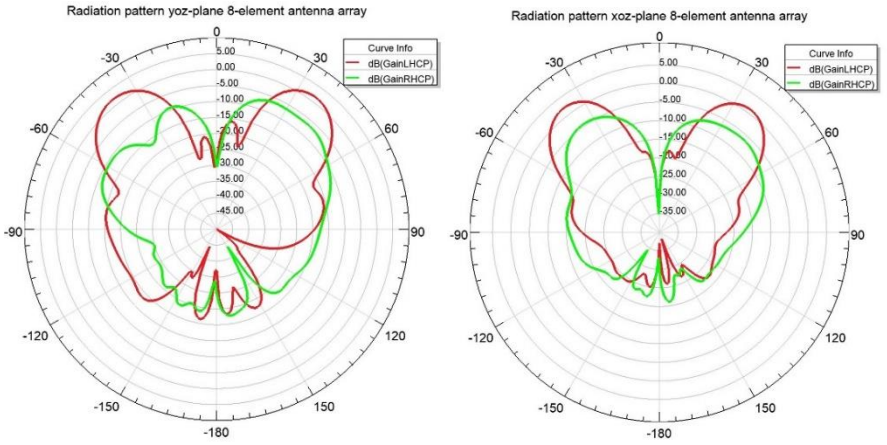

(b) (c)

Figure 4-22 8-elements OAM array III (a) S parameters (b) and (c) 2D gain radiation plots for the yoz and xoz planes, respectively.

The OAM antenna array can generate 3 modes for both negative (LH) and positive rotations (RH), ($\mp$1, $\mp$2and $\mp$3) with zero mode. However, **Figure 4-23** shows only the near field phase progressive for the -3 and +3 for the sake of simplicity.

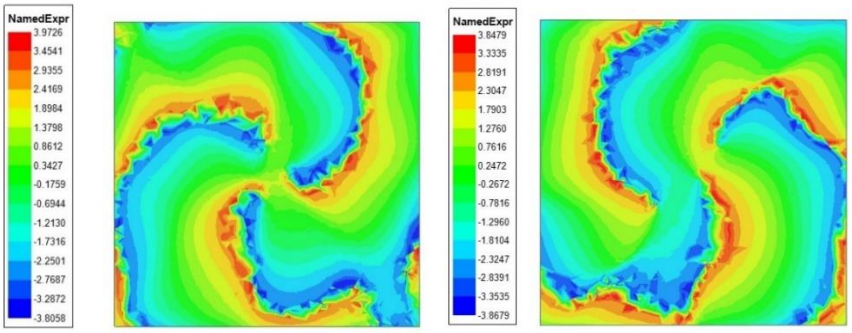

(a) (b)

Figure 4-23 Near-field phase distributions a) RH mode +3 b) LH mode -3

4.3.5 Smart Feeding Network (Butler Matrix 4×4)

Referring to the subsection (2.5), the Butler Matrix and Rotman lens are adopted to feed the OAM antenna array to make it operating at different modes concurrently.

To have the OAM EM wave from the array, the feeding network should provide the required sequential phase for each antenna input port. The 4×4

Butler matrix is really challenge to realize the required sequential phase, where there are many reported designs [51]–[53]. Typically, the Butler

matrix beamforming network is used to generate multiple orthogonal beam patterns. The orthogonal term also is very important parameter to have the spatial multiplexing. However, conventional Butler matrices do not provide the exact phase sequences, so some slight modifications have been made to make them compatible what it is required in the OAM arrays. **Figure 2-14** shows one of them. The reference [16] gives a glance to our special design.

In Chapter 2, the subsection (2.5), we have explained a job of each part in the Butler Matrix. Therefore, we will directly present the whole structure model and then explain the current flow in the Butler matrix to clarify the attaining phase delay through this microwave signal journey. **Figure 4-24** shows the model of Butler matrix that have four input ports and four output ports, five 90^ohybrid couplers, one cross over, and two 90^o phase shifters and other phase shifters with different phase degrees.

In **Figure 4-25,** the signal coming from the input port B1, as an example, will be marked throughout its journey in the circuit. According to the equation in the subsection (0), the transmission line width is found. For 50Ω and 35.3Ω, the transmission microstrip lines are examples used in the Butler matrix. When the signal arrives at the point X, it will be divided into two signals by the hybrid coupler with 90degree phase shift. The signal at point V has 0degree phase shift, and the signal at point Y has-90^ophase shift. Then, we have two paths for the signal flow (V and Y).

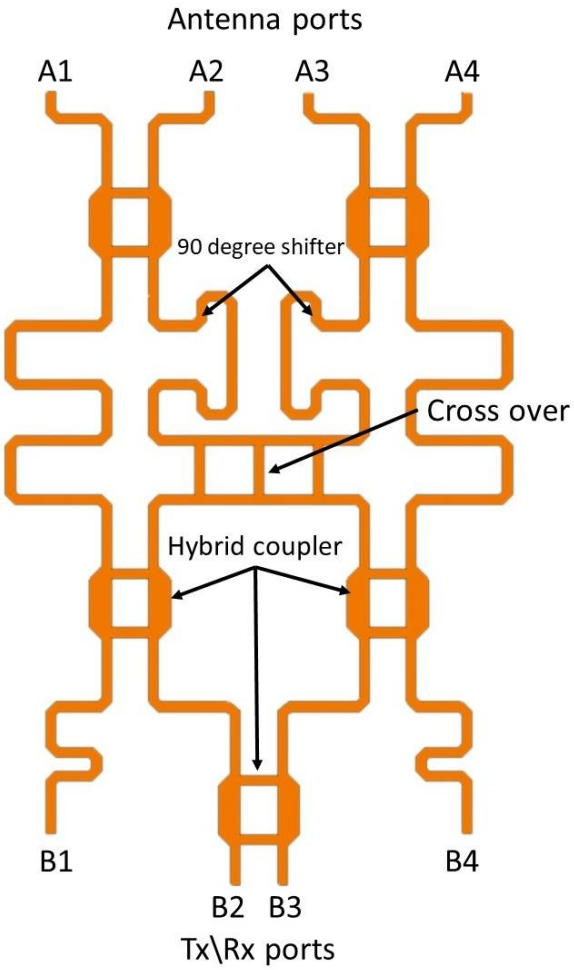

Figure 4-24 The final structure design of the Butler matrix feeding network.

The signal leaves point Y to enter the crossover to reach the point F. This travel needs time, so the delay phase shift becomes true. To compensate this delay into the signal leaving the point V, extra transmission length is added. This procedure considers one of the modifications achieved on the Butler matrix, and aid to keep the phase difference between signals at points G and F -90degree. The signal then leaves the point G to go through the next hybrid coupler, reaching the points A1 and A2 with 90degree phase shift. Just keep in mind that there are several extra transmission lines which are added to compensate the phase delay added by the main components of the Butler matrix. For the other signal at the point F, it will enter the 90degree hybrid coupler at point S passing through 90 degree phase shifter. Thus, the signal at the point S is lagged by 180degree from the signal at the point K. After that, the signal at the point S enters the 90degree hybrid coupler and leaves to reach the points A3 and A4 with lag phase difference of 180degree and 270 degree, respectively, compared to the first reference output port A1.

In summary, the signal, which enters the entire Butler matrix at the point B1, will be divided into four signals with phase differences ($\boldsymbol{0^o, -90^o, -180^o\ and\ -270^o}$)**, resulting in the** mode (+1). In the same manner for the input port B4, we can get on phase sequence ($\boldsymbol{-270^o, -180^o, -90^o\ and\ 0^o}$), mode (-1). The other two ports B2 and B3 result in the liner polarization radiation ($\boldsymbol{90^o, 180^o, 90^o\ and\ 180^o}$). In the next step, we should test all components forming the Matrix individually.

A- Hybrid coupler 90^o

The hybrid coupler is designed using two different widths for the

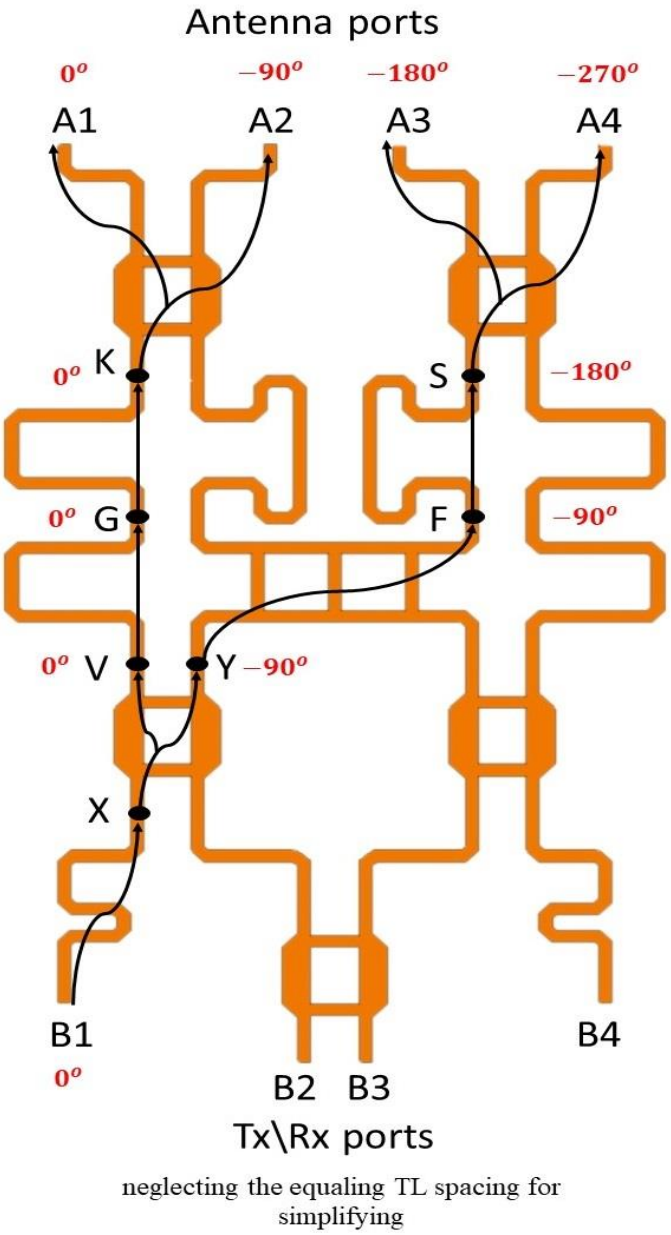

Figure 4-25 The signal flow with phase shifts indications when the port B1 is employed.

transmission lines (i.e., different characteristic impedance) according to the theory introduced in Chapter 2. We have used 50Ω and 35.33Ω TLs on a substrate which is Rogers RT/duroid 6010/6010LM with permittivity of 10.2 and dielectric loss tangent of 0.0023, and a thickness of 0.25mm. **Figure 4-26** depicts the hybrid coupler model. **Table 4-3** shows dimensions of the structure.

The results were completely compatible with the reference David Pozar [25]. The behavior of return loss of all port was:

Table 4-3 The Hybrid coupler 90^o dimensions, unit (mm).

$\lambda_g/4$	W1	W2
1.0625	0.18	0.4
L2	L1	h
0.7	2.7225	0.25

- Phase difference between the S21 and the S31 is 89.8 degree, see **Figure 4-27 (a).**
- The transmission coefficients S21 and S31 are almost -3.6dB.
- The isolation port S41 is close to -18dB at 28GHz, see **Figure 4-27 (b)**.
- **Figure 4-27 (c)** presents the output variation in the phase difference between the ports 2 and 3.

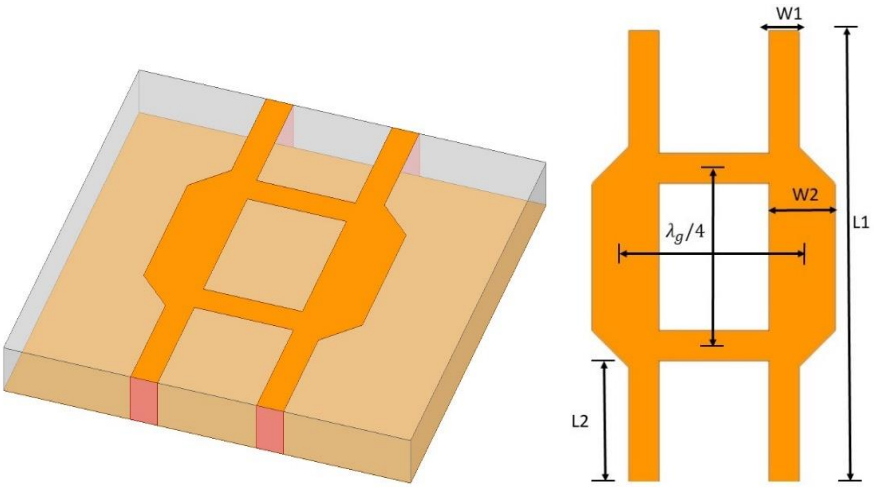

Figure 4-26 90^o Hybrid coupler.

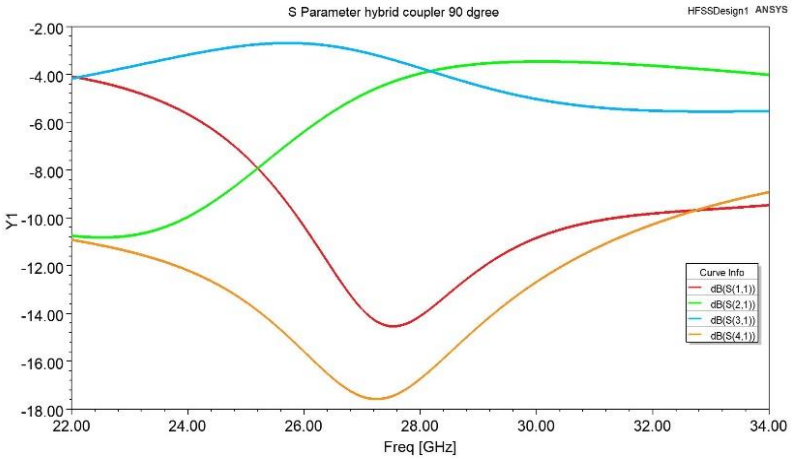

(a)

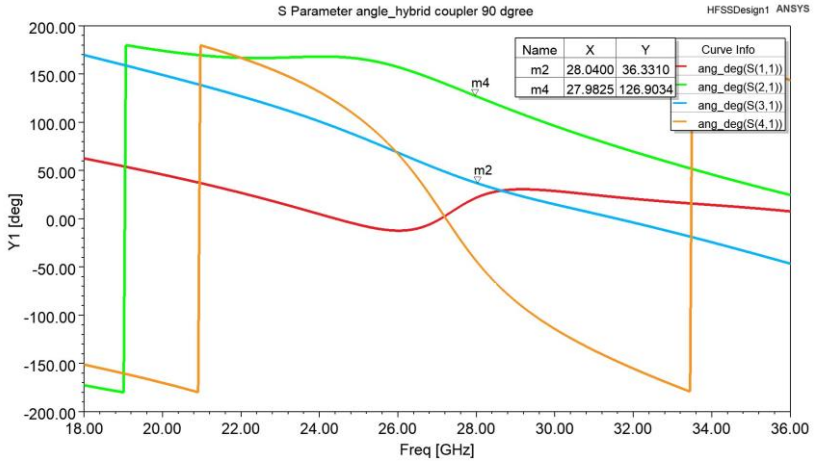

(b)

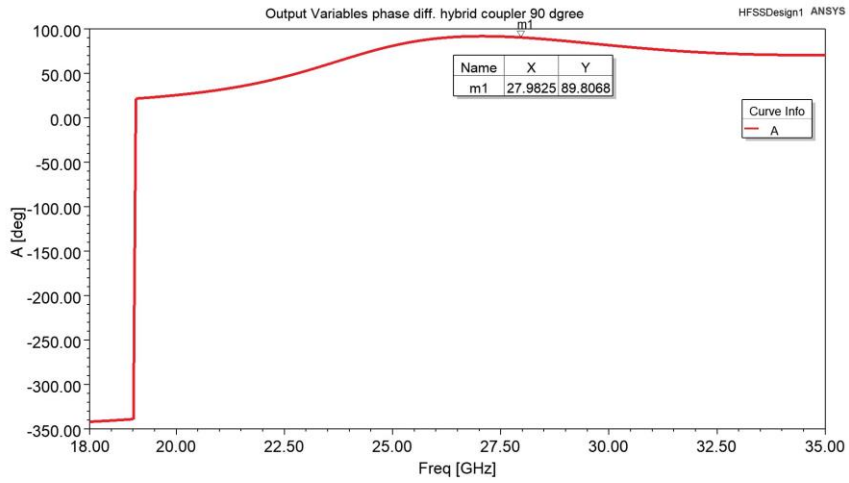

(c)

Figure 4-27 S parameter of hybrid coupler (a) in dB (b) in dgree (c) phase different S21 and S31.

B- Cross Over (0 dB coupler)

The crossover is another component in the Butler matrix feeding network. It consists of two 90degree hybrid couplers connected in series, but the

structure used here is the compact version. This structure aids to route the signal from path to another without interruption. **Figure 4-28** shows the structure model with all indicated parameters. **Table 4-4** provides the structure dimensions.

Table 4-5 The Cross over dimensions, unit (mm).

$\lambda_g/4$	L1	h	W
1.0625	2.7225	0.25	0.18

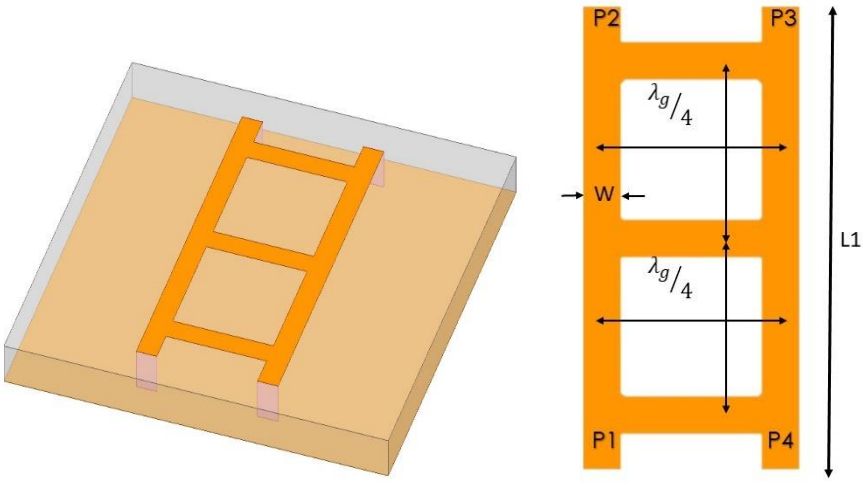

Figure 4-28 Crossover model.

The S parameters given in **Figure 4-29** show that when the signal enters the port 1, it will appear entirely at the port 3. No outputs are at the ports 2 and 4.

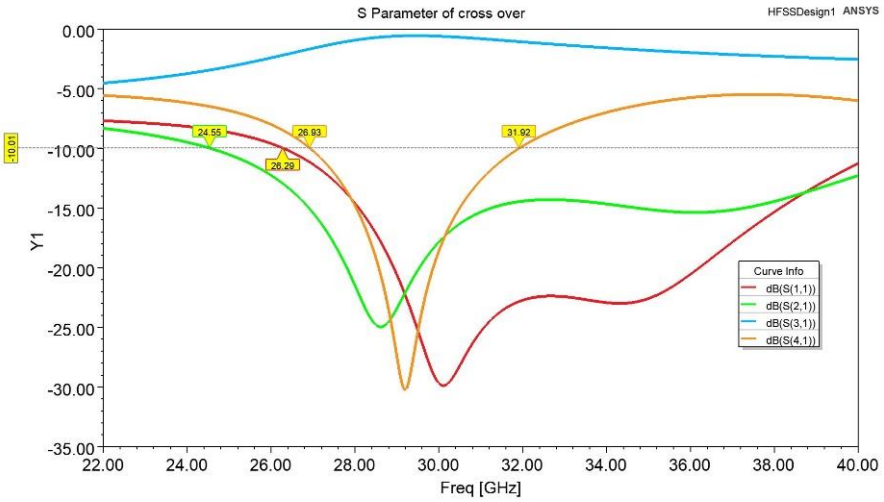

Figure 4-29 S parameters of the Crossover when the signal enters the port 1.

C- Phase Shift 90^o

Simply, the phase shifter is carried out by introducing an extra length for the transmission lines. This fixed physical length of the transmission line has an electrical length varying with the frequency, see **Figure 4-30**.

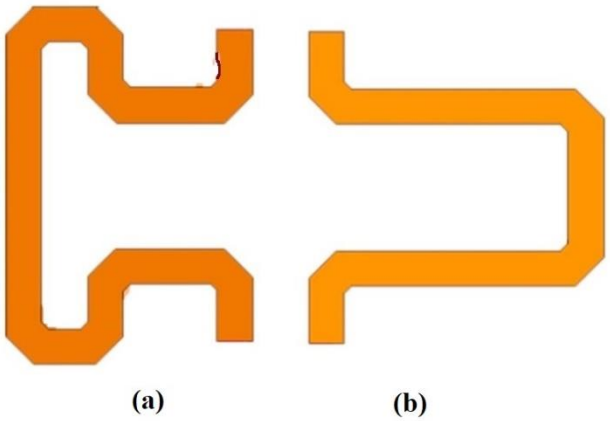

Figure 4-30 Phase shift (a) 90^o shift (b) shifter less by 90^o physical length.

The S parameters are found here again to check its functionality. In this part, we only care about the phase. It is like to be the normal transmission line, as shown in the **Figure 4-31**, the coupled ports S12 or S21 are close to zero -0.2 dB for both and the return ports S11 and S22 are -28 dB.

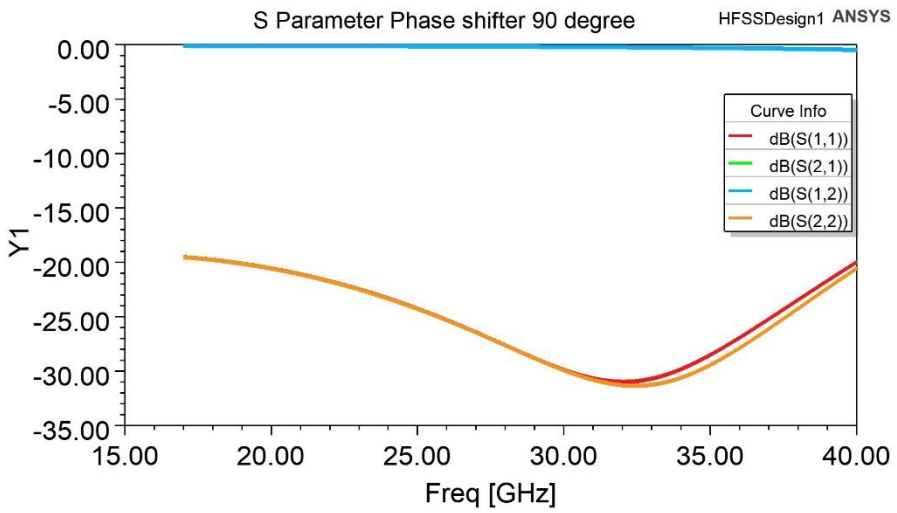

Figure 4-31 S Parameters 90degree phase shifter.

4.3.6 Butler Matrix Test

All designs at high frequencies are sensitive to the any small extra variations in a length of the transmission line. Thus, when introducing the Butler matrix feeding network, we were conscious about that. As a consequence, the feeding network should be tested and verified. The phase here is more important than the magnitude to accomplish the OAM EM wave. **Figure 4-32** below shows all Butler feeding network stages

Each stage has 4 input ports (1, 2, 3 and 4) and 4 output ports (5, 6, 7 and 8). We will test the current flow according to the paths and we will compare the phase angle between the paths. They will be in-phase if there is no difference in the transmission line length.

- In stage-1, the current flow will be tested as (S51, S62, S73 and S84), because we want to know if the paths are in phase with each other. Are the same?
- In stage-3, the current flow will be tested as (S51, S72, S63 and S84), because there is a crossover in the path of port 2 and port 3.

Figure 4-33 shows all the paths having the same phase with each other, while there is 87.6degree phase difference in the stage-4.

Now, we have finished the discussion of the whole Butler matrix along with its results. **Figure 4-34** shows the S parameters of all input ports. It starts from -18dB to -47dB. The progressive phase difference is clear from the port 1 to the port 4, and when the direction is reversed, from the port 4 to the

port 1. As we designed. Because the ports 2 and 3 have the same phase difference, we have showed results for one of them.

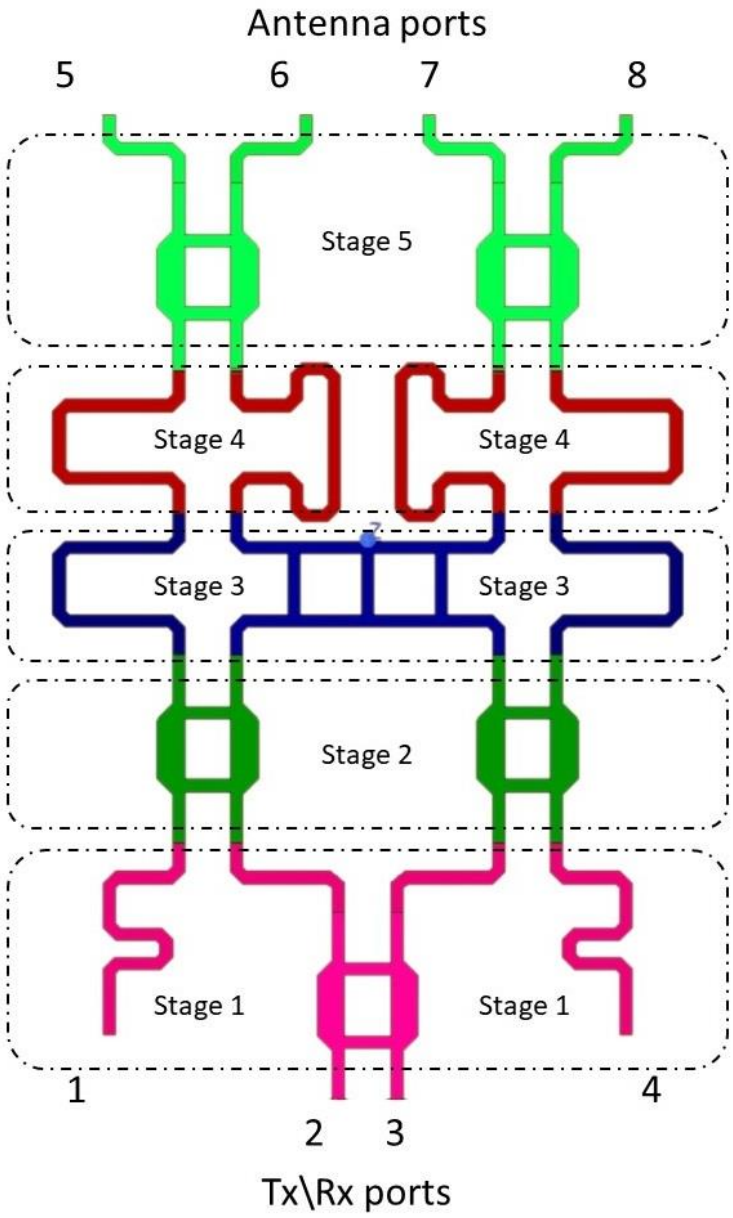

Figure 4-32 The Butler matrix divided as stages to understand the signal paths.

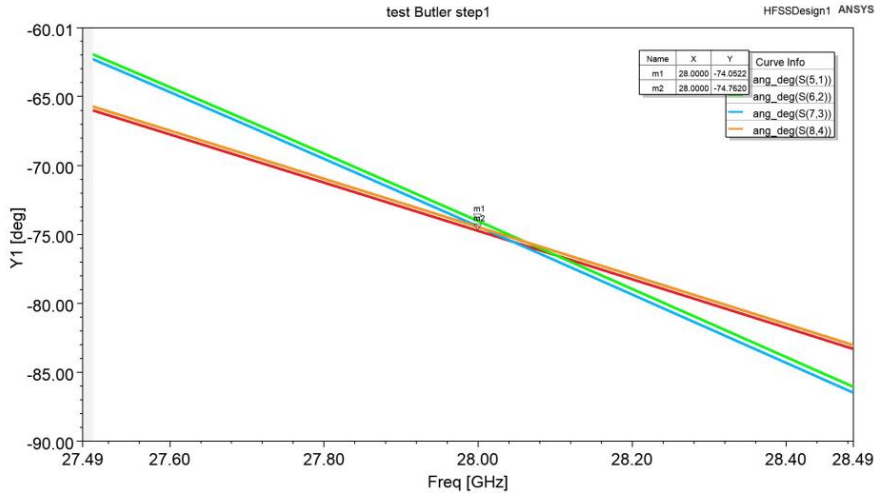
test Butler step1
HFSSDesign1 ANSYS
Curve Info
ang_deg(S(5,1))
ang_deg(S(6,2))
ang_deg(S(7,3))
ang_deg(S(8,4))
Name X Y
m1 28.0000 -74.0522
m2 28.0000 -74.7620
Y1 [deg]
-60.01
-65.00
-70.00
-75.00
-80.00
-85.00
-90.00
27.49 27.60 27.80 28.00 28.20 28.40 28.49
Freq [GHz]

(a)

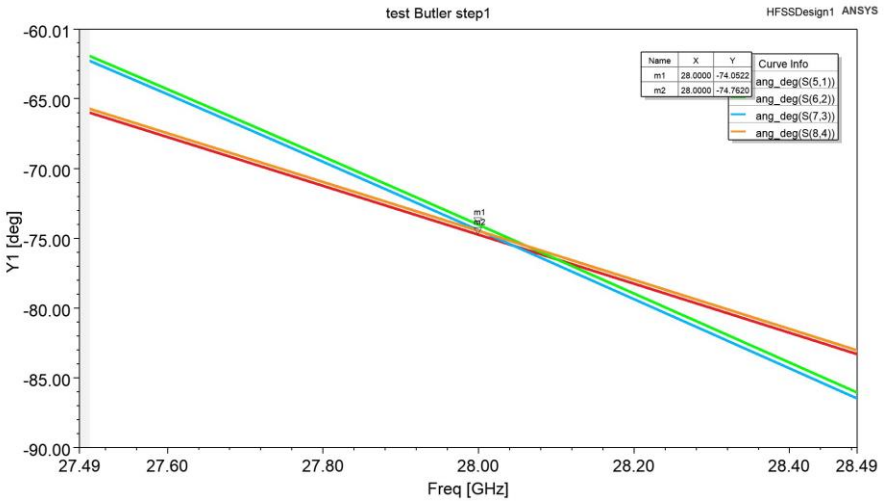
test Butler step1
HFSSDesign1 ANSYS
Curve Info
ang_deg(S(5,1))
ang_deg(S(6,2))
ang_deg(S(7,3))
ang_deg(S(8,4))
Name X Y
m1 28.0000 -74.0522
m2 28.0000 -74.7620
Y1 [deg]
-60.01
-65.00
-70.00
-75.00
-80.00
-85.00
-90.00
27.49 27.60 27.80 28.00 28.20 28.40 28.49
Freq [GHz]

(b)

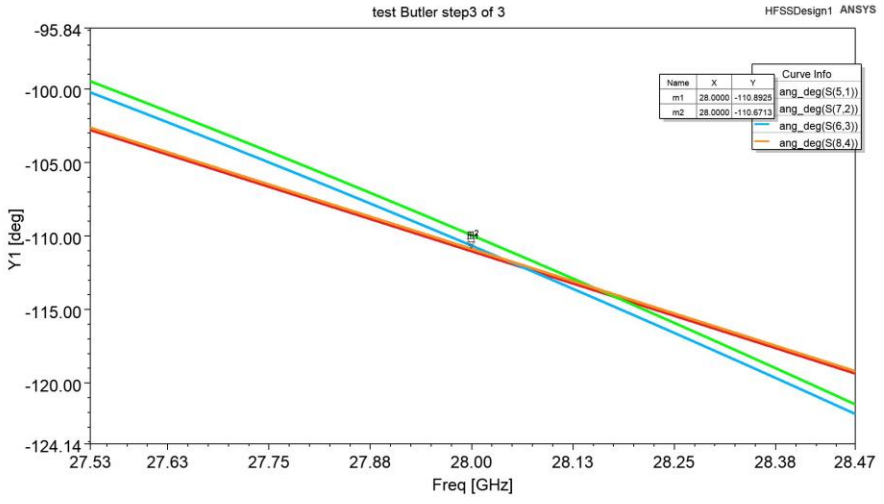
test Butler step3 of 3
HFSSDesign1 ANSYS
Curve Info
ang_deg(S(5,1))
ang_deg(S(7,2))
ang_deg(S(6,3))
ang_deg(S(8,4))
Name X Y
m1 28.0000 -110.8925
m2 28.0000 -110.6713
Y1 [deg]
-95.84
-100.00
-105.00
-110.00
-115.00
-120.00
-124.14
27.53 27.63 27.75 27.88 28.00 28.13 28.25 28.38 28.47
Freq [GHz]

(c)

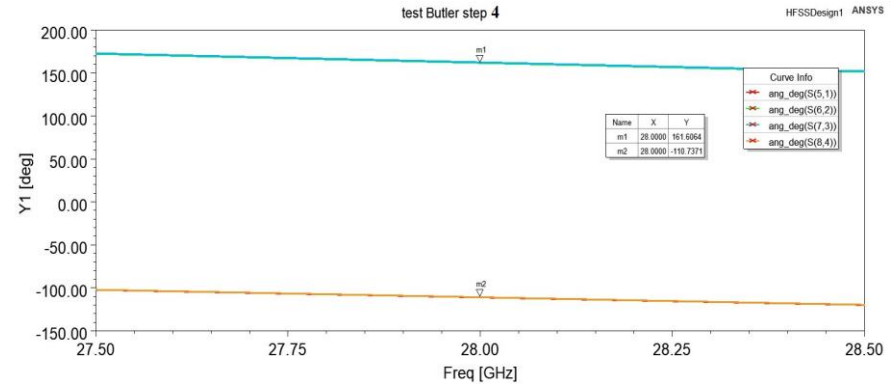

(d)

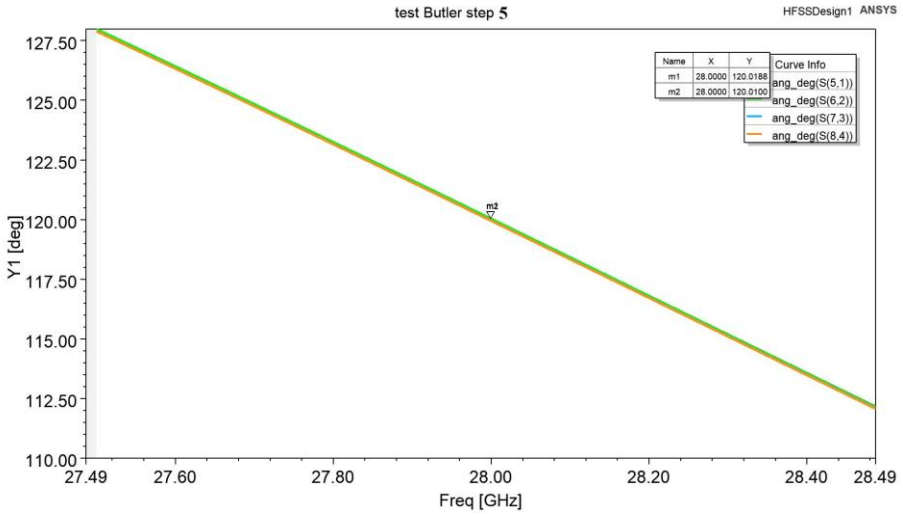

Figure 4-33 Tests of the Butler matrix feeding network stages (a, b, c, d and e) are (stages 1,2,3,4 and 5) respectively.

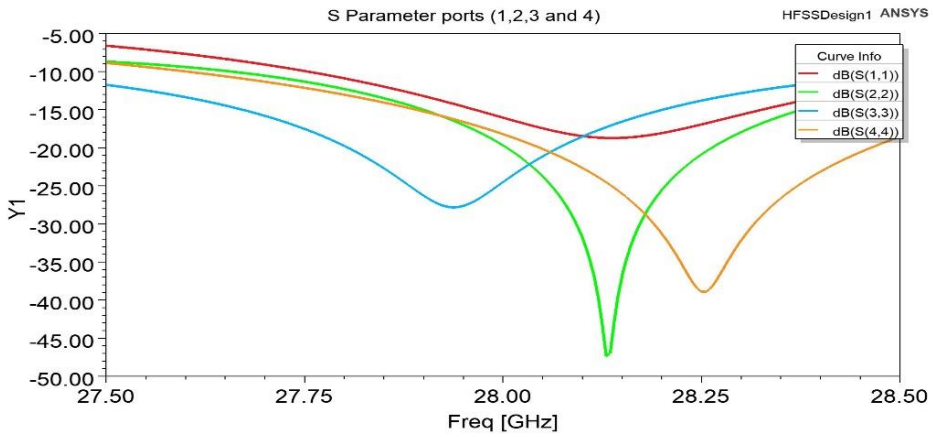

(a)

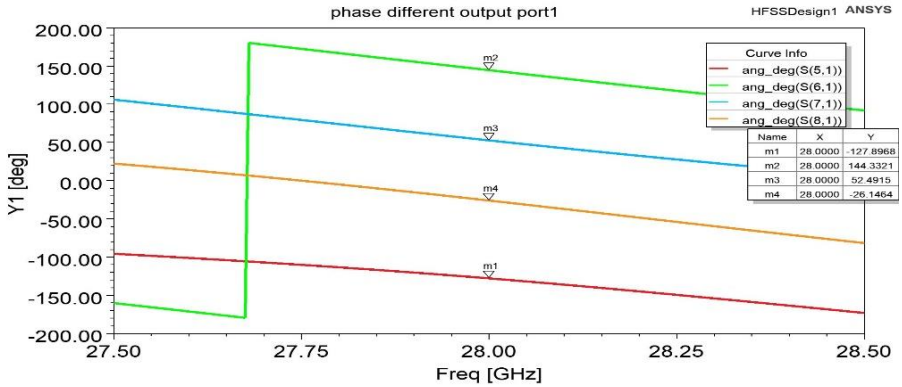

(b)

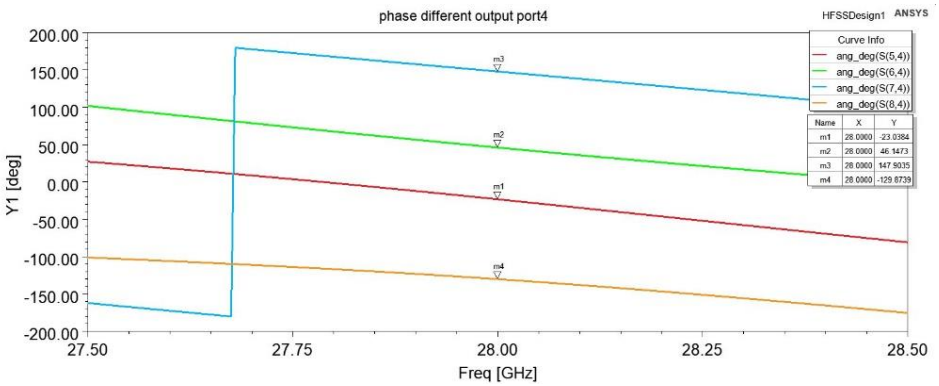

(c)

Figure 4-34 The Butler Matrix feeding network results a) the S parameters of all ports b) the progressive phase difference of the port1 c) the progressive phase difference of the port4.

4.3.7 Actual Butler Matrix Feeding Network with OAM Antenna Array Ⅳ

The antennas radiation field should be asymmetrical in order to obtain the helical phase front. As a helical wave can be generated, the azimuthal phase-dependent factor exp($jl\varphi$) is used, where l is the order of the OAM mode and φ is the azimuthal angle [3]. For instance, if we have 4-element OAM antenna array, the continuous phase intervals can be estimated using $2\pi l/N = \mp\pi/2$ since the OAM order is set to $l = 0, \mp 1$ and a number of the antenna elements is set to N = 4.

When the port 1 is excited, the output ports A1, A2, A3, and A4 have equal magnitudes and specific phases of (0°, −90°, 180°, and −270 °), respectively. When Port 4 is excited, the output ports A1, A2, A3, and A4 have also equal magnitudes but with specific phases of (-270°, −180°, -90°, and 0 °), respectively. If the input port 1 is excited, the mode 1 will be obtained. Furthermore, if the port4 is excited, the mode =-1 will be obtained.

In contrast, when port 2 is excited, the output ports A1, A2, A3, and A4 have equal magnitudes and specific phases of (-90°, −180°, -90°, and −180 °), whereas the situation will be reversed when exciting port 3 to have a sequence of phases of (-180°, −90°, -180°, and −90 °). **Figure 4-35** The whole OAM antenna array IV Butler matrix feeding network + the printed crossed-dipole OAM antenna array with indications of the input ports .

Because the feeding network has four inputs, we have four return loss Snn, where n=1,2,3,4. If one of the feeding network inputs is excited, others are matched with a load of 50ohm. This aids to prohibit reflections from these input ports. The antenna array S parameters (S11, S22, S33 and S44) are determined using the HFSS software, see **Figure 4-38**. The results are obtained with a frequency range of (27.5-28.5) GHz. S11, S22, S33, and S44 are -15.5dB, -18.25dB, -21dB and -24.1dB, respectively. These values confirm that our design is well matched at that range of frequencies. Also, this small range of frequencies is used because of limited computational resources. The final physical OAM antenna array IV size is $3.17\,\lambda_o \times 2.18\lambda_o \times 0.07\lambda_o$ and in millimeter 34×23.4×0.8mm^3.

Integrating the Butler matrix feeding network with extra transmission lines on one substrate eases the fabrication process in the future if the required resources become available. The coaxial probe is utilized to transfer the power from the feeding network to the antenna elements in the array as depicted in **Figure 4-39**. The antenna results mainly depend on the feeing excitation ports. The realized gains of the OAM antenna array are 4.8dB, 4.8dB, and 7.6dB and efficiencies are 75%, 75% and 83.5%, when exciting port 1, port 4 and port 2or3, respectively, as depicted in **Figure 4-38**.

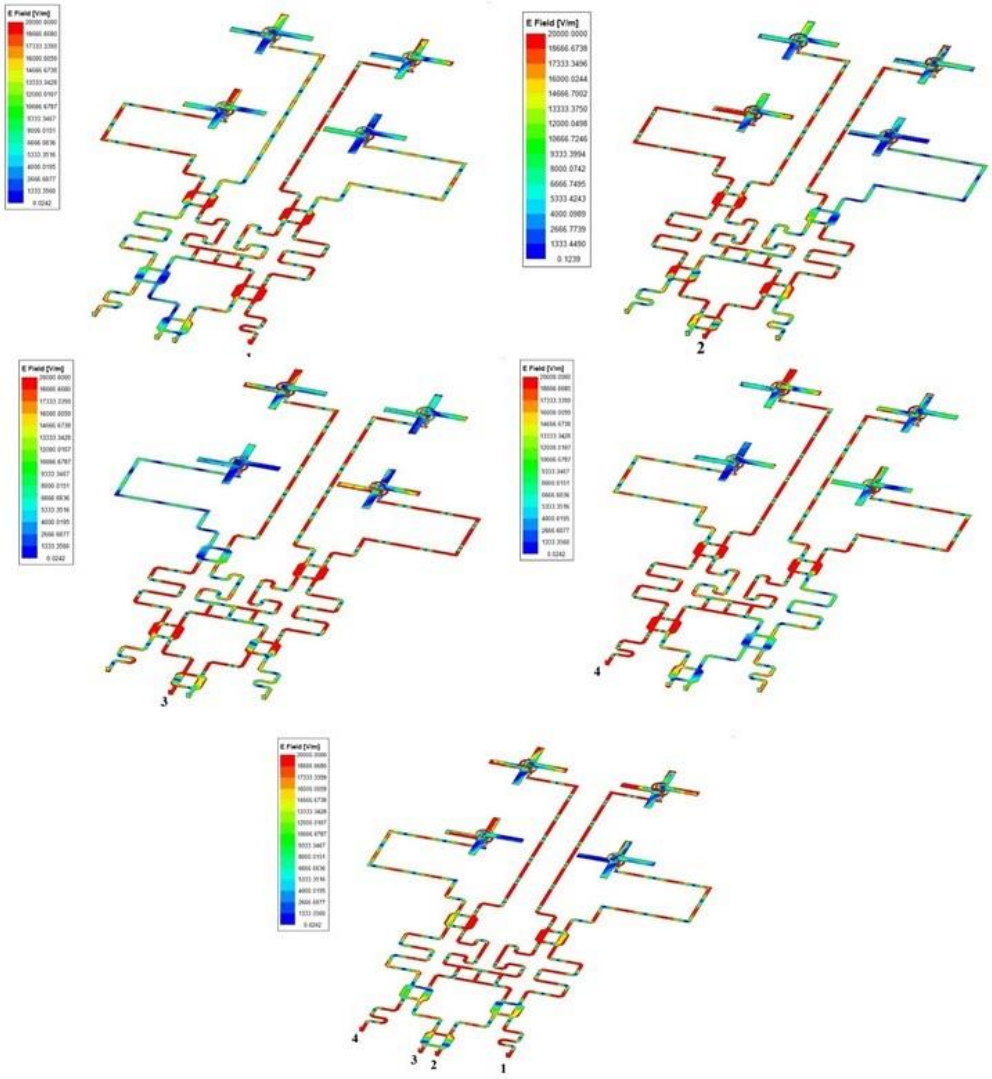

Figure 4-35 The whole OAM antenna array IV Butler matrix feeding network + the printed crossed-dipole OAM antenna array with indications of the input ports .

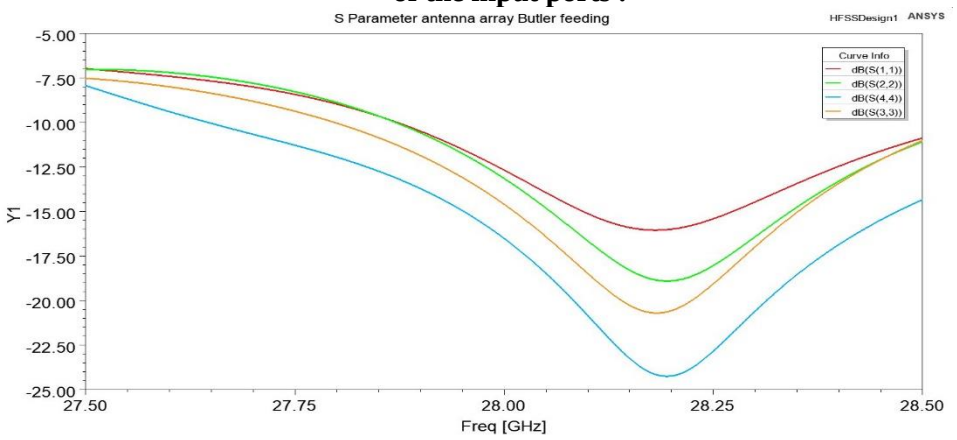

Figure 4-36 The return loss Snn of the proposed OAM antenna array IV (S11, S22, S33 and S44) where all are below the -10dB at the interesting frequency.

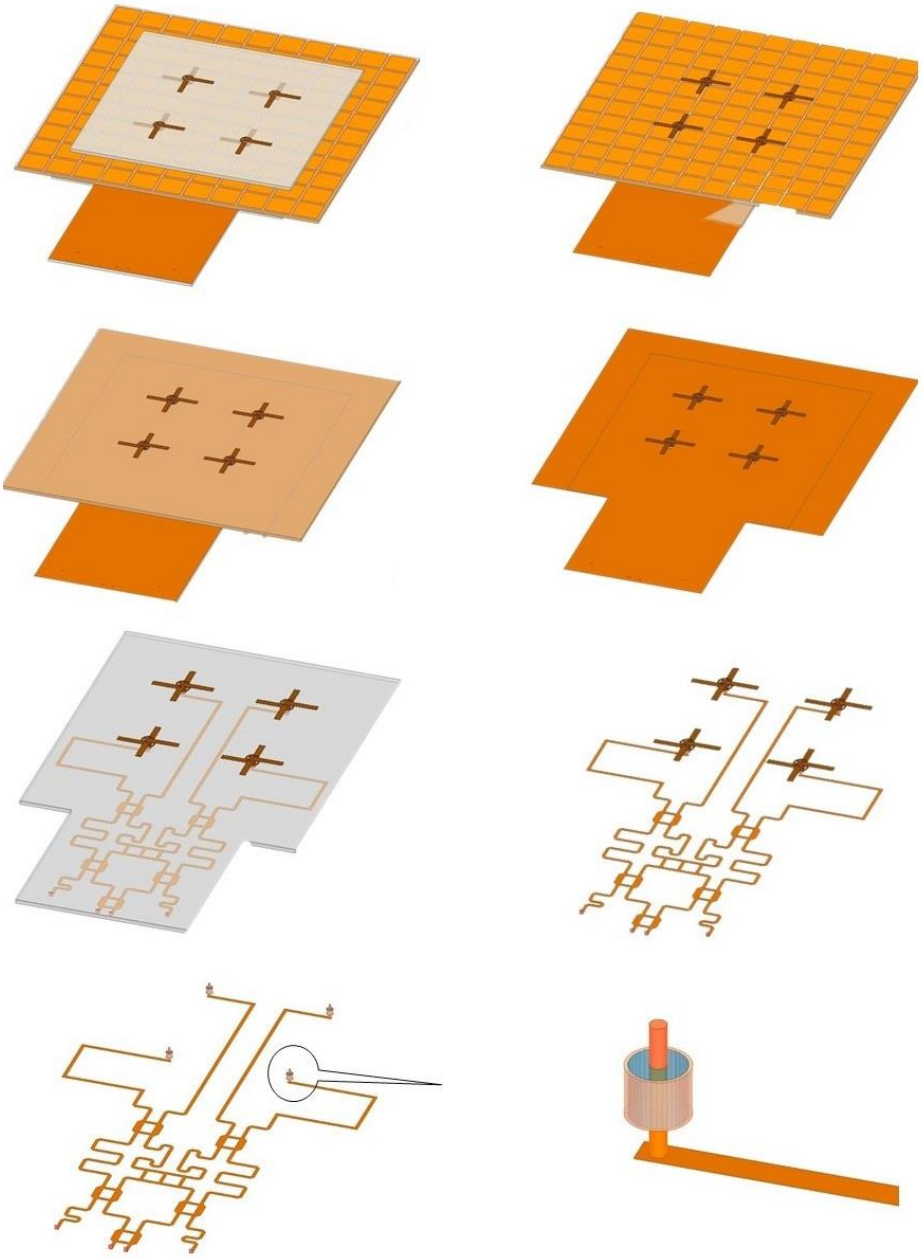

Figure 4-37 Topographic of the proposed new OAM antenna array IV using the Butler Matrix as a feeding network.

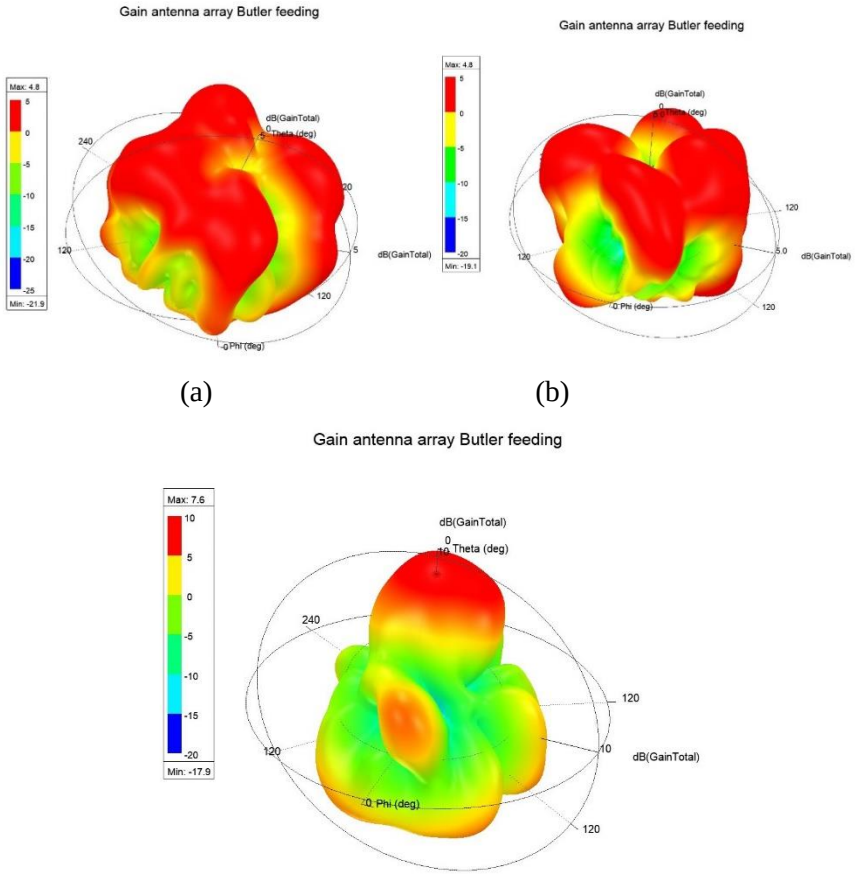

(a) (b)

(c)

Figure 4-38 3D radiation gain plots of the proposed OAM antenna array IV (a) port 1 (b) port 4 (c) linear gain (either port 2 or 3).

The red shadow in the amplitude distribution denotes regions of the high intensity, while the blue shadow represents the low intensity regions. **Figure 4-39** shows screenshots of the recorded near-field values for both amplitude and phase distributions. The OAM radio beams are formed by the typical vortex phase fronts, and the color change from green to red, blue, and back to green correspond to a phase change of 2π. When comparing the positive and negative modes, the phase distribution of l= +1 increases clockwise, whereas the phase distribution of l = -1 increases anticlockwise, see **Figure 4-40.**

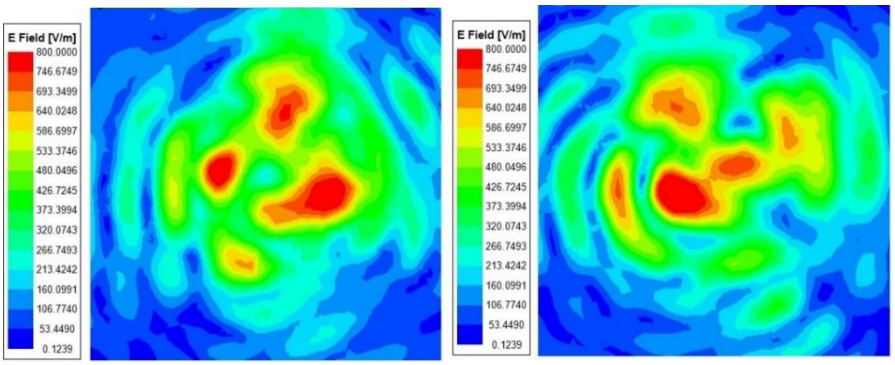

(a) (b)

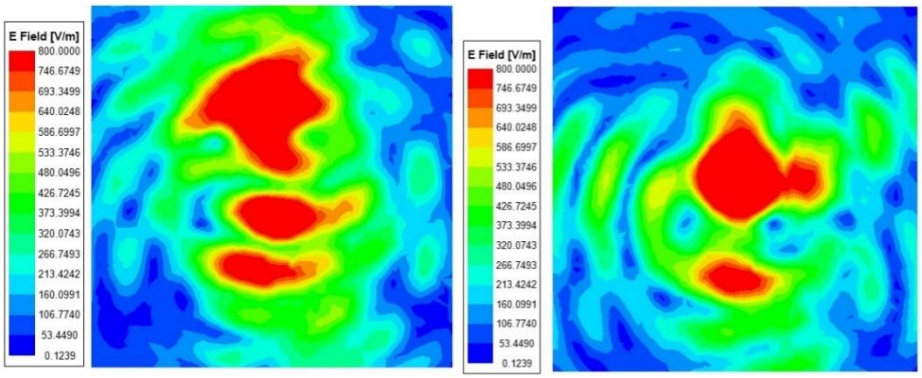

(c) (d)

Figure 4-39 Power intensity patterns (a) port 4 is excited *l*= -1 (b) port 1 is excited *l*= +1 (c) both ports 4 and1 are excited $l = \mp 1$ (d) port 2 or 3 is excited *l*= 0.

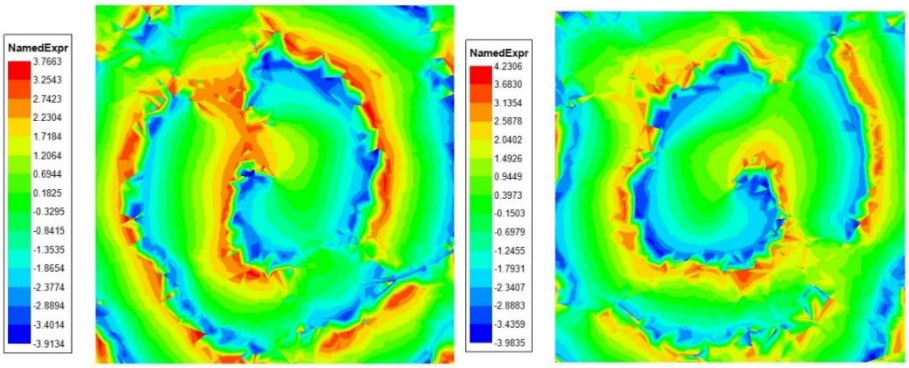

(a) (b)

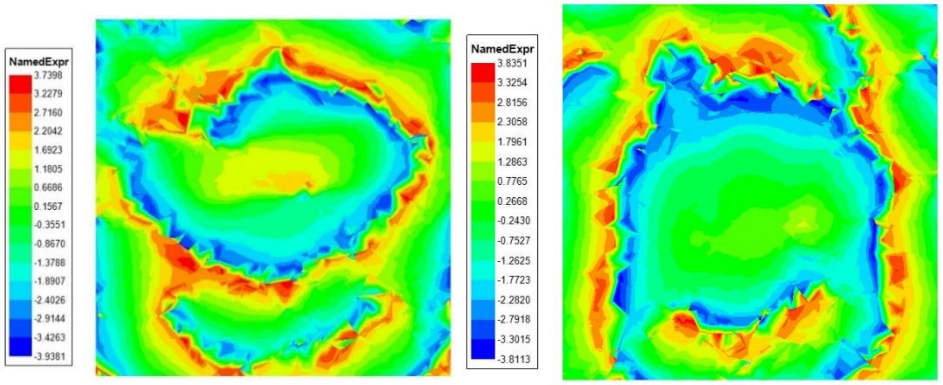

(c) (d)

Figure 4-40 Phase distribution patterns a) port 4 is excited *l*= -1 b) port 1 is excited *l*= +1 c) both ports 4 and1 are excited $l = \mp 1$ d) port 2 or 3 is excited *l*= 0.

The 2D far field radiation patterns of the xoz and yoz planes show the typical OAM pattern with a null in the center as seen **Figure 4-43**. Both planes have high co-polarization components compared to the cross-polarization ones. The cross-polarization components are unavoidable because of the waves generated from the orthogonal components. Many parts may contribute to produce the undesired components such as the coaxial probes, feeding network, etc.

The radiation patterns confirm that our design can generate the OAM EM waves as shown in **Figure 4-41**. Now, we can generate two different orthogonal OAM beams as well as the linear polarization beam. These three different modes can be used to transmit three signals simultaneously. To this end, we have designed a new OAM antenna array operating at the 28GHz (5G applications). The printed crossed-dipole antenna is for the first time used in a design of the OAM antenna array. This array can control its input ports to have a dynamic structure to change the transmission of signal from one polarization to another, avoiding channel jamming or eavesdropping.

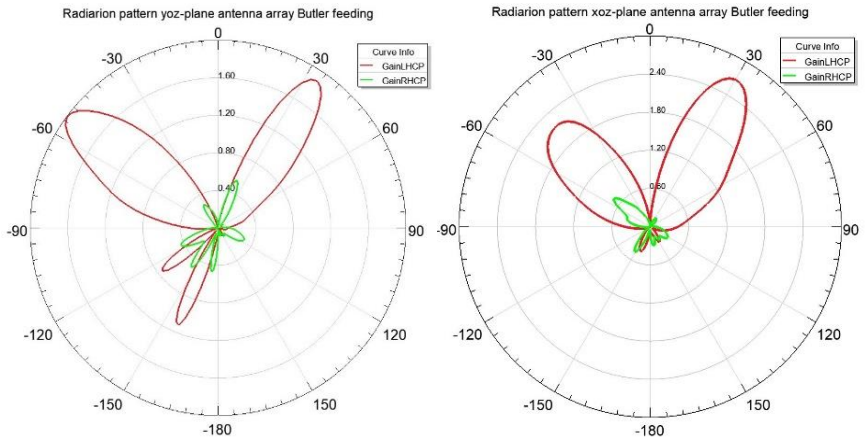
Radiarion pattern yoz-plane antenna array Butler feeding
Radiarion pattern xoz-plane antenna array Butler feeding
Curve Info
GainLHCP
GainRHCP

(a)

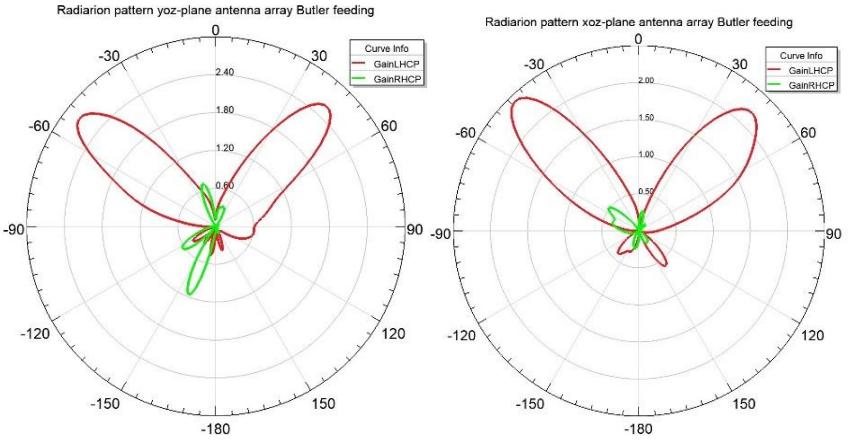
Radiarion pattern yoz-plane antenna array Butler feeding
Radiarion pattern xoz-plane antenna array Butler feeding
Curve Info
GainLHCP
GainRHCP

(b)

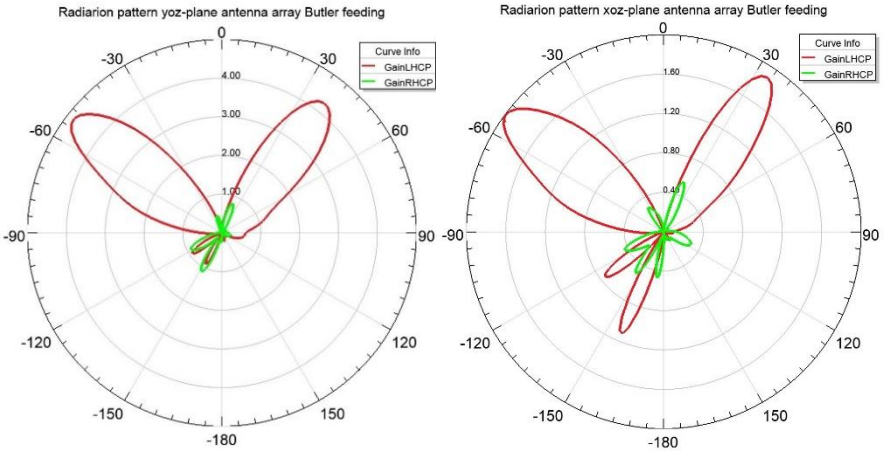
Radiarion pattern yoz-plane antenna array Butler feeding
Radiarion pattern xoz-plane antenna array Butler feeding
Curve Info
GainLHCP
GainRHCP

(c)

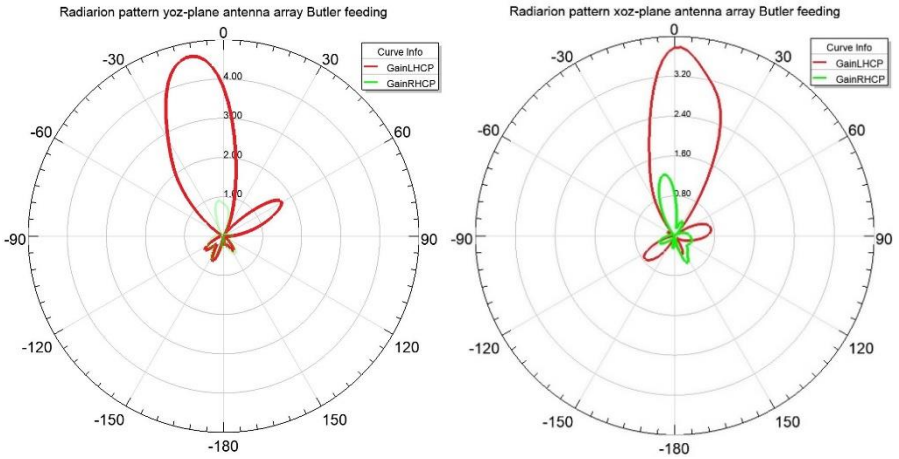

(d)

Figure 4-41 2D gain radiation patterns of the OAM antenna array IV for both the yoz and xoz-planes when exciting different input excitation ports.

Table 4-6 reports results and comparison of the previous works in Chapter one which are related to our proposed works.

Table 4-6 Results and comparison of the proposed work with other related works.

Ref.	type of antenna	feeding	multiplexing	No. of modes	profile	gain dB	frequency GH	
[5]	SSP	Horn antenna	☐	1	high	N/A	40	
[6]	metalens	N/A	☐	3	high	N/A	10	
[8]	DRA	Hybrid coupler	☒	2	high	5.4	5.8	
[9]	DRA Q-plat	Horn antenna	☐	1	high	N/A	100	
[16]	Patch UCA	Sequential phase	☐	1	low	4.6	10	
[12]	Patch UCA	Dual sequential phase	☒	2	low	N/A	4.8	
[13]	Patch UCA	M & U-shape Feeding	☒	2	low	9.5	5.6	
[14]	Patch UCA	PIN diode Feeding netwok	☒	2	low	N/A	2.4	
Ant. I	4-CDA Cavity reflector	N/A	☐	1	high	8.2	28	
Ant. II	4-CDA AMC reflector	N/A	☐	1	low	6.8	28	
Ant. III	8-CDA flat reflector	N/A	☒	3	High	9.2	28	
Ant. IV	4-CDA AMC reflector	Butler Matrix	☒	3	low	4.8	28	

Chapter 5: Conclusion and Future Work

In this chapter, the research will be concluded to give the interested readers a quick glance about what have been carried out in this research. Also, the future works will be presented.

5.1 Conclusion

Several research efforts have been conducted to investigate the design and numerically simulate the new OAM antenna arrays using the low profile printed crossed-dipole antennas. The OAM antenna arrays presented in our thesis were able to generate several OAM modes simultaneously to increase the channel capacity. The research work was divided into two parts.

In the first part, the single printed crossed-dipole antennas were designed and investigated. Starting was with the conventional printed one, and then moved into the one using the AMC as a ground to make it as a low profile structure. The conventional flat metal ground is easier to implement, but has low performance compared to other grounds such as the reflector with four walls and the AMC. The former one can focus the power in narrower beams, so the gain is higher compared to ones with the flat ground and the AMC, but the latter has higher gain than the antenna with the flat ground and lower gain compared the antenna with the four walls cavity reflector. Furthermore, the antenna with the AMC is low profile structure, so it is suitable to our presented OAM antenna arrays. Also, four PIN diodes were integrated on a path of the RF signals to make the printed crossed-dipole antenna reconfigurable to change between the RHCP and LHCP states. The printed crossed-dipole antenna with modified arms and scaled up were introduced. All these conducted works were to select the fit antenna to be used in the presented OAM antenna array. Eventually, the printed crossed-dipole antenna was manufactured and tested as a step to validate that our design can work properly.

The second part of the research work was how to build an effective OAM antenna array, being able to generate several modes simultaneously. Four,

eight, and nine elements were placed in the circular arrangement (i.e., circular array). All of them were placed on the MAC ground to guarantee that the arrays were low profile structures. Then, the OAM arrays were investigated to check up their performances. Their far field phase and amplitude distributions of the electric fields were demonstrated and the helical vortex beams were obvious. Two modes had been selected easily using the port one and port 4 in the Butler matrix, while the port 2 and 3 only support the linear phase distribution. As a result, more modes can be chosen as a number of antenna used in the OAM array is larger. However, this arrays were hard to simulate because of the computation resources as illustrated in this research work. Also, the complicated Butler matrix with a higher number of ports will lead to high losses, resulting in large imbalance in the phase required to generate the OAM-EM waves. We can say that looking for alternative feeding network will be preferred.

All the OAM antenna array parameters such as gain, AR, beam widths, radiation patterns, amplitude and phase distributions of the electric fields were numerically shown and checked and compared with other works.

5.2 Future work

The most important thing that we have concluded in this research is a number of the modes. Increasing the modes means that we should increase a number of elements and a feeding network with large number of inputs and outputs. However, looking for different schemes is one of future possibilities to design higher modes OAM antenna array an OAM antenna array with 9-modes using 9-input (i.e., real multiplexing) by the use of Rotman lens as a an feeding network

In addition, the future work using the 8*8 Butler matrix is another option. This feeding network should be designed to work at 28GHz with 16 different Phase shifters, 12 90-degree hybrid couplers and 4 crossovers. It can be integrated with eight elements of the CDAs as introduced in the subsection (4.3.44.3.4)**.** Here, there are two important advises. First, the Rotman lens should be matched into the focal ratio to produce as equal

amplitude as possible. Secondly, the successful phase sequence is necessary to obtain OAM EM waves.

Eventually, the simulated OAM arrays can be manufactured and tested in the future to have deep clue about how to send and receive several signals simultaneously.

References

[1] T. Translat by Itani, "QURAN ENGLISH TRANSLATION," ClearQuran Dallas, Beirut, 2016.

[2] Y. Zahra, "The Wild Theory of Nicolaus Copernicus," *'Adalah*, vol. 3, no. 3, pp. 120–126, 2019, doi: 10.15408/adalah.v3i3.16545.

[3] M. L. Allen, "Orbital angular momentum of light and the transformation ofLaguerre-Gaussian laser modes," *Phys. Rev. A*, vol. 45, no. 11, pp. 8185–8189, 1992.

[4] Y. Yan *et al.*, "High-capacity millimetre-wave communications with orbital angular momentum multiplexing," *Nat. Commun.*, vol. 5, pp. 1–9, 2014, doi: 10.1038/ncomms5876.

[5] W. Wei, K. Mahdjoubi, C. Brousseau, and O. Emile, "Horn antennas for generating radio waves bearing orbital angular momentum by using spiral phase plate," *IET Microwaves, Antennas Propag.*, vol. 10, no. 13, pp. 1420–1427, 2016, doi: 10.1049/iet-map.2016.0064.

[6] K. Zhang *et al.*, "Phase-engineered metalenses to generate converging and non-diffractive vortex beam carrying orbital angular momentum in microwave region," *Opt. Express*, vol. 26, no. 2, p. 1351, 2018, doi: 10.1364/oe.26.001351.

[7] Y. Wang *et al.*, "Planar Vortex Beam Generator for Circularly Polarized Incidence Based on FSS," *IEEE Trans. Antennas Propag.*, vol. 68, no. 3, pp. 1514–1522, 2020, doi: 10.1109/TAP.2019.2938666.

[8] J. Ren and K. W. Leung, "Generation of microwave orbital angular momentum states using hemispherical dielectric resonator antenna," *Appl. Phys. Lett.*, vol. 112, no. 13, pp. 1–6, 2018, doi: 10.1063/1.5021951.

[9] S. MacCalli, G. Pisano, S. Colafrancesco, B. Maffei, M. W. R. Ng, and M. Gray, "Q-plate for millimeter-wave orbital angular momentum manipulation," *Appl. Opt.*, vol. 52, no. 4, pp. 635–639, 2013, doi: 10.1364/AO.52.000635.

[10] S. M. Mohammadi *et al.*, "Orbital angular momentum in radio: Measurement methods," *Radio Sci.*, vol. 45, no. 4, pp. 565–572, 2010, doi: 10.1029/2009RS004299.

[11] Q. Bai, A. Tennant, and B. Allen, “Experimental circular phased array for generating OAM radio beams,” *Electron. Lett.*, vol. 50, no. 20, pp. 1414–1415, 2014, doi: 10.1049/el.2014.2860.

[12] X. D. Bai *et al.*, “Experimental Array for Generating Dual Circularly-Polarized Dual-Mode OAM Radio Beams,” *Sci. Rep.*, vol. 7, no. November 2016, pp. 1–8, 2017, doi: 10.1038/srep40099.

[13] H. Li, L. Kang, F. Wei, Y. M. Cai, and Y. Z. Yin, “A Low-Profile Dual-Polarized Microstrip Antenna Array for Dual-Mode OAM Applications,” *IEEE Antennas Wirel. Propag. Lett.*, vol. 16, pp. 3022–3025, 2017, doi: 10.1109/LAWP.2017.2758520.

[14] B. Liu, G. Lin, Y. Cui, and R. L. Li, “An Orbital Angular Momentum (OAM) Mode Reconfigurable Antenna for Channel Capacity Improvement and Digital Data Encoding,” *Sci. Rep.*, vol. 7, no. 1, pp. 1–9, 2017, doi: 10.1038/s41598-017-10364-4.

[15] L. Kang, H. Li, J. Zhou, and S. Zheng, “An OAM-Mode Reconfigurable Array Antenna with Polarization Agility,” *IEEE Access*, vol. 8, pp. 40445–40452, 2020, doi: 10.1109/ACCESS.2020.2975846.

[16] W. J. Byun *et al.*, “Multiplexed Cassegrain Reflector Antenna for Simultaneous Generation of Three Orbital Angular Momentum (OAM) Modes,” *Sci. Rep.*, vol. 6, no. June, pp. 1–8, 2016, doi: 10.1038/srep27339.

[17] X. D. Bai, X. L. Liang, J. P. Li, K. Wang, J. P. Geng, and R. H. Jin, “Rotman Lens-Based Circular Array for Generating Five-mode OAM Radio Beams,” *Sci. Rep.*, vol. 6, no. April, pp. 1–8, 2016, doi: 10.1038/srep27815.

[18] Z. Y. Zhang, B. Yu, D. Wu, Y. Mao, and C. Zhang, “Rotman Lens-Fed Antenna for Generating Multiple Orbital Angular Momentum Modes,” *2020 IEEE Wirel. Commun. Netw. Conf. Work. WCNCW 2020 - Proc.*, vol. 8, pp. 29891–29900, 2020, doi: 10.1109/WCNCW48565.2020.9124789.

[19] R. Chen, H. Zhou, M. Moretti, X. Wang, and J. Li, “Orbital Angular Momentum Waves: Generation, Detection, and Emerging Applications,” *IEEE Commun. Surv. Tutorials*, vol. 22, no. 2, pp. 840–868, 2020, doi: 10.1109/COMST.2019.2952453.

[20] J. H. Poynting, “The wave motion of a revolving shaft, and a suggestion as to the angular momentum in a beam of circularly polarised light,” *Opt. Angular Momentum*, vol. 82, pp. 560–567, 1909, doi: 10.1098/rspa.1909.0060.

[21] M. Padgett, J. Arit, N. Simpson, and L. Allen, “An experiment to observe the intensity and phase structure of laguerre-gaussian laser modes,” *Opt. Angular Momentum*, vol. 77, no. 1996, pp. 114–119, 1996, doi: 10.1119/1.18283.

[22] H. Zhou, J. Dong, J. Wang, X. Cai, S. Yu, and X. Zhang, “Dividing

orbital angular momentum of light," *ICOCN 2016 - 2016 15th Int. Conf. Opt. Commun. Networks*, 1999, doi: 10.1109/ICOCN.2016.7875871.

[23] A. M. Yao and M. J. Padgett, "Orbital angular momentum: origins, behavior and applications," *Adv. Opt. Photonics*, vol. 3, no. 2, p. 161, 2011, doi: 10.1364/aop.3.000161.

[24] E. Engineers, "IEEE Std 145-1983 IE E E Standard Definitions of Terms for Antennas," vol. 1983, 1983.

[25] David_M._Pozar, *Microwave_Engineering*, 3rd_Editio. 2005.

[26] A. Balanis, *ANTENNA THEORY ANALYSIS AND DESIGN!*, Fourth edi. Inc., Hoboken, New Jersey: John Wiley & Sons, 2016.

[27] R. Dewan *et al.*, "Artificial magnetic conductor for various antenna applications: An overview," *Int. J. RF Microw. Comput. Eng.*, vol. 27, no. 6, pp. 1–18, 2017, doi: 10.1002/mmce.21105.

[28] W. E. Doherty and W. E. Doherty, "The PIN Diode Designers' Handbook," no. 617, 1998, [Online]. Available: http://www.ieee.li/pdf/essay/pin_diode_handbook.pdf.

[29] T. A. Denidni and T. É. Libar, "Wide band four-port butler matrix for switched multibeam antenna arrays," *IEEE Int. Symp. Pers. Indoor Mob. Radio Commun. PIMRC*, vol. 3, pp. 2461–2464, 2003, doi: 10.1109/PIMRC.2003.1259161.

[30] P. H. Smith, "'Cloverleaf' antenna for F.M. broadcasting," *Proceedings of the IRE*, vol. 35, no. 12. pp. 1556–1563, 1947, doi: 10.1109/JRPROC.1947.230912.

[31] B. ~. F, "A New Type of Circular Polarizer Using Crossed Dipoles." *Re Transactions On Microwave Theory And Techniques*, pp. 385–388, 1961.

[32] S. X. Ta, I. Park, and R. W. Ziolkowski, "Circularly polarized crossed dipole on an HIS for 2.4/5.2/5.8-GHz WLAN applications," *IEEE Antennas and Wireless Propagation Letters*, vol. 12. pp. 1464–1467, 2013, doi: 10.1109/LAWP.2013.2288787.

[33] Y. F. Lin, Y. K. Wang, H. M. Chen, and Z. Z. Yang, "Circularly polarized crossed dipole antenna with phase delay lines for RFID handheld reader," *IEEE Transactions on Antennas and Propagation*, vol. 60, no. 3. pp. 1221–1227, 2012, doi: 10.1109/TAP.2011.2180319.

[34] Y. L. Guoping Pan, "Isotropic Radiation From a Compact Planar Antenna Using Two Crossed Dipoles." *ieee antennas and wireless propagation letters*, pp. 1338–1341, 2012.

[35] S. X. Ta, S. Member, H. Choo, I. Park, and R. W. Ziolkowski, "Crossed , Asymmetrically Barbed Dipole Antennas for GPS Applications," no. c. pp. 1–6, 2013.

[36] T.-H. L. and Y.-S. K. J.-W. Baik, K.-J. Lee, W.-S. Yoon, “Circularly polarised printed crossed dipole antennas with broadband axial ratio,” *Electron. Lett.*, vol. 41, no. 2, pp. 40–41, 2008, doi: 10.1049/el.

[37] J. W. Baik, T. H. Lee, S. Pyo, S. M. Han, J. Jeong, and Y. S. Kim, “Broadband circularly polarized crossed dipole with parasitic loop resonators and its arrays,” *IEEE Trans. Antennas Propag.*, vol. 59, no. 1, pp. 80–88, 2011, doi: 10.1109/TAP.2010.2090463.

[38] G. Feng, L. Chen, X. Xue, and X. Shi, “Broadband Circularly Polarized Crossed-Dipole Antenna with a Single Asymmetrical Cross-Loop,” *IEEE Antennas Wirel. Propag. Lett.*, vol. 16, no. 2, pp. 3184–3187, 2017, doi: 10.1109/LAWP.2017.2767700.

[39] L. Wang, W. X. Fang, Y. F. En, Y. Huang, W. H. Shao, and B. Yao, “Wideband Circularly Polarized Cross-Dipole Antenna with Parasitic Elements,” *IEEE Access*, vol. 7, no. c, pp. 35097–35102, 2019, doi: 10.1109/ACCESS.2019.2904658.

[40] L. Wang, W. X. Fang, W. H. Shao, B. Yao, Y. Huang, and Y. F. En, “Broadband circularly polarized cross-dipole antenna with multiple modes,” *IEEE Access*, vol. 8, pp. 66489–66494, 2020, doi: 10.1109/ACCESS.2020.2981050.

[41] T. K. Nguyen, H. H. Tran, and N. Nguyen-Trong, “A Wideband Dual-Cavity-Backed Circularly Polarized Crossed Dipole Antenna,” *IEEE Antennas Wirel. Propag. Lett.*, vol. 16, no. c, pp. 3135–3138, 2017, doi: 10.1109/LAWP.2017.2764923.

[42] S. X. Ta and I. Park, “Crossed dipole loaded with magneto-electric dipole for wideband and wide-beam circularly polarized radiation,” *IEEE Antennas Wirel. Propag. Lett.*, vol. 14, pp. 358–361, 2015, doi: 10.1109/LAWP.2014.2363944.

[43] Z. Zhao, Y. Li, L. Wang, Z. Tang, and Y. Yin, “Design of broadband circularly polarized antenna via loading coupled rotated dipoles,” *Microw. Opt. Technol. Lett.*, vol. 61, no. 2, pp. 425–430, 2019, doi: 10.1002/mop.31586.

[44] H. H. Tran, I. Park, and T. K. Nguyen, “Circularly Polarized Bandwidth-Enhanced Crossed Dipole Antenna with a Simple Single Parasitic Element,” *IEEE Antennas Wirel. Propag. Lett.*, vol. 16, no. c, pp. 1776–1779, 2017, doi: 10.1109/LAWP.2017.2676165.

[45] H. H. Tran and I. Park, “Wideband Circularly Polarized Cavity-Backed,” *IEEE Trans. Antennas Propag.*, vol. 15, pp. 358–361, 2016.

[46] D. Wu, Z. Y. Zhang, L. Ji, L. Yang, G. Fu, and X. Shi, “Wideband circularly polarized cross bowtie dipole antenna with axial-ratio bandwidth enhancement,” *Prog. Electromagn. Res. C*, vol. 72, no. February, pp. 65–72, 2017, doi: 10.2528/PIERC17011503.

[47] G. Feng, L. Chen, X. Wang, X. Xue, and X. Shi, “Broadband circularly polarized crossed bowtie dipole antenna loaded with parasitic elements,” *IEEE Antennas Wirel. Propag. Lett.*, vol. 17, no.

1, pp. 114–117, 2018, doi: 10.1109/LAWP.2017.2777442.

[48] W. J. Yang, Y. M. Pan, and S. Y. Zheng, “A Low-Profile Wideband Circularly Polarized Crossed-Dipole Antenna with Wide Axial-Ratio and Gain Beamwidths,” *IEEE Trans. Antennas Propag.*, vol. 66, no. 7, pp. 3346–3353, 2018, doi: 10.1109/TAP.2018.2829810.

[49] L. Zhang *et al.*, “Single-feed ultra-wideband circularly polarized antenna with enhanced front-to-back ratio,” *IEEE Trans. Antennas Propag.*, vol. 64, no. 1, pp. 355–360, 2016, doi: 10.1109/TAP.2015.2501844.

[50] S. X. Ta and I. Park, “Artificial magnetic conductor-based circularly polarized crossed-dipole antennas: 1. AMC structure with grounding pins,” *Radio Sci.*, vol. 52, no. 5, pp. 630–641, 2017, doi: 10.1002/2016RS006203.

[51] V. Prakash, S. Dahiya, S. Kumawat, and P. Singh, “Design of 4 × 4 butler matrix and its process modeling using petri nets for phase array systems,” *Prog. Electromagn. Res. C*, vol. 103, no. February, pp. 137–153, 2020, doi: 10.2528/pierc20022003.

[52] A. Array, Y. Park, J. Bang, and J. Choi, “applied sciences Dual-Circularly Polarized 60 GHz Beam-Steerable,” 2020.

[53] A. Shastrakar, “Design and Simulation of Microstrip Butler Matrix Elements Operat-ing at 2.4GHz for Wireless Applications,” *Int. J. Sci. Eng. Res.*, vol. 7, no. 5, pp. 1528–1531, 2016, [Online]. Available: http://www.ijser.org.

الخلاصة

يتطلب الزيادة في عدد المشتركين والأجهزة المتصلة معًا عبر الأنظمة اللاسلكية أو الإنترنت استخدام جميع الموارد المتاحة قدر الإمكان. تهدف هذه الرسالة إلى إلقاء الضوء على استخدام مضاعفة الإرسال المكاني كدرجة إضافية من الحرية لزيادة سعة قناة الاتصال. عادةً ما يكون تعدد إرسال الوقت والتردد من أكثر التقنيات شيوعًا المستخدمة في أنظمة الاتصالات.

الزخم الزاوي المداري OAM هو تقنية تم استغلالها في هذه الأطروحة. يمكن أن تحمل OAM عدة إشارات EM متعامدة في وقت واحد إذا تم تغذية النظام بواسطة دائرة قادرة على تغذية نظام OAM بمدخلات متعددة. تنقسم مهمة البحث بأكملها إلى ثلاثة أجزاء لتسهيل هذا الإنجاز. الجزء الأول مخصص لتصميم عناصر الهوائي الفردي Crossed-dipole هو الهوائي المطبوع ثنائي القطب. يبدأ التصميم بالتصميم التقليدي وينتهي بتصميم يتمتع بأداء عالٍ وهو تركيب منخفض المظهر مقارنة بالتصميم التقليدي. تم زيادت الكسب وكذلك تم تقليل مركبات الاستقطاب المتقاطع وايضاً مُتجه الإشعاع مستقرًا وتم تقليل الفجوة بين الباعث الرئيسي والعاكس. حيث أُستخدامَ التجويف ذو أربعة جدران cavity والموصل المغناطيسي الصناعي AMC للقيام بذلك. الطريقة الأولى تركز الطاقة على حزم أضيق ، وبالتالي يتم تحسين الكسب ، بينما تساعد الطريقة الأخيرة على تقليل الفجوة الفاصلة بين الباعث الرئيسي والعاكس. أيضًا تم تنفيذ أشياء أخرى مثل استخدام مجموعة من الدايودات لجعل التصميم عبارة عن هوائي قابل لإعادة تشكيل اتجاه الأستقطاب الدائري.

ثانيًا تم تطوير شبكة تغذية تعمل ضمن الترددات اللاسلكية باستخدام مصفوفة بتلر. حيث يمكن لكل منفذ إدخال توزيع الإشارة على جميع منافذ الإخراج مع أزاحة طور تدريجي ولكل منفذ أزاحة طور تقدمي خاص به ومتعامد مع بعضها البعض. تتيح هذه الخاصية لتصميمنا المقترح أن ارسال عدة إشارات متعامدة بشكل متزامن.

في النهاية تم تصميم العديد من النسخ المتماثلة للهوائي Crossed-dipole ضمن ترتيب دائري موحد UCA للتوصل إلى تصميم مصفوفة هوائي الـOAM حيث تُستخدم أربعة وثمانية وتسعة من عناصر الهوائي في المصفوفة الـOAM كخطوة لزيادة عدد الأشارات المرسلة. من خلال تغذية عناصر الهوائي OAM مباشرة أو من خلال شبكات تغذية ذو التردد الراديوي. كذلك الحصول على موجة كهرومغناطسية أعصارية متضمنة عدة اشارات متعامدة مع بعضها بأطوار مختلفة والتي تم عرضها في العمل.

ظاهرة الزخم الزاوي المداري قائمة على تصميم مصفوفة هوائيات تعمل ضمن موجات الدقيقة

الرسالة

مقدمة الى قسم هندسة تقنيات الاتصالات كجزء من متطلبات نيل درجة

الماجستير

تقدم بها

مصطفى عبد المهدي محمد حسن المظفر

إشراف

المدرس الدكتور حسام نعمان محمد علي الأنصاري

2021

جمهورية العراق
وزارة التعليم العالي والبحث العلمي
جامعة الفرات الاوسط التقنية
الكلية التقنية الهندسية- نجف

ظاهرة الزخم الزاوي المداري قائمة على تصميم مصفوفة هوائيات تعمل ضمن موجات الدقيقة

مصطفى عبد المهدي محمد حسن المظفر

ماجستير هندسة تقنيات الاتصالات

2021